

## LIBRARY Michigan State University

This is to certify that the

thesis entitled

ELECTRON SPIN ECHO ENVELOPE MODULATION STUDIES ON METHYLMALONYL-COA MUTASE

presented by

Nadia Anjum Shams-Ahmed

has been accepted towards fulfillment of the requirements for

M. S. degree in Chemistry

Date 9/29/99

**O**-7639

MSU is an Affirmative Action/Equal Opportunity Institution

PLACE IN RETURN BOX to remove this checkout from your record.

TO AVOID FINES return on or before date due.

MAY BE RECALLED with earlier due date if requested.

DATE DUE	DATE DUE	DATE DUE
	N 10-20	
		<del></del>
	. 10 1	

6/01 c:/CIRC/DateDue.p65-p.15

# ELECTRON SPIN ECHO ENVELOPE MODULATION STUDIES ON METHYLMALONYL-COA MUTASE

Ву

Nadia Anjum Shams-Ahmed

## AN ABSTRACT OF A THESIS

Submitted to
Michigan State University
in partial fulfillment of the requirements
for the degree of

**MASTER OF SCIENCE** 

**Department Of Chemistry** 

1999

#### ABSTRACT

## ELECTRON SPIN ECHO ENVELOPE MODULATION STUDIES ON METHYLMALONYL-COA MUTASE

### By

## Nadia Anjum Shams-Ahmed

Vitamin B<sub>12</sub>, a cobalt-based cofactor, is involved in many enzymatic systems, including methylmalonyl-CoA mutase. Methylmalonyl-CoA mutase is an enzyme that converts *L*-methylmalonyl-CoA into succinyl-CoA, which is part of respiratory metabolism. The mechanism involved in this reaction is not yet known. The most popularly accepted mechanism involves a free radical pathway.

Ruma Banerjee and Rugmini Padmakumar have tried to identify the radical intermediates of this enzymatic reaction by using electron paramagnetic resonance (EPR) spectroscopy. They found inhomogeneous broadening in their spectra, and hyperfine splittings resulting from coupling of the unpaired electron with the cobalt nucleus. They also did a power dependence study on the enzyme in the presence of the substrate at two different temperatures. At 10K they saw two different signals, whereas at 25K they only saw one. The spectra showed coupling to the cobalt, which indicated that cobalamin, a cobalt-based radical formed from the B<sub>12</sub> cofactor, was one of the radicals. It was not clear, however, what the other radical species was.

Electron spin echo envelope modulation, a pulsed EPR technique, was performed on their samples in order to continue their study. ESEEM data showed peaks in the low frequency region of the spectrum that are characteristic of coupled nitrogen. Isotopic substitution of protein bound <sup>14</sup>N coupled with further ESEEM studies allowed us to assign these modulations to a histidyl group, coordinated axially to Co(II).

To Allah, the one God, who blessed me with the ability and energy to comprise this work, and who helped me in various ways to make this possible.

To Hadhrat Mirza Tahir Ahmad, Khalifatul Masih IV, whose guidance and prayers provided me with peace of mind.

To my late father, Dr. Salah U. Shams, who taught me about spirituality, dedication, and hard work through example.

To my husband Tahir, who helped me keep my sanity and never stopped believing in me.

Last but not least, to my mother Kaukab, my sister Sabiha, and my brother Sabah, who constantly encouraged me and never let me give up.

## **ACKNOWLEDGMENTS**

I would like to thank the following individuals for giving me their time, patience, and support during the course of this project:

Dr. John McCracken

Dr. Gerald Babcock

Dr. Marilena DiValentin

Pierre Dorlet

Dr. Curt Hoganson

Dr. Steve Siebold

Dr. Hans Schelvis

Gwynne Osaki

Tara Simmons

and

Nasir Bukhari.

## TABLE OF CONTENTS

LIST OF TABLESvi
LIST OF FIGURESvii
LIST OF ABBREVIATIONSviii
CHAPTER I
INTRODUCTION 1 References 13
CHAPTER II
ELECTRON PARAMAGNETIC RESONANCE METHODS14
Origin Of the Zeeman Effect14
Derivation Of the Spherical Harmonics
Derivation Of the Angular Momentum Operators20
Deriving the Zeeman Energy From A Hydrogen-Like Atom (S = ½)24
Deriving the Two Spin Energy States For An Electron
The Nuclear Zeeman Interaction
Electron Nuclear Hyperfine Interaction: Isotropic and Anisotropic32
Orientation Of the Lab Axes With Respect To the Hyperfine Axes40
Data Of Enzyme With Substrate and Product44
Principles Of Transition Rates and Power Saturation49
Power and Temperature Dependence Study59
References 63
CHAPTER III
ELECTRON SPIN ECHO ENVELOPE MODULATION64
Two Pulse ESEEM65
Two Pulse ESEEM For $S = \frac{1}{2}$ and $I = \frac{1}{2}$ Spin System69
Two Pulse ESEEM For A System With $S = \frac{1}{2}$ and $I = 1$ 73
Modulations Of Two-Pulse ESEEM75
Three-Pulse ESEEM
Modulations Of Three-Pulse ESEEM
The τ-Suppression Effect79
Fourier Transformation80
References 83
CHAPTER IV
NUCLEAR QUADRUPOLAR INTERACTION OF <sup>14</sup> N84
Deriving the Nuclear Quadrupolar Interaction Energies For An I = 1  Nucleus
Resonant Frequencies Of the Nuclear Quadrupolar Interaction90

Solving For the Field Gradient q and the Asymmetry Parameter $\eta$	91
Deriving the Energy Level Diagram For An $S = \frac{1}{2}$ and $I = 1$ System	92
References	96
CHAPTER V	
ESEEM OF METHYLMALONYL-COA MUTASE WITH L-METHYL-	
MALONYL-COA WITH <sup>14</sup> N	97
ESEEM Data Collection	
Samples Of Methylmalonyl-CoA Mutase	97
ESEEM Of <sup>14</sup> N Samples	
Discussion	
References	
CHAPTER VI	
ESEEM OF METHYLMALONYL-COA MUTASE WITH L-METHYL-	
MALONYL-COA WITH 15N	107
ESEEM Data Collection	
Samples Of Methylmalonyl-CoA Mutase	
ESEEM Of <sup>15</sup> N Sample	
Discussion	
Conclusion	
	117

## LIST OF TABLES

Table 4.1: The solutions of Equations (156), (157), and (158) for the three nuclear spin states  $m_I = -1$ , 0, and +1.

#### LIST OF FIGURES

- Figure 1.1: The chemical equation for the production of Acyl-CoA.
- Figure 1.2: The migration of acyl-CoA into the mitochondrion.
  - (a) At the outer mitochondrial membrane, acyl-CoA react with carnitine to form acyl-carnitine derivatives, which can cross the inner mitochondrial membrane.
  - (b) At the inner mitochondrial membrane, the acyl-carnitine derivatives are converted back to acyl-CoA and carnitine.
- Figure 1.3: The production of acyl-carnitine derivatives.
- Figure 1.4: Acetyl-CoA, which is a two carbon subunit produced during fatty acid metabolism or β-oxidation.
- Figure 1.5: Propionyl-CoA, which is produced during β-oxidation of odd-chain-length saturated fatty acids.
- Figure 1.6: The production of succinyl-CoA from propionyl-CoA.
- Figure 1.7: The structure of 5'-deoxyadenosylcobalamin coenzyme B<sub>12</sub> (vitamin B<sub>12</sub>).
- Figure 1.8: Adenosylcobalamin when recombined with methylmalonyl-CoA mutase.
- Figure 1.9: The postulated reaction mechanism of mmCoA mutase. The two possible radicals are either the deoxyadenosyl radical or a secondarily generated protein radical.
- Figure 1.10: Banerjee's and Padmakumar's EPR spectrum of the holoenzyme with deuterated substrate, [CD<sub>3</sub>]methylmalonyl-CoA. The eight small peaks are due to the hyperfine interaction between the unpaired electron and the cobalt(II) nucleus.
- Figure 2.1: The rotation of a mass m about a fixed point. The mass is rotating at a distance r from the center with a velocity v, and has an angular momentum L perpendicular to the plane of rotation.
- Figure 2.2: The rotation of a two particle system,  $m_1$  and  $m_2$ , about its center of mass. The particle  $m_1$  rotates at a distance  $r_1$  from the center of mass, while the particle  $m_2$  rotates at a distance  $r_2$  from the center of mass. The two particle system has an angular momentum L perpendicular to the plane of rotation.

- Figure 2.3: The relationship between the cartesian coordinates x, y, and z and the spherical polar coordinates r,  $\theta$ , and  $\phi$ .
- Figure 2.4: For an  $S = \frac{1}{2}$  system, the two degenerate electronic energy levels split further and further apart as the applied magnetic field is increased.
- Figure 2.5: The energy levels of a proton with  $I = \frac{1}{2}$  in a magnetic field.
- Figure 2.6: The vector for the electron magnetic dipole moment  $\mu_e$  will feel a local field from the vector for the nuclear magnetic dipole moment  $\mu_n$ . **B** is the applied magnetic field and  $\theta$  is the angle between the applied field and the axis of the two magnetic moments. The distance between the two dipoles is r. (The vector  $\mu_e$  represents the state  $m_s = -\frac{1}{2}$ , and the vector  $\mu_n$  represents the state  $m_I = +\frac{1}{2}$ .)
- Figure 2.7: The derivative spectrum of a nucleus with  $I = \frac{1}{2}$  interacting with an electron in an isotropic system. The constant a is the hyperfine splitting constant, and the resonant field value  $B_{resonance} = hv/(g\beta) \pm a/2$ .
- Figure 2.8: The derivative spectrum of a nucleus  $I = \frac{1}{2}$  interacting with an electron in an anisotropic system. It can be seen that  $A_{\perp}$  is not equal to  $A_{\parallel}$ .
- Figure 2.9: The axis system in terms of the hyperfine. **B** is the applied magnetic field and  $S_z$  is the electron spin in the direction of the applied field.
- Figure 2.10: The axis system in terms of the laboratory field **B**. The electron is at the origin interacting with the nearby nucleus.
- Figure 2.11: The EPR spectrum of mmCoA mutase with the substrate L-mmCoA.
- Figure 2.12: The EPR spectrum of mmCoA mutase with [CD<sub>3</sub>]mmCoA.
- Figure 2.13: The EPR spectrum of mmCoA mutase with the product succinyl-CoA.
- Figure 2.14: For a two level system, with ground state  $\beta$  and excited state  $\alpha$ , the microwave-induced upward transition rate  $mw_u$  equals the microwave-induced downward transition rate  $mw_d$  at low power.
  - (a) When the relaxation rate down is added to the microwave-induced rate down, they become greater than the upward transition rate.
  - (b) The microwave power can be increased to overcome the relaxation rate down, leading to a condition called power saturation.
- Figure 2.15: The two level system of an electron with  $S = \frac{1}{2}$ . The transition energy  $\Delta E = \gamma \hbar B$ . The number of spins in the two states are represented by  $N_+$  and  $N_-$ .

- Figure 2.16: The two level systems of both the electron system, labelled 1 and 2, and the reservoir, labelled b and a. The diagram in (a) represents an allowed transition, while the diagram in (b) represents a forbidden transition. The x's represent initial states. The populations of the two levels in the electron system are given by N<sub>1</sub> and N<sub>2</sub>, and the populations of the two levels in the reservoir system are given by N<sub>a</sub> and N<sub>b</sub>.
- Figure 2.17: The EPR spectrum of the power dependence study of mmCoA mutase with L-mmCoA at 10K. There is a shift in g values as the power is varied from 100mW to 0.05 mW. At 100 mW, the g value is 2.14. At 0.05 mW, the g value is 2.11.
- Figure 2.18: The EPR spectrum of the power dependence study of mmCoA mutase with L-mmCoA at 25K. As the power is varied from 100 mW to 0.05 mW, there is no shift in the g value. The g value of the lineshape is 2.11.
- Figure 3.1: Microwave pulse sequence of a two-pulse ESEEM experiment.
- Figure 3.2: The modulated echo decay plot of Ni(III)(CN)<sub>4</sub>(H<sub>2</sub>O)<sub>2</sub>.
- Figure 3.3: Classical picture of a two-pulse ESEEM experiment.  $B_0$  is the lab field,  $B_1$  is the magnetic field associated with the microwave pulses, M is the bulk magnetization, and  $\omega_0$  is the microwave pulse frequency.
- Figure 3.4: Energy level diagram describing the quantum mechanical results of an ESEEM experiment for an  $S = \frac{1}{2}$ ,  $I = \frac{1}{2}$  spin system. The frequencies  $\omega_{\alpha}$  and  $\omega_{\beta}$  are  $\omega_{\alpha} = [(\omega_{I} A/2)^{2} + B^{2}/4]^{1/2}$  and  $\omega_{\beta} = [(\omega_{I} + A/2)^{2} + B^{2}/4]^{1/2}$ .
- Figure 3.5: The combination of quantum mechanical results with classical results of an ESEEM experiment.
- Figure 3.6: The energy level diagram for an  $S = \frac{1}{2}$ , I = 1 spin system, showing the three allowed and six semiforbidden transitions.
- Figure 3.7: The microwave pulse sequence of a three-pulse ESEEM experiment.
- Figure 3.8: The classical picture of a three-pulse ESEEM experiment describing the formation of a stimulated echo.
- Figure 3.9: (a) The free induction decay (FID) spectrum for an  $S = \frac{1}{2}$ ,  $I = \frac{1}{2}$  spin system. (b) The frequency domain spectrum of the FID spectrum shown in (a).
- Figure 4.1: Different types of nuclei, varying in charge distributions.

- Figure 4.2: The energy splitting diagram of  $^{14}N$ , showing splittings from the (a) electron Zeeman energy  $[-g_e\beta_eH_0m_s]$ , (b) nuclear Zeeman interaction  $[-g_n\beta_nH_0/h = -v_n]$ , (c) the electron-nuclear hyperfine interaction  $[am_sm_I]$ , and (d) nuclear quadrupole interaction.  $v_n$  is the Larmor frequency, which is .94 MHz at 3060 G.
- Figure 4.3: The Fourier transformation spectrum of <sup>14</sup>N.
- Figure 5.1: The field scan of mmCoA mutase with L-mmCoA.
- Figure 5.2: The electron spin echo decay envelope of mmCoA mutase with L-mmCoA at 3060 G.
- Figure 5.3: The Fourier transformation of the spectrum shown in Figure 5.2, at 3060 G.
- Figure 5.4: The Fourier transformtion of the spectrum shown in Figure 5.2, at 3140 G.
- Figure 5.5: An illustration of cobalamin showing the three possible nitrogens coupled to the unpaired electron. The four nitrogens around the cobalt center are the pyrrole nitrogens. The nitrogen at the lower axial position is the nitrogen from the dimethylbenzimidazole. The dashed line leads to a nitrogen-based ligand from the protein of the enzyme.
- Figure 6.1: The two-pulse echo-detected EPR experiment of  $^{15}$ N-labelled mmCoA mutase with L-[CD<sub>3</sub>]mmCoA.
- Figure 6.2: The Fourier transformation spectrum of the three-pulse ESEEM spectrum of  $^{15}$ N-labelled mmCoA mutase with L-[CD<sub>3</sub>]mmCoA at 3060 G.
- Figure 6.3: The Fourier transformation spectrum of the three-pulse ESEEM spectrum of  $^{15}$ N-labelled mmCoA mutase with L-[CD<sub>3</sub>]mmCoA at 3220 G.
- Figure 6.4: The Fourier transformation spectrum of the three-pulse ESEEM spectrum of  $^{15}$ N-labelled mmCoA mutase with L-[CD<sub>3</sub>]mmCoA at 4000 G.
- Figure 6.5: An illustration showing cobalamin with the cobalt center coordinated at the lower axial position to a nitrogen-based ligand from the protein of the enzyme.

## LIST OF ABBREVIATIONS

CoA: Coenzyme A

TCA: Tricarboxylic Acid

ATP: Adenosine Triphosphate

MmCoA: Methylmalonyl-CoA

EPR: Electron Paramagnetic Resonance

ESEEM: Electron Spin Echo Envelope Modulation

L-mmCoA: L-methylmalonyl-CoA

K: Degrees Kelvin

mW: MilliWatts

FID: Fourier Induction Decay

<sup>14</sup>N: Nitrogen-14

<sup>15</sup>N: Nitrogen-15

MHz: MegaHerz

Cm: Centimeters

J: Joules

G: Gauss

Ns: Nanoseconds

<sup>2</sup>H: Deuterium

## **INTRODUCTION**

Methylmalonyl-CoA mutase is an enzyme that converts L-methylmalonyl-CoA into succinyl-CoA, which is part of the tricarboxylic acid (TCA) cycle. The TCA cycle is the component of respiratory metabolism that provides a means for breaking down two carbon units into carbon dioxide in the presence of oxygen. Succinyl-CoA is also utilized in the synthesis of heme in animals.  $^1$ 

Succinyl-CoA is produced during fatty acid metabolism. Fatty acids with an odd number of carbons are rare in many mammalian tissues, but in animals such as cows and sheep, the oxidation of these fatty acids can account for as much as 25% of their energy requirements.<sup>1</sup>

Inside cells, fatty acids are first reacted with coenzyme A and ATP in the cytosol to yield fatty acyl-CoA, illustrated in Figure 1.1<sup>1</sup>. This reaction is catalyzed by acyl-CoA ligase, also known as thiokinase. At the outer mitochondrial membrane, represented in Figure 1.2<sup>1</sup>, acyl-CoA reacts with carnitine to yield acyl-carnitine derivatives in a reaction described in Figure 1.3<sup>1</sup>, which can then cross the inner membrane of the mitochondrion. Once inside the mitochondrion, the acyl-carnitine derivatives are converted back to acyl-CoA and carnitine, shown in Figure 1.2<sup>1</sup>.

Inside the mitochondrion, odd-chain-length saturated fatty acids break down by a process called β-oxidation, to yield a number of acetyl-CoA's, shown in Figure 1.4<sup>1</sup>, and one propionyl-CoA, shown in Figure 1.5<sup>1</sup>. It is propionyl-CoA that begins the series of enzymatic reactions that produces succinyl-CoA, illustrated in Figure 1.6<sup>1</sup>. Propionyl-CoA, with the addition of ATP, CO<sub>2</sub>, and H<sub>2</sub>O, is converted into *D*-methylmalonyl-CoA with the enzyme propionyl-CoA carboxylase. Then *D*-methylmalonyl-CoA is converted

Figure 1.1: The chemical equation for the production of Acyl-CoA.

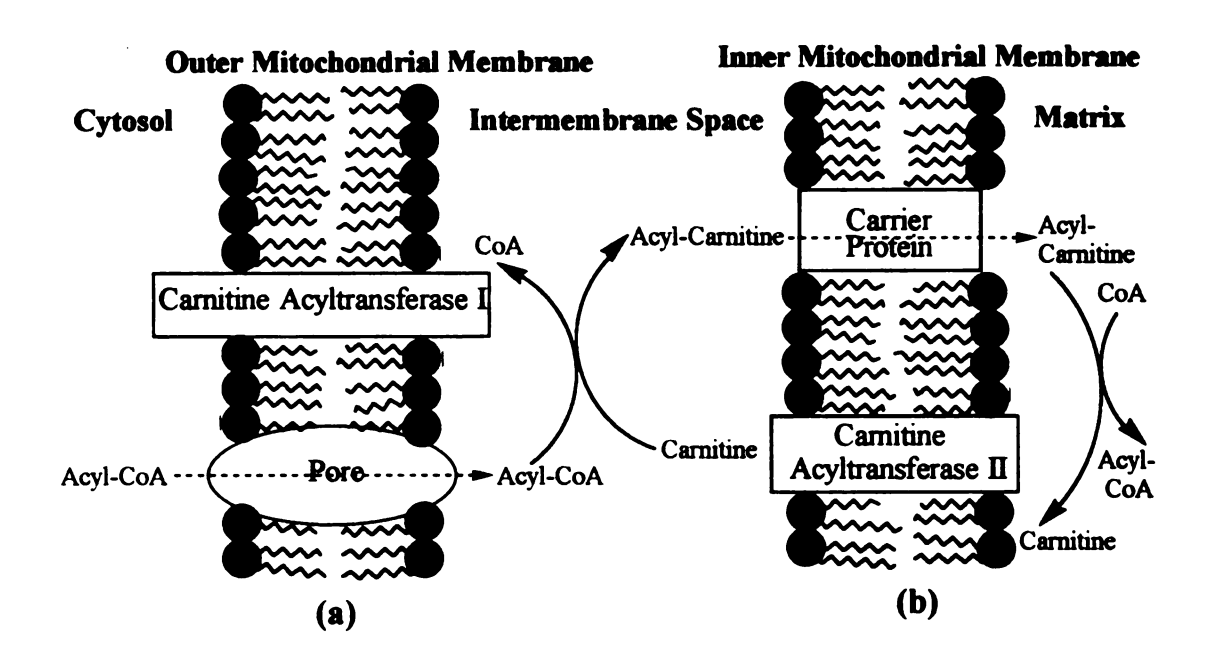


Figure 1.2: The migration of acyl-CoA into the mitochondrion.

- (a) At the outer mitochondrial membrane, acyl-CoA react with carnitine to form acyl-carnitine derivatives, which can cross the inner mitochondrial membrane.
- (b) At the inner mitochondrial membrane, the acyl-carnitine derivatives are converted back to acyl-CoA and carnitine.

Figure 1.3: The production of acyl-carnitine derivatives.

Figure 1.4: Acetyl-CoA, which is a two carbon subunit produced during fatty acid metabolism, or  $\beta$ -oxidation.

Figure 1.5: Propionyl-CoA, which is produced during β-oxidation of odd-chain-length saturated fatty acids.

Figure 1.6: The production of succinyl-CoA from propionyl-CoA.

into its optical isomer by methylmalonyl-CoA racemase. Finally, methylmalonyl-CoA mutase converts L-methylmalonyl-CoA into succinyl-CoA.<sup>1</sup>

The conversion of L-methylmalonyl-CoA into succinyl-CoA is an intramolecular rearrangement reaction on adjacent carbon atoms (refer to Figure 1.6<sup>1</sup>). The thioester group on the  $\alpha$ -carbon migrates to the  $\beta$ -carbon in exchange for a hydrogen atom. This isomerization is catalyzed by methylmalonyl-CoA mutase. The dysfunction of this enzyme leads to a condition called methylmalonic acidemia, which is an inborn error of amino acid metabolism. The symptoms and effects of this disease are vomiting, convulsions, mental retardation, and eventually death.  $\alpha$ 

MmCoA mutase is a vitamin B<sub>12</sub>-dependent enzyme. There are a variety of enzymes that are dependent on the B<sub>12</sub> cofactor, such as diol dehydratase, glutamate mutase, *L*-β-Lysine aminomutase, ethanolamine ammonia lyase, ribonucleotide reductase, and methionine synthase.<sup>2</sup> The vitamin B<sub>12</sub> coenzymes consist of a cobalt atom bonded to four pyrrole nitrogens forming a "corrin" ring, as can be seen in Figure 1.7<sup>1</sup>. The upper axial position on the cobalt can be a methyl, a hydroxide, or a 5'-deoxyadenosyl group, which is the principle coenzymatic form. In the case of methylmalonyl-CoA mutase, the B<sub>12</sub> cofactor is adenosylcobalamin, where the upper axial position is a 5'-deoxyadenosine. The lower axial position is occupied by a dimethylbenzimidazole group.<sup>1</sup> However, studies have been done on the methionine synthase system showing that when the B<sub>12</sub> cofactor is bound to the enzyme, the lower axial position is no longer coordinated to the dimethylbenzimidazole group, but rather to the side chain of a histidine residue.<sup>3</sup> This mode of bonding was also found for methylmalonyl-CoA mutase, as shown in Figure 1.8.<sup>4</sup>

Figure 1.7: The structure of 5'-deoxyadenosylcobalamin coenzyme  $B_{12}$  (vitamin  $B_{12}$ ).

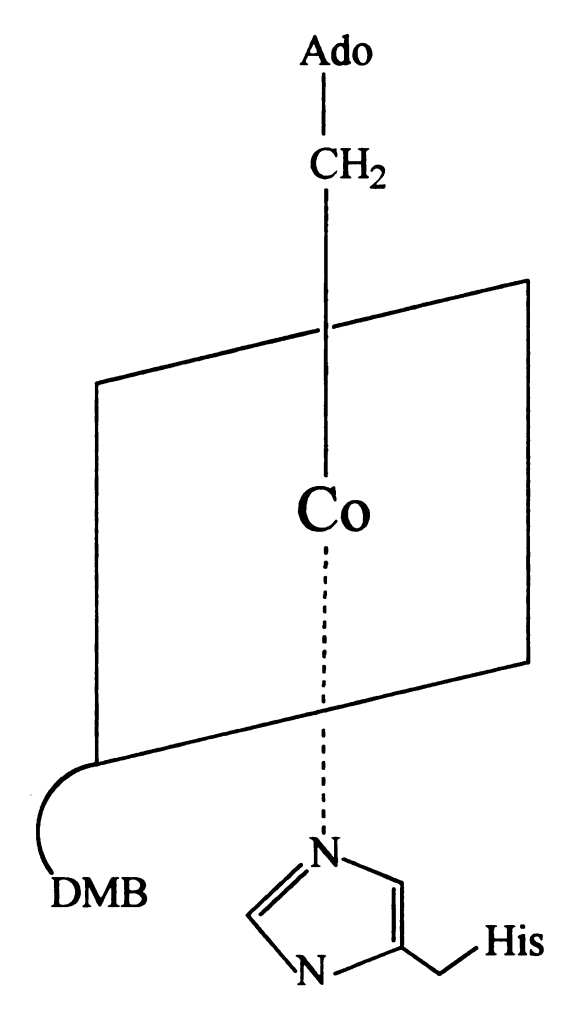


Figure 1.8: Adenosylcobalamin when recombined with methylmalonyl-CoA mutase.

The B<sub>12</sub>-dependent enzymes are all involved in rearrangement reactions, but there has been a lot of ambiguity about the mechanism of the rearrangements. The most popularly accepted reaction mechanism involves a free radical pathway, which begins at the metal center of the cofactor.<sup>2</sup> This is not a phenomenon that is unique to the B<sub>12</sub>-dependent enzymes. In fact, the B<sub>12</sub>-dependent enzymes are one of the three families of the larger metallo-radical class of enzymes, which share similar structural and functional principles. The three families are the glycyl/thiyl radical enzymes, the B<sub>12</sub>-dependent enzymes, and the O<sub>2</sub>-dependent radical enzymes. Basically, the metal centers of these enzymes consist of either copper, cobalt, iron, or manganese and act to generate an amino acid radical. This radical then initiates catalysis by abstracting a hydrogen atom from the substrate.<sup>5</sup> However, it is the actual details of how this mechanism occurs in each system that is of current interest.

It is believed that the mechanism involved in the production of succinyl-CoA from methylmalonyl-CoA mutase is comprised of three main steps, illustrated in Figure 1.9<sup>6</sup>. The first step is the homolytic bond cleavage of the cobalt-carbon bond of the B<sub>12</sub> cofactor to produce a cobalamin free radical and an adenosyl free radical.<sup>6</sup> Upon binding to the substrate, the corrin ring undergoes conformational changes that lengthens and weakens the cobalt-carbon bond, allowing for ease of dissociation of the bond. However, it has not been determined whether the steric interactions alone provide enough energy to break the bond.<sup>2</sup> The second step is hydrogen abstraction from the substrate. After the cobalt-carbon bond dissociates, the adenosyl radical, either directly or via a protein radical, abstracts a hydrogen atom from the methyl group of *L*-methylmalonyl-CoA, generating a reactive primary radical on the substrate. The third step is the 1,2

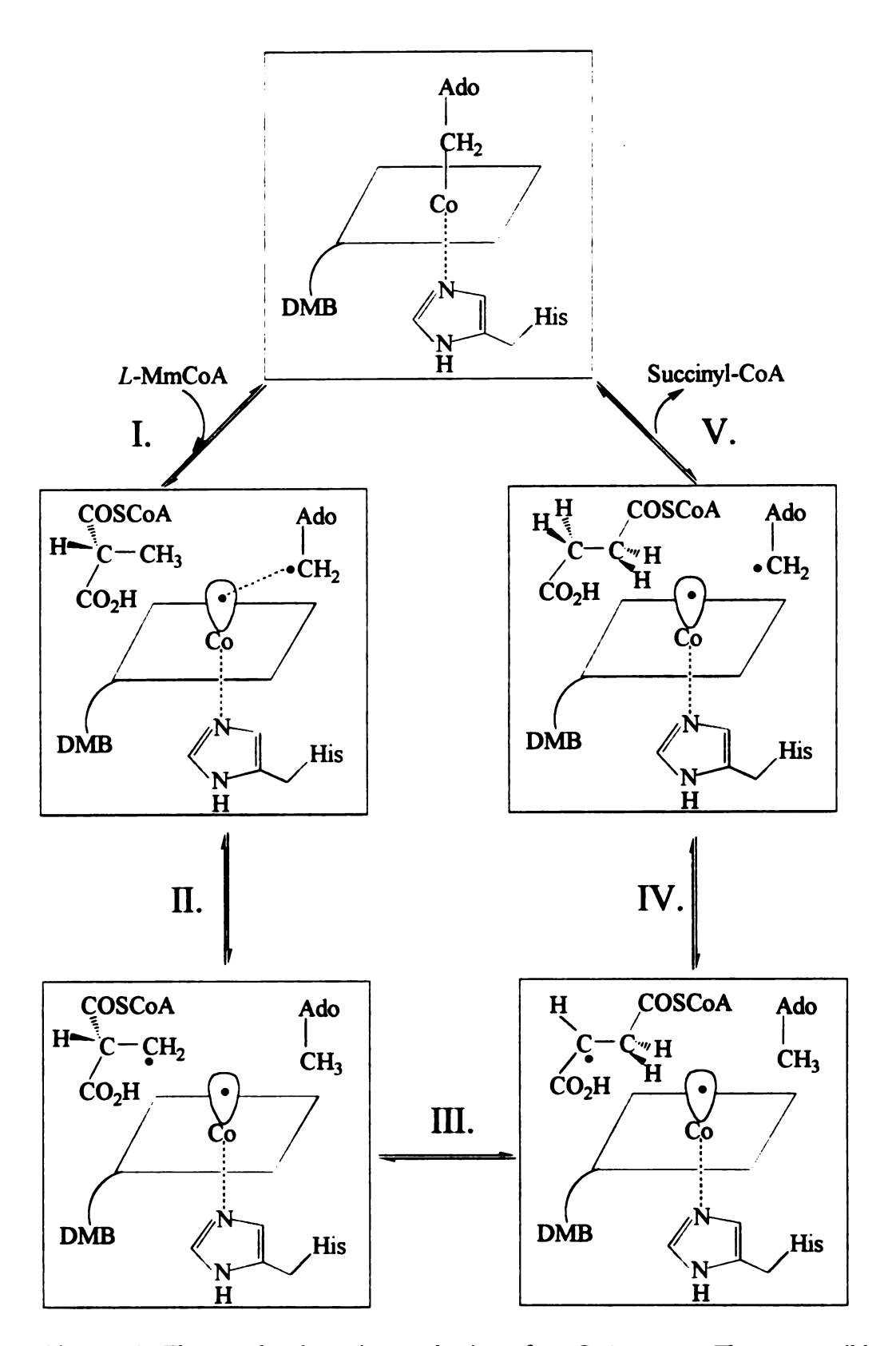


Figure 1.9: The postulated reaction mechanism of mmCoA mutase. The two possible radicals are either the deoxyadenosyl radical or a secondarily generated protein radical.

rearrangement reaction. This is the least understood of the three steps. The substrate rearranges to a more stable secondary radical on the product. Somehow, either via a free radical, a carbonium ion, a carbanion, or an organocobalt intermediate, the  $\alpha$ -carbon thioester group is switched to the  $\beta$ -carbon. After the substrate leaves, the cobalt atom of the cobalamin radical and the carbon atom of the adenosyl radical reform their bond.<sup>6</sup> A major question pertaining to this mechanism is whether the adenosyl radical abstracts the hydrogen atom alone, or if there is a secondary protein radical involved.

Electron paramagnetic spectroscopy provides an ideal tool for characterization of paramagnetic centers in complex chemical systems. In biological systems containing large molecules such as proteins, it can become difficult to obtain information about the paramagnetic center within the molecule. EPR spectroscopy removes this obstacle because it is only sensitive to the structure directly around the paramagnetic center. Ruma Banerjee and Rugmini Padmakumar have characterized the EPR properties of mmCoA mutase under several conditions. No EPR signal was detected for the apoenzyme, which is the form of the enzyme without the  $B_{12}$  cofactor, nor was an EPR signal detected for the holoenzyme, which is the form of the enzyme reconstituted with the B<sub>12</sub> cofactor. However, when either the substrate, L-methylmalonyl-CoA, or the product, succinyl-CoA was added to the holoenzyme and rapidly frozen in liquid nitrogen, an EPR signal was detected.<sup>6</sup> Figure 1.10<sup>6</sup> illustrates Baneriee's and Padmakumar's spectrum of the holoenzyme rapidly mixed with deuterated substrate. [CD<sub>3</sub>]methylmalonyl-CoA. The eight small peaks in the spectrum indicate hyperfine splittings resulting from coupling of the unpaired electron with the cobalt(II) nucleus. which has a spin of I = 7/2. This coupling between the unpaired electron and the

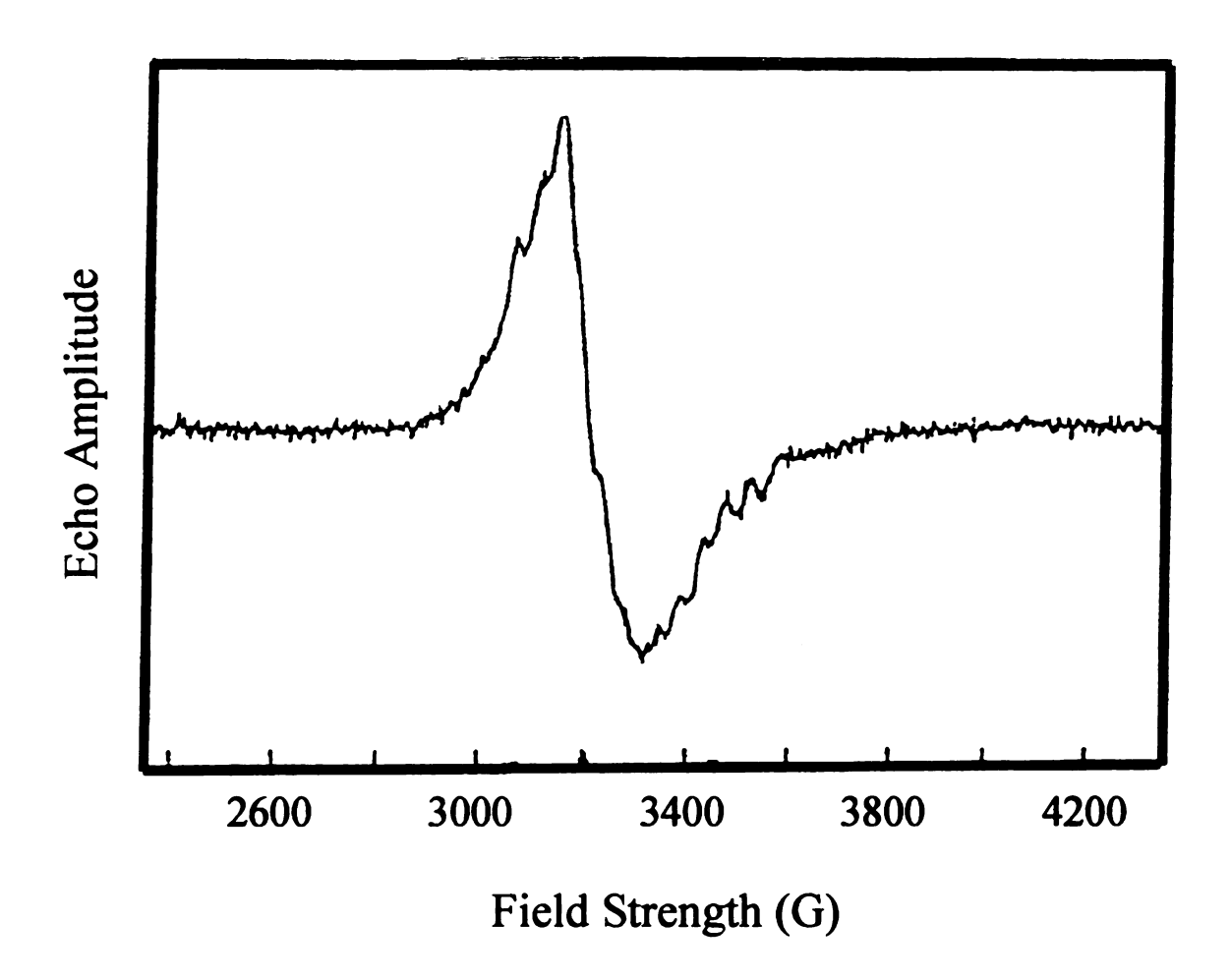


Figure 1.10: Banerjee and Padmakumar's EPR spectrum of the holoenzyme with deuterated substrate, [CD<sub>3</sub>]mmCoA. The eight small peaks are due to the hyperfine interaction between the unpaired electron and the cobalt(II) nucleus.

cobalt(II) nucleus is the result of hyperfine interaction, which is the interaction between the magnetic moment of the unpaired electron and the magnetic moment of the cobalt(II) nucleus. Other than the cobalt nucleus, it was not possible to determine any of the other species present since they were weakly coupled to the unpaired electron.

The purpose of this project was to determine what species were weakly coupled to the unpaired electron, and then to identify the radicals present in the sample of the enzyme with the substrate. One way to study weak couplings between an unpaired electron and surrounding nuclei with nuclear magnetic spins is by the electron spin echo envelope modulation (ESEEM) technique of pulsed EPR. Once the nuclei have been identified by ESEEM, they can be assigned by means of isotope labelling. Using both of these techniques, ESEEM and isotope labelling, more information regarding the identity of the radical species of mmCoA mutase can be obtained.

#### References

- 1. Zubay, Geoffrey. Biochemistry. Wm. C. Brown Publishers: Iowa, 1993.
- 2. Sigel, H., and A. Sigel. Metal Ions In Biological Systems. Marcel Dekker, Inc., New York: 1994, Vol. 30, pp. 1-24 and 255-278.
- 3. Matthews, R., et. al., Biochemistry, 1988, Vol. 27, pp. 8458-8465.
- 4. Mancia, et. al., Structure, 1996, Vol. 4, pp. 339-350.
- 5. Babcock, G., et. al., Acta Chemica Scandinavica, 1997, Vol. 51, pp. 533-540.
- 6. Banerjee, R., and R. Padmakumar, *The Journal of Biological Chemistry*, April 21, 1995, Vol. 270, No. 16, pp. 9295-9300.

## Chapter 2: Electron Paramagnetic Resonance Methods

The proposed reaction mechanism of the rearrangement reaction of L-mmCoA to succinyl-CoA involves radical species. One way to investigate radical systems is by EPR spectroscopy, or electron paramagnetic resonance spectroscopy. EPR is a spectroscopic technique allowing the study of molecules containing unpaired electrons by observing the magnetic fields at which the electron spin energy levels come into resonance with microwave radiation. An EPR spectrum is obtained by monitoring the microwave absorption at a fixed frequency as the magnetic field is swept.

In EPR, the interaction between the unpaired electron spin moment and the applied magnetic field is called the Zeeman effect. For the simplest paramagnetic system, which has a single unpaired electron such that the electronic spin quantum number  $S = \frac{1}{2}$ , the isotropic electronic Zeeman hamiltonian is

$$\hat{H} = g\beta B\hat{S}_{z} \tag{1}$$

where g is the electron g factor,  $\beta$  is the electron Bohr magneton, B is the applied field strength, and the operator of  $S_z$  is the electron spin operator in the direction of the field.

## Origin of the Zeeman Effect

Atoms have magnetic dipole moments due to the motion of their electrons, and each electron has its own intrinsic magnetic dipole moment associated with its spin. In paramagnetic materials, each atom has a permanent magnetic moment, which can be related to the angular momentum of the atom. In order to understand this relationship, it is necessary to derive the equation for the spherical harmonics, beginning with the classical model of the rigid rotor. Using the equation for the spherical harmonics, the

quantum mechanical operators for angular momentum, L and  $L_z$ , and spin angular momentum, S and  $S_z$ , are obtained.

## **Derivation Of the Spherical Harmonics**

When a particle rotates around a fixed axis as illustrated in Figure 2.1<sup>2</sup>, the particle has both angular momentum and rotational kinetic energy.<sup>2</sup> The kinetic energy is given by

$$KE = \frac{1}{2} mv^2 = p^2/2m$$
 (2)

where m is the mass of the particle, the momentum p = mv, and v is the linear velocity. The angular velocity is

$$v = 2\pi r v = r \omega \tag{3}$$

where v is the frequency of rotations, r is the radius of the circle of orbit, and the angular velocity  $\omega = d\theta/dt = 2\pi v$ . Therefore, the kinetic energy of a particle in circular motion about a fixed point in terms of angular velocity and angular momentum is

$$KE = \frac{1}{2} mr^2 \omega^2 = \frac{1}{2} I\omega^2$$
 (4)

where the moment of inertia  $I = mr^2$ . The angular momentum L is defined as

$$L = I\omega. (5)$$

Thus, the kinetic energy of rotational motion in terms of angular momentum is

$$KE_{rot} = \frac{1}{2} I\omega^2 = L^2/2I.$$
 (6)

When two particles rotate about their center of mass, as illustrated in Figure 2.2<sup>2</sup>, they satisfy the condition

$$m_1 r_1 = m_2 r_2 \tag{7}$$

where  $r_1$  is the distance of  $m_1$  from the center of mass, and  $r_2$  is the distance of  $m_2$  from the center of mass. Since the equilibrium distance R between the particles is

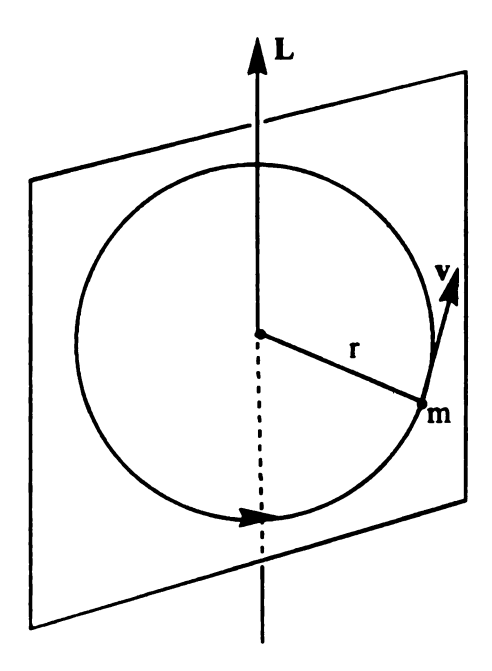


Figure 2.1: The rotation of a mass m about a fixed point. The mass is rotating at a distance r from the center with a velocity v, and has an angular momentum L perpendicular to the plane of rotation.

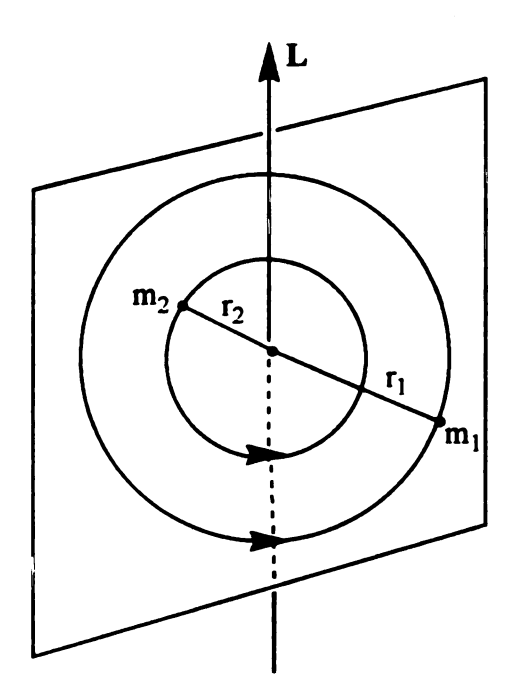


Figure 2.2: The rotation of a two particle system,  $m_1$  and  $m_2$ , about its center of mass. The particle  $m_1$  rotates at a distance  $r_1$  from the center of mass, while the particle  $m_2$  rotates at a distance  $r_2$  from the center of mass. The two particle system has an angular momentum L perpendicular to the plane of rotation.

$$R = r_1 + r_2, (8)$$

then from Equations (7) and (8) the following relationships for the radii can be obtained:

$$r_1 = [m_2/(m_1 + m_2)] R$$
 (9)

and

$$r_2 = [m_1/(m_1 + m_2)] R.$$
 (10)

The rotational kinetic energy for this two particle system is

$$KE_{rot} = \frac{1}{2} m_1 r_1^2 \omega^2 + \frac{1}{2} m_2 r_2^2 \omega^2$$

$$= \frac{1}{2} (m_1 r_1^2 + m_2 r_2^2) \omega^2$$

$$KE_{rot} = \frac{1}{2} I\omega^2$$
(12)

where  $I = [m_1m_2/(m_1 + m_2)]R^2$  after elimination of  $r_1$  and  $r_2$  by Equations (9) and (10). If we let  $m_1m_2/(m_1 + m_2) = \mu$ , then the moment of inertia can be rewritten as

$$I = \mu R^2 \tag{13}$$

where  $\mu$ , called the reduced mass, is defined as

$$1/\mu = 1/m_1 + 1/m_2 = (m_1 + m_2)/m_1m_2. \tag{14}$$

By using the reduced mass, the two body problem has been reduced to a one body problem. Therefore, the rotational kinetic energy of the two body system written in terms of angular momentum L becomes

$$KE_{rot} = L^2/(2I) = L^2/(2\mu R^2)^2$$
 (15)

The system of the rigid rotor has kinetic energy but no potential energy. In quantum chemistry, classical mechanical observables are represented as quantum mechanical operators. Therefore, the classical kinetic energy corresponds to the following quantum mechanical hamiltonian operator for rotational energy:

$$\hat{\boldsymbol{H}} = -\frac{\hbar^2}{2\mu} \nabla^2 \tag{16}$$

where the Laplacian operator  $\nabla^2$  is defined as

$$\nabla^2 = \frac{\partial^2}{\partial x^2} + \frac{\partial^2}{\partial y^2} + \frac{\partial^2}{\partial z^2}.$$
 (17)

As the energy of the rigid rotor is rotational, it is more convenient to use spherical polar coordinates, which are defined in Figure 2.3<sup>2</sup>. The Laplacian operator in spherical polar coordinates is

$$\nabla^2 = \frac{1}{\mathbf{R}^2} \frac{\partial}{\partial R} \left( \mathbf{R}^2 \frac{\partial}{\partial R} \right) + \frac{1}{\mathbf{R}^2 \sin^2 \theta} \frac{\partial^2}{\partial \phi^2} + \frac{1}{\mathbf{R}^2 \sin \theta} \frac{\partial}{\partial \theta} (\sin \theta \frac{\partial}{\partial \theta}). \tag{18}$$

In the model of the rigid rotor, R is constant because the two particles are at fixed distances from the origin. Therefore, all the derivative terms of R can be ignored, since the derivative of a constant is zero. Keeping this in mind, when Equation (18) is substituted into Equation (16), the hamiltonian operator for the rigid rotor becomes

$$\hat{H} = -\frac{\hbar^2}{2I} \left[ \frac{1}{\sin \theta} \frac{\partial}{\partial \theta} \left( \sin \theta \frac{\partial}{\partial \theta} \right) + \frac{1}{\sin^2 \theta} \frac{\partial^2}{\partial \phi^2} \right]$$
 (19)

where  $I = \mu R^2$ . Since the rigid rotor wavefunction is a function of the angles  $\theta$  and  $\phi$ , the eigenvalue problem to be solved is

$$-\frac{\hbar^2}{2I} \left[ \frac{1}{\sin \theta} \frac{\partial}{\partial \theta} \left( \sin \theta \frac{\partial}{\partial \theta} \right) + \frac{1}{\sin^2 \theta} \frac{\partial^2}{\partial \phi^2} \right] Y(\theta, \phi) = E Y(\theta, \phi). \tag{20}$$

The solutions  $Y(\theta, \phi)$  to this standard differential equation are called spherical harmonics.

Since the two quantum numbers  $\ell$  (angular momentum quantum number) and m (magnetic quantum number) arise in the solution of this eigenvalue equation, the wavefunctions are represented as

$$Y_{\ell}^{m}(\theta,\phi)$$
.

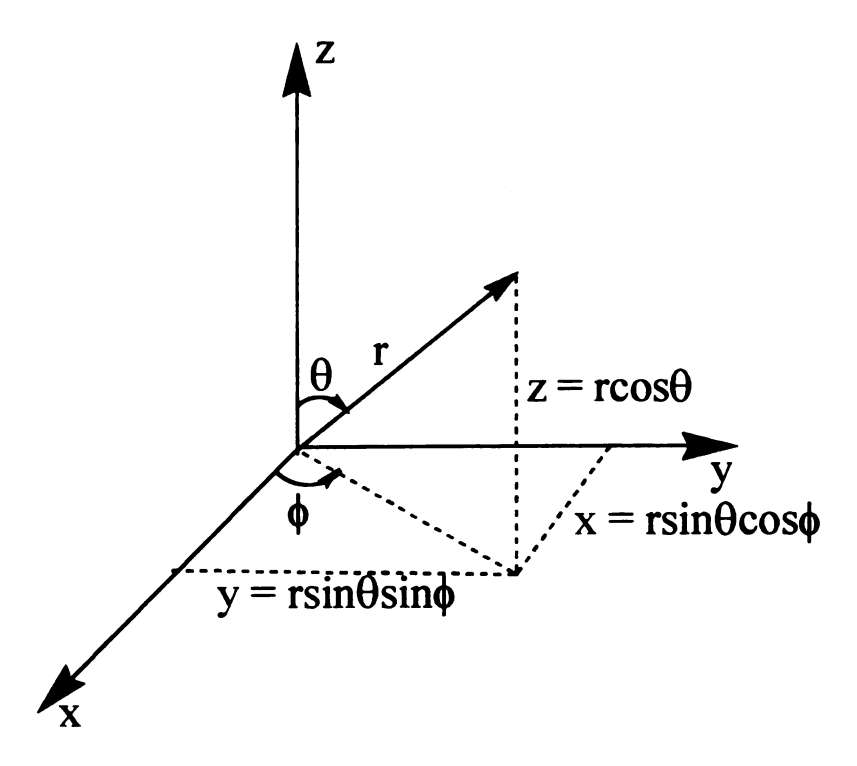


Figure 2.3: The relationship between the cartesian coordinates x, y, and z and the spherical polar coordinates r,  $\theta$ , and  $\phi$ .

In general, it is found that

$$\hat{\boldsymbol{H}} \; \mathbf{Y}_{\ell}^{m}(\boldsymbol{\theta}, \boldsymbol{\phi}) = \frac{\ell(\ell+1)\hbar^{2}}{2\mathbf{I}} \; \mathbf{Y}_{\ell}^{m}(\boldsymbol{\theta}, \boldsymbol{\phi}) \tag{21}$$

where  $\ell$  is the angular momentum quantum number (or azimuthal quantum number).

Therefore, the energies of the rigid rotor are given by

$$E = \frac{\ell(\ell+1)\hbar^2}{2I}$$
 (22)

where the angular momentum quantum number  $\ell = 0, 1, 2, ...$  etc.<sup>2</sup>

## Derivation Of the Angular Momentum Operators

Angular momentum is a vector that has components in the x, y, and z directions. Thus, in order to develop the quantum mechanical operators for angular momentum in the x, y, and z directions, it is necessary to begin with the classical expressions for angular momentum in all three dimensions.<sup>2</sup>

As illustrated in Figures  $2.1^2$  and  $2.2^2$ , the angular momentum of a particle or particles rotating about a fixed point is represented by the vector  $\mathbf{L}$  in the direction perpendicular to the plane of the circular motion. If a mass m rotates about a fixed point with linear velocity  $\mathbf{v}$ , the angular momentum  $\mathbf{L}$  is given by the cross product of the radius  $\mathbf{r}$  and the linear momentum vector  $\mathbf{p}$ ,

$$\mathbf{L} = \mathbf{r} \times \mathbf{m} \mathbf{v} = \mathbf{r} \times \mathbf{p} \tag{23}$$

where the cross product of the vectors  $\mathbf{r}$  and  $\mathbf{p}$  is a vector of magnitude  $|\mathbf{r}||\mathbf{p}|\sin\theta$ , and  $\theta$  is the angle between  $\mathbf{r}$  and  $\mathbf{p}$ . The vectors  $\mathbf{r}$  and  $\mathbf{p}$  can be expressed in terms of their components with the unit vectors

 $\hat{i}$ ,  $\hat{j}$ , and  $\hat{k}$ 

pointing along the x, y, and z axes respectively as follows:

$$\mathbf{r} = x\hat{\mathbf{i}} + y\hat{\mathbf{j}} + z\hat{\mathbf{k}} \tag{24}$$

and

$$\mathbf{p} = \mathbf{p}_{x} \hat{\mathbf{i}} + \mathbf{p}_{y} \hat{\mathbf{j}} + \mathbf{p}_{z} \hat{\mathbf{k}}. \tag{25}$$

Thus, a determinant can be set up in order to find the cross product of r and p, which gives the angular momentum L as

$$\mathbf{L} = \mathbf{r} \times \mathbf{p} = \begin{bmatrix} \hat{\mathbf{i}} & \hat{\mathbf{j}} & \hat{\mathbf{k}} \\ \mathbf{x} & \mathbf{y} & \mathbf{z} \\ \mathbf{p}_{x} & \mathbf{p}_{y} & \mathbf{p}_{z} \end{bmatrix} = (\mathbf{y}\mathbf{p}_{z} - \mathbf{z}\mathbf{p}_{y})\hat{\mathbf{i}} + (\mathbf{z}\mathbf{p}_{x} - \mathbf{x}\mathbf{p}_{z})\hat{\mathbf{j}} + (\mathbf{x}\mathbf{p}_{y} - \mathbf{y}\mathbf{p}_{x})\hat{\mathbf{k}}. \quad (26)$$

Therefore, the three components of the classical angular momentum of a particle rotating about a fixed point are

$$L_{x} = yp_{z} - zp_{y} \tag{27}$$

$$L_{v} = zp_{x} - xp_{z} \tag{28}$$

and

$$L_z = xp_y - yp_x. (29)$$

The square of the angular momentum,  $L^2$ , is found by taking the scalar product of L with itself:

$$L \cdot L = |L||L|\cos\theta = L^{2}(\cos \theta) = L^{2}(1) = L^{2} = L_{x}^{2} + L_{y}^{2} + L_{z}^{2}$$
 (30)

where L<sup>2</sup> is a scalar quantity.

In order to convert the classical angular momentum into its quantum mechanical operators, the quantities of  $L_x$ ,  $L_y$ , and  $L_z$  must be replaced with their corresponding quantum mechanical operators, namely

$$\hat{\mathbf{P}}_{x} = \frac{\hbar}{i} \frac{\partial}{\partial x} = -i\hbar \frac{\partial}{\partial x} \tag{31}$$

$$\hat{\mathbf{P}}_{y} = \frac{\hbar}{i} \frac{\partial}{\partial y} = -i\hbar \frac{\partial}{\partial y}$$
 (32)

and

$$\hat{\mathbf{P}}_{z} = \frac{\hbar}{i} \frac{\partial}{\partial z} = -i\hbar \frac{\partial}{\partial z}.$$
 (33)

Therefore, the angular momentum operators for the x, y, and z components are

$$\hat{\mathbf{L}}_{x} = -i\hbar(\mathbf{y}\frac{\partial}{\partial \mathbf{z}} - \mathbf{z}\frac{\partial}{\partial \mathbf{y}}) \tag{34}$$

$$\hat{\mathbf{L}}_{y} = -i\hbar(\mathbf{z}\frac{\partial}{\partial \mathbf{x}} - \mathbf{x}\frac{\partial}{\partial \mathbf{z}})$$
(35)

and

$$\hat{\mathbf{L}}_{z} = -i\hbar(\mathbf{x}\frac{\partial}{\partial \mathbf{y}} - \mathbf{y}\frac{\partial}{\partial \mathbf{x}}). \tag{36}$$

The quantum mechanical operator for the square of the angular momentum is

$$\hat{\mathbf{L}}^2 = |\hat{\mathbf{L}}|^2 = \hat{\mathbf{L}} \cdot \hat{\mathbf{L}} = \hat{\mathbf{L}}_x^2 + \hat{\mathbf{L}}_y^2 + \hat{\mathbf{L}}_z^2. \tag{37}$$

As mentioned earlier, since the system is rotational it is more convenient to write the angular momentum operators in spherical polar coordinates (see Figure 2.3<sup>2</sup>), which are

$$\hat{\mathbf{L}}_{x} = i\hbar(\sin\phi \frac{\partial}{\partial\theta} + \cot\theta \cos\phi \frac{\partial}{\partial\phi}) \tag{38}$$

$$\hat{\mathbf{L}}_{y} = i\hbar(-\cos\phi\frac{\partial}{\partial\theta} + \cot\theta\sin\phi\frac{\partial}{\partial\phi}) \tag{39}$$

$$\hat{\mathbf{L}}_{z} = -i\hbar \frac{\partial}{\partial \phi} \tag{40}$$

and

$$\hat{\mathbf{L}}^2 = -\hbar^2 \left[ \frac{1}{\sin \theta} \frac{\partial}{\partial \theta} (\sin \theta \frac{\partial}{\partial \theta}) + \frac{1}{\sin^2 \theta} \frac{\partial^2}{\partial \phi^2}) \right]. \tag{41}$$

It is important to note here that the operators for  $L_x$  and  $L_y$ ,  $L_y$  and  $L_z$ , and  $L_z$  and  $L_z$  do not commute with each other. However, the operators for  $L_x$ ,  $L_y$ , and  $L_z$  each commute with the operator for  $L^2$ . This implies that one can measure precisely the square of the total angular momentum and only one of the components of the angular momentum. For example, if the magnitude of the total angular momentum, which is defined as

$$|\mathbf{L}| = \sqrt{\mathbf{L}^2} = \sqrt{\mathbf{L}_x^2 + \mathbf{L}_y^2 + \mathbf{L}_z^2}$$
 (42)

is measured, and  $L_z$  is also measured, then it is not possible to measure  $L_x$  and  $L_y$  precisely. Thus, the eigenfunction of  $L^2$  is an eigenfunction of  $L_z$ , but not an eigenfunction of  $L_x$  or  $L_y$  as they do not commute with  $L_z$ . This is a major difference between classical and quantum mechanical systems.<sup>2</sup>

Since the operators for  $L^2$  and  $L_z$  commute, a function can be constructed that is an eigenfunction of both operators. These wavefunctions are called the spherical harmonics, and were seen in Equation (21) for the energy of a rigid rotor. For the classical rigid rotor,

$$L^2 = 2I(KE) \tag{43}$$

while for the quantum mechanical operator

$$\hat{\mathbf{L}}^2 = 2\mathbf{I}(\hat{\boldsymbol{H}}). \tag{44}$$

Therefore, the eigenvalue equation for the square of the angular momentum becomes

$$\hat{\mathbf{L}}^2 \mathbf{Y}_{\ell}^{m}(\boldsymbol{\theta}, \boldsymbol{\phi}) = \ell(\ell+1)\hbar^2 \mathbf{Y}_{\ell}^{m}(\boldsymbol{\theta}, \boldsymbol{\phi})$$
 (45)

where the angular momentum quantum number  $\ell = 0, 1, 2, ...$  etc. According to Equation (45), the total angular momentum squared for a rigid rotor can only have the following values:

$$\mathbf{L}^2 = \ell(\ell+1)\hbar^2 \tag{46}$$

where  $\ell = 0, 1, 2, \dots$  etc. Similarly, when operating on the spherical harmonics with the z-component of the angular momentum operator of  $L_z$  using the equation

$$\hat{\mathbf{L}}_{z}\mathbf{Y}_{t}^{m}(\theta,\phi) = m\hbar\mathbf{Y}_{t}^{m}(\theta,\phi) \tag{47}$$

where the magnetic quantum number  $m = -\ell$ ,  $-\ell+1,...$ ,  $\ell-1,\ell$ , the corresponding eigenvalues for  $L_z$  are

$$L_z = m\hbar \tag{48}$$

where  $m = -\ell, -\ell+1, ..., \ell-1, \ell$ .

Thus, since the spherical harmonics are eigenfunctions for the two commuting operators of  $L^2$  and  $L_z$ , they can be used to find the corresponding angular momentum eigenvalues. The spherical harmonics were in terms of the two coordinates  $\theta$  and  $\phi$ , so only two quantum numbers were seen in the eigenvalues. The eigenvalue of the operator of  $L^2$  was in terms of the angular momentum quantum number  $\ell$ , and the eigenvalue of the operator for  $L_z$  was in terms of the magnetic quantum number m. These two quantum numbers are related in that an angular momentum vector has a value for  $\ell$ , and for each value of  $\ell$ , the quantum number m has the values  $-\ell, ..., 0, ..., +\ell$ . Therefore, in the absence of an electric or magnetic field, there is a degeneracy of  $2\ell + 1$  orientations for the angular momentum vector.<sup>2</sup>

Deriving the Zeeman Energy From A Hydrogen-Like Atom ( $S = \frac{1}{2}$ )

As seen in Equation (45) of the rigid rotor, the square of the magnitude of the angular momentum is found by operating on the hydrogenlike wavefunction with the operator of L<sup>2</sup>. Since the wavefunction is

$$R(r)Y_{l}^{m}(\theta,\phi)$$

and the operator of  $L^2$  only operates on  $\theta$  and  $\phi$ , the eigenvalue of  $L^2$  was found and given in Equation (46). Thus, for a hydrogenlike atom, the only values for angular momentum are

$$\mathbf{L} = \sqrt{\ell(\ell+1)}\hbar\tag{49}$$

where  $\ell = 0, 1, 2, ...,$  etc. It was also shown in Equation (48) from the rigid rotor that the z-component of angular momentum  $L_z$  is in terms of the magnetic quantum number m, which describes the orientation of the angular momentum vector. In the absence of a magnetic field and not including the spin of the electron (which is also a kind of angular momentum), the energy of the hydrogenlike atom is independent of m. However, in the presence of a magnetic field, the energy does depend on m.

For each value of  $\ell$ , there are  $2\ell + 1$  different values of m, each corresponding to a different value of energy. In the presence of a magnetic field the  $2\ell + 1$  degeneracy with respect to m is removed, because when an atom has angular momentum L, the atom acts like a small magnet. In other words, the atom has a magnetic dipole moment  $\mu$ , given by

$$\mu = \gamma_c L \tag{50}$$

where the gyromagnetic ratio  $\gamma_e$  is defined as

$$\gamma_e = -e/(2m_e) \tag{51}$$

where m<sub>e</sub> is the mass of the electron and e is the charge of the electron. The z-component of the dipole moment is

$$\mu_z = -[e/(2m_e)] L_z.$$
 (52)

Substituting the value of L<sub>z</sub> from Equation (48), Equation (52) becomes

$$\mu_z = -[e\hbar/(2m_e)] m = -\mu_B m$$
 (53)

where the Bohr magneton  $\mu_B$  (also known as  $\beta_e$ ) is defined as

$$\mu_{\rm B} = e\hbar/(2m_{\rm e}) \tag{54}$$

and is the natural unit of magnetic dipole moment for electronic states.<sup>2</sup>

When a magnetic dipole is placed in a magnetic field oriented along a given direction, the potential energy is given by

$$\mathbf{E} = -\mathbf{\mu} \bullet \mathbf{B} \tag{55}$$

where **B** is the magnetic flux density. If the z direction is chosen to be along **B** so that  $B_z = B$ , then the energy becomes

$$E = -\mu_z B = [eB/(2m_e)] L_z.$$
 (56)

The hamiltonian operator for a hydrogenlike atom in a magnetic field is found by adding the potential energy of Equation (56) to the hamiltonian in the absence of the magnetic field:

$$\hat{\boldsymbol{H}} = \hat{\boldsymbol{H}}_0 + \frac{\mathbf{eB}}{2\mathbf{m}} \hat{\mathbf{L}}_z. \tag{57}$$

When the hamiltonian of Equation (57) is applied to the eigenfunctions of a hydrogenlike atom (the eigenfunctions of the hamiltonian in the absence of a magnetic field), it is found that these functions are also eigenfunctions of the above complete hamiltonian with the following eigenvalues:

$$E_{n\ell m} = -\frac{m_{e}e^{4}z^{2}}{2(4\pi\varepsilon_{0})^{2}n^{2}\hbar^{2}} + \mu_{B}mB$$
 (58)

where z is the atomic number of the atom,  $\varepsilon_0$  is the permittivity of vaccum, the principle quantum number n = 1, 2, 3, ..., etc., the angular momentum quantum number  $\ell = 0, 1, 2, ..., \text{etc.}$ , and the magnetic quantum number  $m = \ell, \ell-1, ..., -\ell$ . The second term of the energy in Equation (58) implies that in the presence of a magnetic field, the energy levels

have been split into  $2\ell + 1$  levels. When spectral lines are split due to a magnetic field, it is called the Zeeman effect.<sup>2</sup>

Deriving the Two Spin Energy States For An Electron

It was proposed in 1925 that an electron has an intrinsic angular momentum S. Since the spin angular momentum of an electron has no analog in classical mechanics, the spin angular momentum operators cannot be constructed by first writing the classical hamiltonian. However, the treatment of spin angular momentum is very similar to the treatment of orbital angular momentum.<sup>2</sup>

The magnitude of the spin angular momentum S is

$$S = \sqrt{s(s+1)} \, \hbar = \frac{\sqrt{3}}{2} \, \hbar \tag{59}$$

where the spin quantum number s (also referred to as the spin) of the electron has the single value of  $\frac{1}{2}$ . The z-component of the spin angular momentum  $S_z$  is

$$S_z = m_s \hbar \tag{60}$$

where the quantum number m<sub>s</sub> for the z-component has two possible eigenvalues, +½ and -½ (also referred to as "spin-up" and "spin-down" respectively). This implies that the electron spin angular momentum has only two orientations.<sup>2</sup>

The corresponding spin angular momentum operators of S and  $S_z$  can be applied to spin functions to yield eigenvalues. However, since the spin eigenfunctions do not involve spatial coordinates, the two possible spin functions are represented by  $\alpha$  and  $\beta$ . Thus, the eigenfunction equations for the spin angular momentum are

$$\hat{\mathbf{S}}^{2} |\alpha\rangle = \frac{1}{2} (\frac{1}{2} + 1) \hbar^{2} |\alpha\rangle = \frac{3}{4} \hbar^{2} |\alpha\rangle$$
 (61)

$$\hat{\mathbf{S}}^{2} |\beta\rangle = \frac{1}{2} (\frac{1}{2} + 1) \hbar^{2} |\beta\rangle = \frac{3}{4} \hbar^{2} |\beta\rangle$$
 (62)

$$\hat{\mathbf{S}}_{z}|\alpha\rangle = +\frac{1}{2}\hbar|\alpha\rangle \tag{63}$$

and

$$\hat{\mathbf{S}}_{z}|\beta\rangle = -\frac{1}{2}\hbar|\beta\rangle. \tag{64}$$

It should be noted that under the same argument given for the components of the orbital angular momentum, the components  $S_x$  and  $S_y$  cannot be determined simultaneously with  $S_z$  since  $S_x$  and  $S_y$  do not commute with  $S_z$ .<sup>2</sup>

Due to its charge and intrinsic spin angular momentum, an electron has a magnetic dipole moment  $\mu_s$ , which is proportional to its spin angular momentum S:

$$\mu_s = -[g_e e/(2m_e)] S$$
 (65)

where the electron g factor  $g_e = 2.002322$  for a free electron. The component of the magnetic moment of the electron in the direction of the applied magnetic field is

$$\mu_z = -[g_e e/(2m_e)] S_z$$
 (66)

where S<sub>z</sub> is the component of the spin angular momentum in the direction of the field.

Substituting Equation (60) into Equation (66), the magnetic moment in the direction of the field becomes

$$\mu_z = -[g_e e\hbar/(2m_e)] m_s.$$
 (67)

From Equation (56) where the potential energy is given as  $E = -\mu_z B$ , the energy of the spin magnetic moment in a magnetic field B is found to be

$$E = g_e \mu_B m_s B. \tag{68}$$

Since the quantum number m<sub>s</sub> has the two values +½ and -½, the electron spin has the following two energy states in a magnetic field:

$$E = +\frac{1}{2}g_e\mu_B B \tag{69}$$

and

$$E = -\frac{1}{2}g_e\mu_B B. \tag{70}$$

It is the transition between these two levels that is studied in electron spin resonance.<sup>2</sup>

Figure 2.4 illustrates that as the external magnetic field of the system is increased, the splitting of the two energy levels ( $m_s = +\frac{1}{2}$ ,  $-\frac{1}{2}$ ) of the unpaired electron increases. As the microwave radiation is applied at a constant frequency, the resonance condition is achieved at only one field value at a time. The magnitude of the transition shown in Figure 2.4 is the energy that must be absorbed from the oscillating magnetic field B to move from the lower to the upper state.<sup>3</sup>

#### The Nuclear Zeeman Interaction

Just as an electron has a spin associated with it, the nucleus of an atom also has a spin associated with it due to its protons and neutrons. The nuclear spin interacts with the magnetic field for the same reasons that the electron spin does, and this interaction is the nuclear Zeeman effect. The nuclear spin hamiltonian is

$$\hat{\boldsymbol{H}} = -\mathbf{g}_{n} \boldsymbol{\beta}_{n} \mathbf{B} \hat{\mathbf{I}}_{n} \tag{71}$$

where  $g_n$  is the nuclear g factor,  $\beta_n$  is the nuclear magneton, B is the applied magnetic field, and the operator of  $I_z$  is the nuclear spin operator. The nuclear Zeeman energy term is opposite in sign and smaller in magnitude than the electron Zeeman energy term.

For a nucleus, the total spin angular momentum is I, the spin quantum number is I, and the component of nuclear spin in the z direction is  $I_z$ . Just like S for electrons, I is an angular momentum, and thus the eigenvalue of  $I^2$  is given by  $I(I + 1)\hbar^2$ . It follows that the magnitude of I is

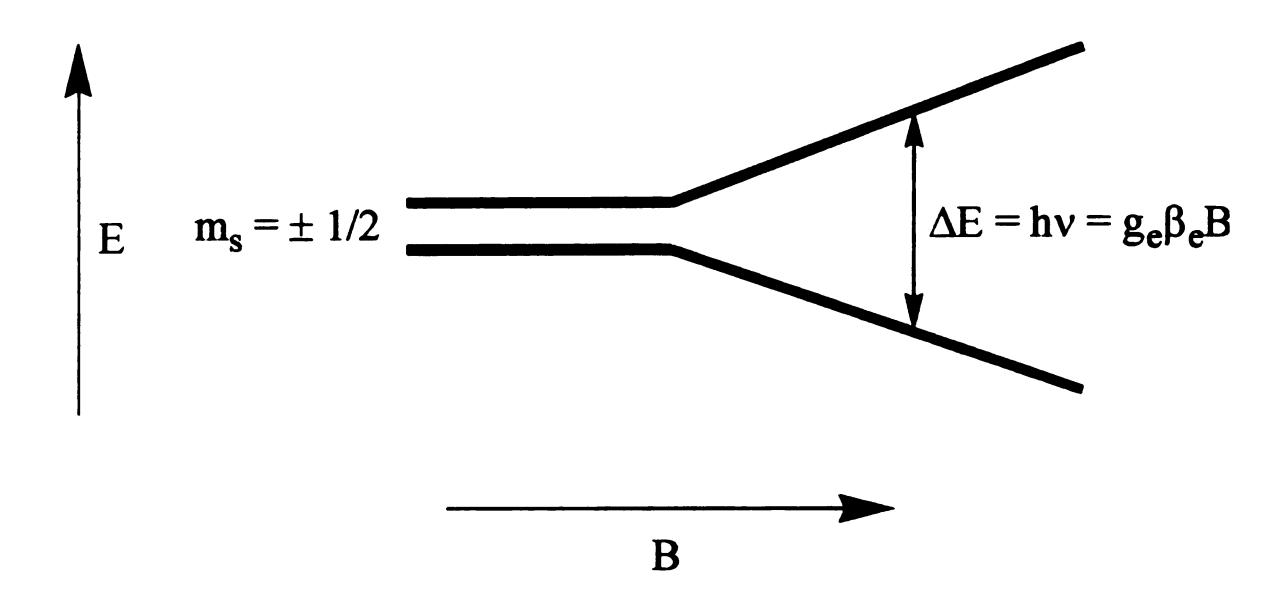


Figure 2.4: For an  $S = \frac{1}{2}$  system, the two degenerate electronic energy levels split further and further apart as the applied magnetic field is increased.

$$|\mathbf{I}| = \sqrt{\mathbf{I}(\mathbf{I} + \mathbf{1})} \, \hbar. \tag{72}$$

Similarly, the eigenvalues of  $I_z$  are  $m_I\hbar$ , where  $m_I = -I, -I+1, ..., 0, ..., I-1, I$ . Therefore, there are 2I+1 values of  $m_I$ , each associated with an eigenstate of  $I^2$  and  $I_z$ .<sup>2</sup>

As with the case of the electron, the magnetic dipole moment of the nucleus is proportional to the spin angular momentum, where

$$\mu = [g_n e/(2m_p)] I \tag{73}$$

where  $g_n$  is the nuclear g factor,  $m_p$  is the mass of the proton, and e is the elementary charge. Depending on the sign of the nuclear g factor,  $\mu$  and I can either be parallel or antiparallel. If  $g_n$  is positive, then  $\mu$  and I are parallel, while a negative  $g_n$  implies the two are antiparallel.

Since I is in units of  $\hbar$ , the basic unit of nuclear dipole moment, which is the nuclear magneton  $\mu_N$  (also known as  $\beta_n$ ), can be defined as

$$\mu_{\rm N} = e\hbar/(2m_{\rm p}). \tag{74}$$

Using Equation (74), the z-component of the nuclear dipole moment is

$$\mu_z = [g_n e/(2m_p)] m_l \hbar = g_n \mu_N m_l.$$
 (75)

Equation (55) defines the energy of a magnetic dipole in an external magnetic field **B** as -μ•**B**. If the z direction is chosen to be along the field, then

$$E = -\mu_z B = -g_n \mu_N m_i B \tag{76}$$

where  $m_I = -I, -I+1, ..., 0, ..., I-1, I$ . Thus a nucleus with spin I has 2I + 1 nondegenerate energy states in a magnetic field. Transitions among these levels are induced by applying electromagnetic radiation, with the frequency equal to the energy level spacings. The

selection rule for these transitions is  $\Delta m_I = 0$ , and the frequency  $\nu$  of the transitions is given by

$$v = \Delta E/h = g_n \mu_n B/h \tag{77}$$

which is called the Larmor frequency. There is only one Larmor frequency because the energy levels are equally spaced. Figure 2.5 illustrates the energy levels of a single proton in a magnetic field, which is the simplest case of  $I = \frac{1}{2}$ . Unlike the case of the electron, the proton has the lower energy when it is parallel to the field  $(m_I = +\frac{1}{2})$ , and has the higher energy when it is antiparallel to the field  $(m_I = -\frac{1}{2})^2$ .

Electron Nuclear Hyperfine Interaction: Isotropic and Anisotropic

The electron nuclear hyperfine interaction is an interaction between the magnetic moments of the unpaired electron and the nuclei. The electron spin not only interacts with the applied magnetic field, but also with the weak local magnetic fields arising from the magnetic moments of nearby nuclei, as illustrated in Figure 2.6. The result of this interaction on an EPR spectrum is hyperfine structure, which is the splitting of individual resonance lines into components. There are two contributions to the hyperfine interaction. The first is a Fermi contact interaction, which is isotropic, meaning that the density of the electron is at the nucleus. Since this component of the hyperfine is isotropic, changing the sample orientation relative to the magnetic field B does not alter the EPR spectrum. The second contribution to the hyperfine is a dipole-dipole interaction, which is anisotropic, meaning that the energy level separations are strongly dependent on the orientation of the molecule in the applied magnetic field.

If the electron and nuclear dipoles in Figure 2.6 were to behave classically with the applied magnetic field **B** in the z direction, then the classical energy of the dipole-

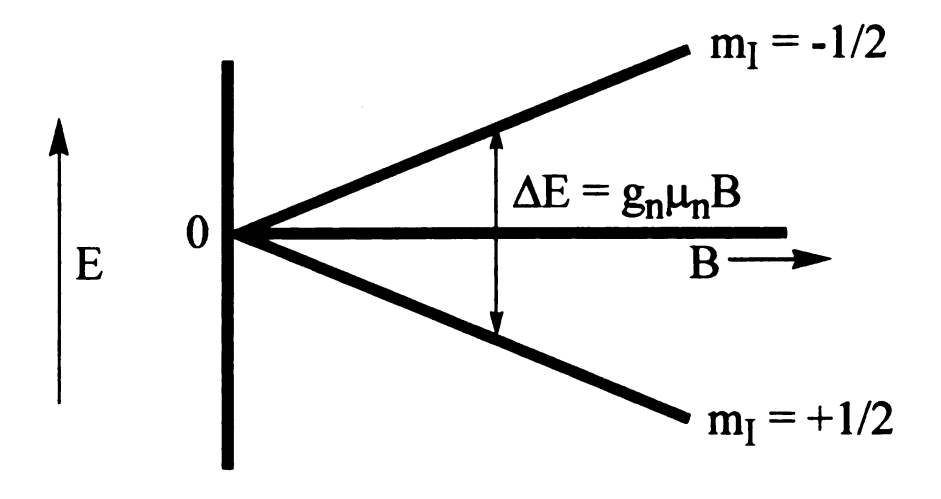


Figure 2.5: The energy levels of a proton with  $I = \frac{1}{2}$  in a magnetic field.

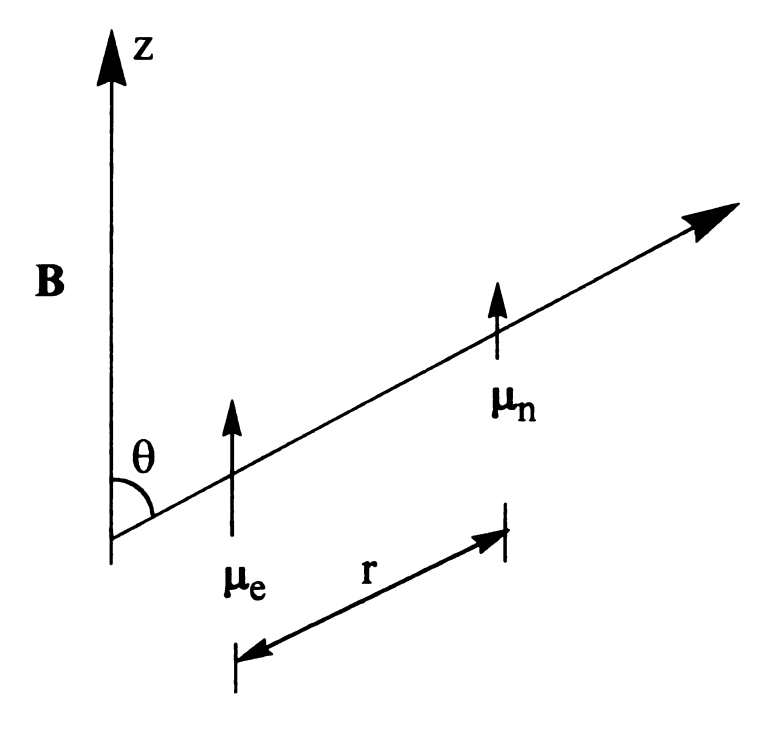


Figure 2.6: The vector for the electron magnetic dipole moment  $\mu_e$  will feel a local field from the vector for the nuclear magnetic dipole moment  $\mu_n$ . **B** is the applied magnetic field and  $\theta$  is the angle between the applied field and the axis of the two magnetic moments. The distance between the two dipoles is r. (The vector  $\mu_e$  represents the state  $m_s = -\frac{1}{2}$ , and the vector  $\mu_n$  represents the state  $m_l = +\frac{1}{2}$ .

dipole interaction between them is given by

$$E_{\text{dipolar}} = -\frac{\mu_{\circ}}{4\pi} \frac{3\cos^2\theta - 1}{r^3} \mu_{nz} \mu_{ez} = -B_{\text{local}} \mu_{ez}$$
 (78)

where  $\mu_o$  is the permeability of vaccum, and  $\mu_{ez}$  and  $\mu_{nz}$  are the components of the electron and nuclear dipole moments along the direction of the applied magnetic field. The two dipoles are separated by a distance r, and  $\theta$  is the angle between B and the line joining the two dipoles.  $B_{local}$ , the local field at the electron caused by the nucleus, can either enhance or diminish the externally applied magnetic field depending on the values of  $\theta$  and r.

The electron is not localized at one position in space since it is in an orbital. Therefore, the interaction energy must be averaged over the electron probability distribution function. If all values of  $\theta$  are possible, such as the case of an electron in an s orbital, then the average local field at each r can be obtained by first averaging  $\cos^2\theta$  over a sphere by the following multivariable integration:

$$\left\langle \cos^2 \theta \right\rangle = \frac{\int_0^{2\pi} \int_0^{\pi} \cos^2 \theta \sin \theta d\theta d\phi}{\int_0^{2\pi} \int_0^{\pi} \sin \theta d\theta d\phi} = \frac{1}{3}$$
 (79)

where  $\sin\theta d\theta d\phi$  is the element of surface area on a sphere in spherical polar coordinates. When the result of Equation (79) is substituted into Equation (78), it can be seen that the local field  $B_{local}$  becomes zero. This is the case of the isotropic hyperfine interaction.<sup>3</sup>

The hamiltonian for the electron nuclear hyperfine interaction is

$$\hat{H} = \hat{\mathbf{S}} \bullet \mathbf{A} \bullet \hat{\mathbf{I}} \tag{80}$$

where A is the hyperfine coupling matrix. In an axial system,  $A_{xx} = A_{yy} = A_{\perp}$  and  $A_{zz} = A_{\parallel}$ . In an isotropic system such as the case of a hydrogen nucleus interacting with an

electron,  $A_1 = A_{\parallel}$ , and thus  $A_x = A_y = A_z$ . Therefore, the hamiltonian of Equation (80) for an isotropic system becomes

$$\hat{\boldsymbol{H}} = (\hat{\mathbf{S}}_{x} \hat{\mathbf{S}}_{y} \hat{\mathbf{S}}_{z}) \begin{pmatrix} \mathbf{A} & 0 & 0 \\ 0 & \mathbf{A} & 0 \\ 0 & 0 & \mathbf{A} \end{pmatrix} \begin{pmatrix} \hat{\mathbf{I}}_{x} \\ \hat{\mathbf{I}}_{y} \\ \hat{\mathbf{I}}_{z} \end{pmatrix}$$
(81)

where A is a scalar. If the electron spin is directed along B in the z direction, then

$$\hat{\boldsymbol{H}} = \mathbf{A} (0 \, 0 \, \hat{\mathbf{S}}_z) (\mathbf{1}) \begin{pmatrix} \hat{\mathbf{I}}_x \\ \hat{\mathbf{I}}_y \\ \hat{\mathbf{I}}_z \end{pmatrix}. \tag{82}$$

Therefore, the hamiltonian for the isotropic hyperfine interaction is

$$\hat{H}_{180} = A \hat{S}, \hat{I}, \tag{83}$$

where A is the isotropic hyperfine coupling constant. This constant measures the magnetic interaction energy between the electron and nucleus, and is often expressed as A/h in units of frequency (MHz). It can also be expressed in magnetic field units (mT) as  $a = A/(g_e\beta_e)$ , which is called the hyperfine splitting constant. For the present system of S =  $\frac{1}{2}$  and I =  $\frac{1}{2}$ , two peaks would be expected in the absorption spectrum because a spin I nucleus splits the spectrum into  $2\pi I + 1$  hyperfine lines of equal intensity. Figure 2.7 illustrates what the derivative spectrum would look like for a hydrogen nucleus interacting with an electron.

In the case of isotropic hyperfine, all values of  $\theta$  were equally probable in Equation (78) for the dipolar energy. However, in systems where the molecule is not free to tumble such as in solid samples, all values of  $\theta$  are not equally probable, and  $B_{local}$  does not vanish. In such cases, there is anisotropy in the hyperfine caused by the dipolar interaction between the electron and nucleus.<sup>3</sup> In a system with  $S = \frac{1}{2}$  and  $I = \frac{1}{2}$ , the

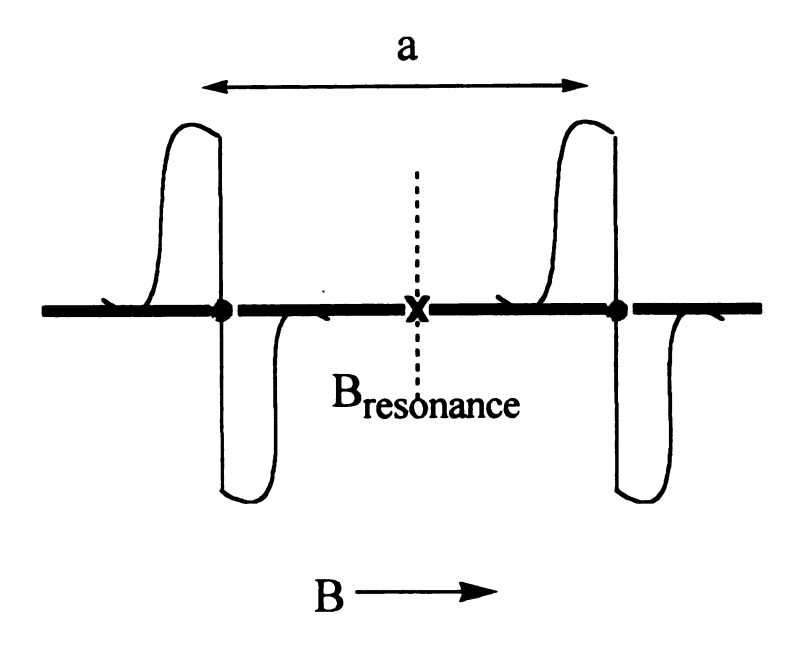


Figure 2.7: The derivative spectrum of a nucleus with  $I = \frac{1}{2}$  interacting with an electron in an isotropic system. The constant a is the hyperfine splitting constant, and the resonant field value  $B_{\text{resonance}} = h\nu/(g\beta) \pm a/2$ .

derivative spectrum for an anisotropic system is shown in Figure 2.8. The figure illustrates that unlike an isotropic system,  $A_{\perp} \neq A_{\parallel}$ .

The classical expression for the dipolar interaction energy between an electron and nucleus separated by a distance r is

$$E_{\text{dipolar}}(\mathbf{r}) = \frac{\mu_{\circ}}{4\pi} \left[ \frac{\mu_{\circ}^{\mathsf{T}} \bullet \mu_{n}}{r^{3}} - \frac{3(\mu_{\circ}^{\mathsf{T}} \bullet \mathbf{r})(\mu_{n}^{\mathsf{T}} \bullet \mathbf{r})}{r^{5}} \right]$$
(84)

where r represents the vector joining the magnetic dipoles of the unpaired electron and the nucleus, illustrated in Figure 2.6. The vectors  $\mu_e$  and  $\mu_n$  are the classical electron and nuclear magnetic moments, and the superscript <sup>T</sup> is to indicate the transpose. For the corresponding quantum mechanical system, the magnetic moment vectors in Equation (84) must be replaced by their operators. The hamiltonian can thus be written as

$$\hat{H}_{\text{dipolar}}(\mathbf{r}) = -\frac{\mu_{\text{o}}}{4\pi} \mathbf{g} \boldsymbol{\beta}_{\text{e}} \mathbf{g}_{\text{n}} \boldsymbol{\beta}_{\text{n}} \left[ \frac{\hat{\mathbf{S}}^{\mathsf{T}} \bullet \hat{\mathbf{I}}}{r^{3}} - \frac{3(\hat{\mathbf{S}}^{\mathsf{T}} \bullet \mathbf{r})(\hat{\mathbf{I}}^{\mathsf{T}} \bullet \mathbf{r})}{r^{5}} \right]. \tag{85}$$

By expanding the vectors in Equation (85), the dipolar hamiltonian becomes

$$\hat{H}_{dipolar}(\mathbf{r}) = -\frac{\mu_{o}}{4\pi} g \beta_{e} g_{n} \beta_{n} \begin{bmatrix} \frac{r^{2} - 3x^{2}}{r^{5}} \hat{\mathbf{S}}_{x} \hat{\mathbf{I}}_{x} + \frac{r^{2} - 3y^{2}}{r^{5}} \hat{\mathbf{S}}_{y} \hat{\mathbf{I}}_{y} + \frac{r^{2} - 3z^{2}}{r^{5}} \hat{\mathbf{S}}_{z} \hat{\mathbf{I}}_{z} - \frac{3xy}{r^{5}} (\hat{\mathbf{S}}_{x} \hat{\mathbf{I}}_{y} + \hat{\mathbf{S}}_{y} \hat{\mathbf{I}}_{x}) - \frac{3xz}{r^{5}} (\hat{\mathbf{S}}_{x} \hat{\mathbf{I}}_{z} + \hat{\mathbf{S}}_{z} \hat{\mathbf{I}}_{x}) - \frac{3yz}{r^{5}} (\hat{\mathbf{S}}_{y} \hat{\mathbf{I}}_{z} + \hat{\mathbf{S}}_{z} \hat{\mathbf{I}}_{y})$$
(86)

where g is assumed to be isotropic.<sup>3</sup> (For an anisotropic g,  $g_{\perp} \neq g_{\parallel}$ , where  $g_{\perp}$  and  $g_{\parallel}$  correspond to  $A_{\perp}$  and  $A_{\parallel}$  respectively.) Since the hamiltonian is applied to an electron in an orbital, the quantities in brackets must be averaged over the electron spatial distribution. The following spin hamiltonian in matrix notation becomes

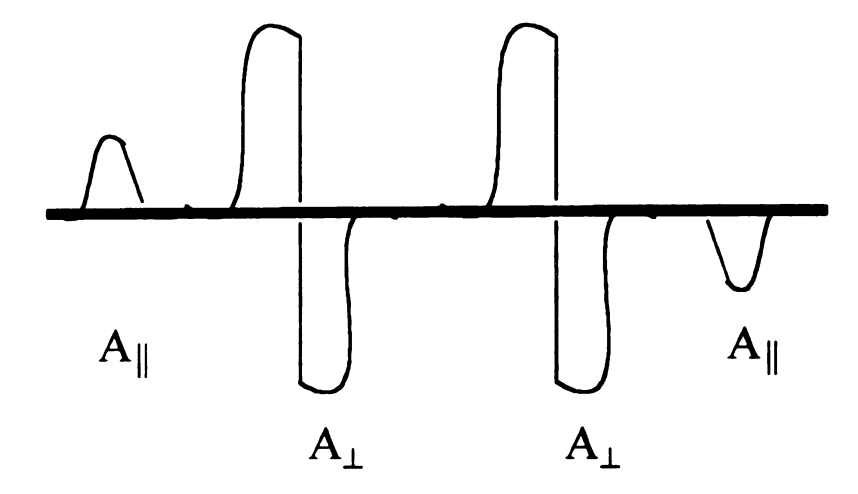


Figure 2.8: The derivative spectrum of a nucleus  $I=\frac{1}{2}$  interacting with an electron in an anisotropic system. It can be seen that  $A_1$  is not equal to  $A_{\parallel}$ .

$$\hat{\boldsymbol{H}}_{dipolar} = -\frac{\mu_{o}}{4\pi} g \beta_{e} g_{n} \beta_{n} \times \left[\hat{\boldsymbol{S}}_{x} \quad \hat{\boldsymbol{S}}_{y} \quad \hat{\boldsymbol{S}}_{z}\right] \bullet \\
\begin{bmatrix} \left\langle \frac{r^{2} - 3x^{2}}{r^{5}} \right\rangle & \left\langle -\frac{3xy}{r^{5}} \right\rangle & \left\langle -\frac{3xz}{r^{5}} \right\rangle \\
\left\langle -\frac{3xy}{r^{5}} \right\rangle & \left\langle \frac{r^{2} - 3y^{2}}{r^{5}} \right\rangle & \left\langle -\frac{3yz}{r^{5}} \right\rangle \\
\left\langle -\frac{3xz}{r^{5}} \right\rangle & \left\langle -\frac{3yz}{r^{5}} \right\rangle & \left\langle \frac{r^{2} - 3z^{2}}{r^{5}} \right\rangle \end{bmatrix} \bullet \begin{bmatrix} \hat{\boldsymbol{I}}_{x} \\ \hat{\boldsymbol{I}}_{y} \\ \hat{\boldsymbol{I}}_{z} \end{bmatrix} (87)$$

which is abbreviated as

$$\hat{\boldsymbol{H}}_{\text{dipolar}} = \hat{\mathbf{S}}^{\mathsf{T}} \bullet \mathbf{T} \bullet \hat{\mathbf{I}} \tag{88}$$

where T is the dipolar interaction tensor (in units of Hz) that gauges the anisotropic nuclear hyperfine interaction.<sup>5</sup> Incorporating the isotropic hyperfine term into Equation (88) gives the complete hamiltonian for the hyperfine interaction as

$$\hat{\boldsymbol{H}}_{\text{invertine}} = \hat{\mathbf{S}}^{\mathsf{T}} \bullet \mathbf{A} \bullet \hat{\mathbf{I}}$$
 (89)

where A, the hyperfine parameter (3x3) matrix, is defined as

$$\mathbf{A} = \mathbf{A}\mathbf{1}_3 + \mathbf{T} \tag{90}$$

where A is the isotropic hyperfine coupling constant and 1<sub>3</sub> is the 3x3 unit matrix.<sup>3</sup>

Orientation Of the Lab Axes With Respect To the Hyperfine Axes

In an anisotropic system, there are designated hyperfine axes that are separate from the laboratory axes. Figure 2.9 illustrates the axis system in terms of the hyperfine, and Figure 2.10 illustrates the laboratory axis system in terms of the lab field **B**. In order to establish a common axis system, one set of axes must be rotated with respect to the other. One way to do this is to hold the hyperfine axes fixed and rotate the laboratory field about the hyperfine axes.

The complete spin hamiltonian is given by

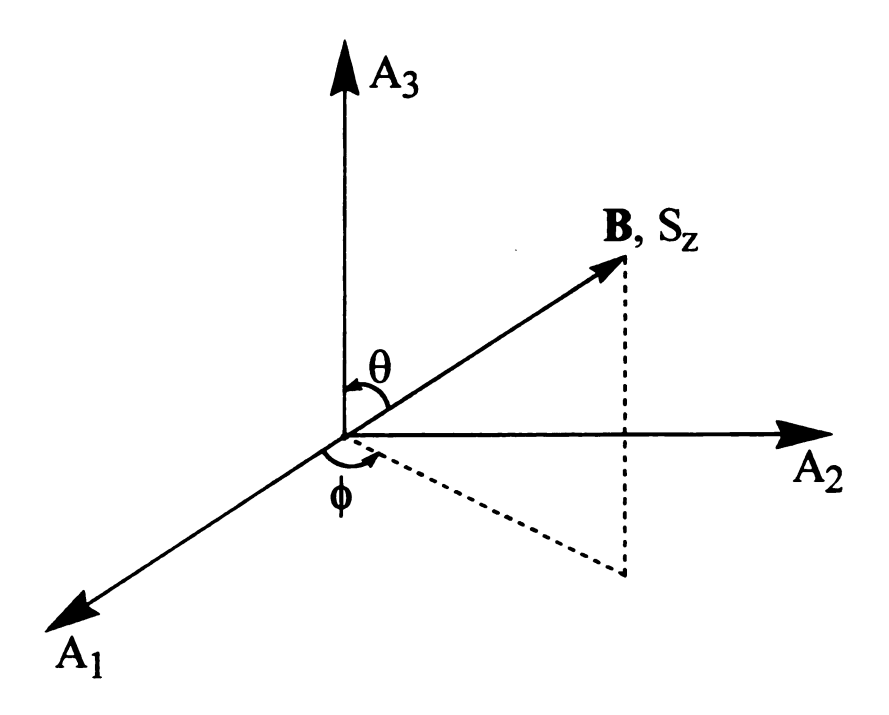


Figure 2.9: The axis system in terms of the hyperfine. **B** is the applied magnetic field and **Ş** is the electron spin in the direction of the applied field.

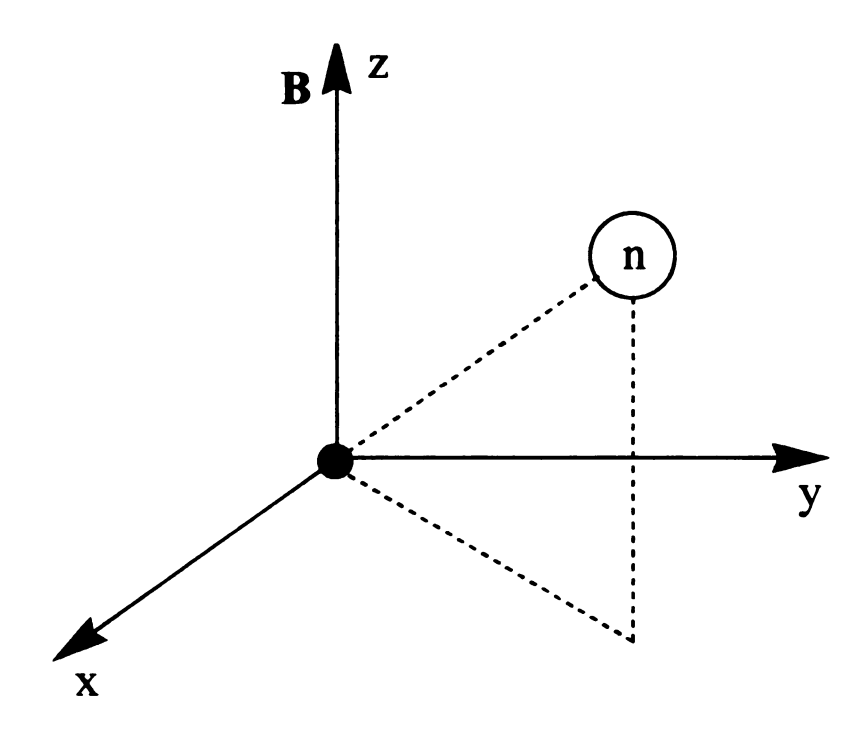


Figure 2.10: The axis system in terms of the laboratory field **B**. The electron is at the origin interacting with the nearby nucleus.

 $\hat{H} = \beta \mathbf{B} \cdot \mathbf{g} \cdot \hat{\mathbf{S}} + \hat{\mathbf{S}} \cdot \mathbf{A} \cdot \hat{\mathbf{I}} - \beta_n g_n \mathbf{B} \cdot \hat{\mathbf{I}}$  (91) where g is assumed to be isotropic, the applied field  $\mathbf{B} = \mathbf{B}_o(l_x, l_y, l_z)$ , and the operator for the electron spin, which is directed along the field, is  $\mathbf{S} = \mathbf{S}_z(l_x, l_y, l_z)$ . The coordinates  $l_x$ ,  $l_y$ , and  $l_z$  describe the laboratory field orientation in terms of  $\mathbf{B}_o$ , and are defined as

$$l_x = \sin\theta \cos\phi \tag{92}$$

$$l_{v} = \sin\theta \sin\phi \tag{93}$$

and

$$l_z = \cos\theta. \tag{94}$$

Writing out the matrices in the hamiltonian, Equation (91) becomes

$$\hat{\boldsymbol{H}} = \mathbf{g}\boldsymbol{\beta}\mathbf{B}_{\mathbf{s}}\hat{\mathbf{S}}_{z} + \hat{\mathbf{S}}_{z}(\mathbf{l}_{x}, \mathbf{l}_{y}, \mathbf{l}_{z}) \begin{pmatrix} \mathbf{A}_{xx} & 0 & 0 \\ 0 & \mathbf{A}_{yy} & 0 \\ 0 & 0 & \mathbf{A}_{zz} \end{pmatrix} (\hat{\mathbf{I}}_{x}) - \boldsymbol{\beta}_{n}\mathbf{g}_{n}\mathbf{B}_{\mathbf{s}}(\mathbf{l}_{x}\hat{\mathbf{I}}_{x} + \mathbf{l}_{y}\hat{\mathbf{I}}_{y} + \mathbf{l}_{z}\hat{\mathbf{I}}_{z}).$$
(95)

Substituting  $m_e \hbar$  for the operator of  $S_z$ , performing the matrix operations, and regrouping terms yields

$$\hat{H} = g\beta B_{o}m_{s}\hbar + (m_{s}\hbar A_{xx} - g_{n}\beta_{n}B_{o})l_{x}\hat{l}_{x} + (m_{s}\hbar A_{yy} - g_{n}\beta_{n}B_{o})l_{y}\hat{l}_{y} + (m_{s}\hbar A_{zz} - g_{n}\beta_{n}B_{o})l_{z}\hat{l}_{z}.$$
(96)

If Equation (96) is divided by h, then using Equation (77) it can be written as

 $\hat{H} = g\beta B_0 m_s + (m_s A_{xx} - \nu_n) I_x \hat{I}_x + (m_s A_{yy} - \nu_n) I_y \hat{I}_y + (m_s A_{zz} - \nu_n) I_z \hat{I}_z$  (97) where the factor of  $(2\pi)^{-1}$  in the electron Zeeman and the hyperfine terms is incorporated into the constants. For the case of  $S = \frac{1}{2}$  and  $I = \frac{1}{2}$ , a (4x4) matrix can be constructed with the z-components along the diagonal. In order to solve for the operators of  $I_x$  and  $I_y$ , the equations

$$\hat{\mathbf{I}}_{\perp} = \hat{\mathbf{I}}_{\perp} + i\hat{\mathbf{I}}_{\perp} \tag{98}$$

and

$$\hat{\mathbf{I}}_{\mathbf{x}} = \hat{\mathbf{I}}_{\mathbf{x}} - i\hat{\mathbf{I}}_{\mathbf{y}} \tag{99}$$

are used to find that

$$\hat{\mathbf{I}}_{x} = \frac{1}{2}(\hat{\mathbf{I}}_{+} + \hat{\mathbf{I}}_{-}) \tag{100}$$

and

$$\hat{\mathbf{I}}_{y} = -\frac{i}{2}(\hat{\mathbf{I}}_{+} - \hat{\mathbf{I}}_{-}). \tag{101}$$

Using the following two equations,

$$\hat{\mathbf{I}}_{+}|\mathbf{m}_{s} \quad \mathbf{m}_{I}\rangle = \left[\mathbf{I}(\mathbf{I}+1) - \mathbf{m}_{I}(\mathbf{m}_{I}+1)\right]^{\frac{1}{2}}|\mathbf{m}_{s} \quad \mathbf{m}_{I}+1\rangle$$
 (102)

and

$$\hat{\mathbf{I}}_{2}|\mathbf{m}, \mathbf{m}_{1}\rangle = \left[\mathbf{I}(\mathbf{I}+1) - \mathbf{m}_{1}(\mathbf{m}_{1}-1)\right]^{\frac{1}{2}}|\mathbf{m}, \mathbf{m}_{1}-1\rangle$$
 (103)

the x and y components of the matrix can be calculated. Using only the top block

diagonal of the full (4x4) matrix, the hamiltonian can be rewritten as

$$\hat{H} = g\beta B.m.(1) +$$

$$\begin{bmatrix} \frac{g\beta B_{\circ}}{2} + (\frac{A_{zz}}{2} - v_{n})\frac{l_{z}}{2} & \frac{g\beta B_{\circ}}{2} + (\frac{A_{xx}}{2} - v_{n})\frac{l_{x}}{2} - (\frac{A_{yy}}{2} - v_{n})\frac{il_{y}}{2} \\ \frac{g\beta B_{\circ}}{2} + (\frac{A_{xx}}{2} - v_{n})\frac{l_{x}}{2} + (\frac{A_{yy}}{2} - v_{n})\frac{il_{y}}{2} & \frac{g\beta B_{\circ}}{2} - (\frac{A_{zz}}{2} - v_{n})\frac{l_{z}}{2} \end{bmatrix} (104)$$

where (1) is the unit matrix indicating that the electron Zeeman energy is a diagonal term.

By letting  $A_x = \frac{1}{2}(A_{xx}m_s - \nu_n)$ ,  $A_y = \frac{1}{2}(A_{yy}m_s - \nu_n)$ , and  $A_z = \frac{1}{2}(A_{zz}m_s - \nu_n)$ , the (2x2) matrix in Equation (104) can be simplified to represent the nuclear part. The resulting matrix is

$$\frac{1}{2} \begin{bmatrix} A_z l_z & A_x l_x - i A_y l_y \\ A_x l_x + i A_y l_y & -A_z l_z \end{bmatrix}$$

In order to put the nuclear part of the hamiltonian in the same axis system as the electronic part, the above matrix is diagonalized. For the case of a point dipole-point dipole model, as illustrated in Figure 2.6, with an axial A tensor so that  $A_{xx} = A_{yy} = A_{yy}$  and  $A_{zz} = A_{yy}$ .

$$\lambda(m_s) = \pm \frac{1}{2} \sqrt{(A_1 m_s - v_n)^2 \sin^2 \theta + (A_1 m_s - v_n)^2 \cos^2 \theta}.$$
 (105)

From Equation (105), it can be noted that the rotation of the laboratory axes about the hyperfine axes is independent of the angle  $\phi$ . This result is useful for measuring hyperfine splittings by using the following similar equation:

$$v(m_*, \theta) = \lambda^+(m_*) - \lambda^-(m_*) = \sqrt{(A_+ m_* - v_n)^2 \sin^2 \theta + (A_* m_* - v_n)^2 \cos^2 \theta}.$$
 (106)

### Data Of Enzyme With Substrate and Product

Ruma Banerjee and Rugmini Padmakumar wanted to "test" the radical pathway mechanism by proving, and possibly identifying, the involvement of radicals in the rearrangement reaction catalyzed by mmCoA mutase. They took recombinant mmCoA mutase from *propionibacterium shermanii* and purified it 20-fold to near homogeneity in a highly active form.<sup>6</sup> Then they tested various samples using electron paramagnetic spectroscopy of the enzyme to see if they would get EPR signals or not. What they found was that for the apoenzyme, the form of the isolated enzyme, and for the holoenzyme, which is the enzyme reconstituted with the B<sub>12</sub> cofactor, no EPR signal was detected. However, when either the substrate, *L*-mmCoA, or the product, succinyl-CoA, was added to the holoenzyme and rapidly frozen in liquid nitrogen, an EPR signal was detected.<sup>6</sup>

The EPR signal detected for the sample of the mmCoA mutase with the substrate, L-mmCoA, is shown in Figure 2.11<sup>6</sup>. In the high field region, the spectrum shows

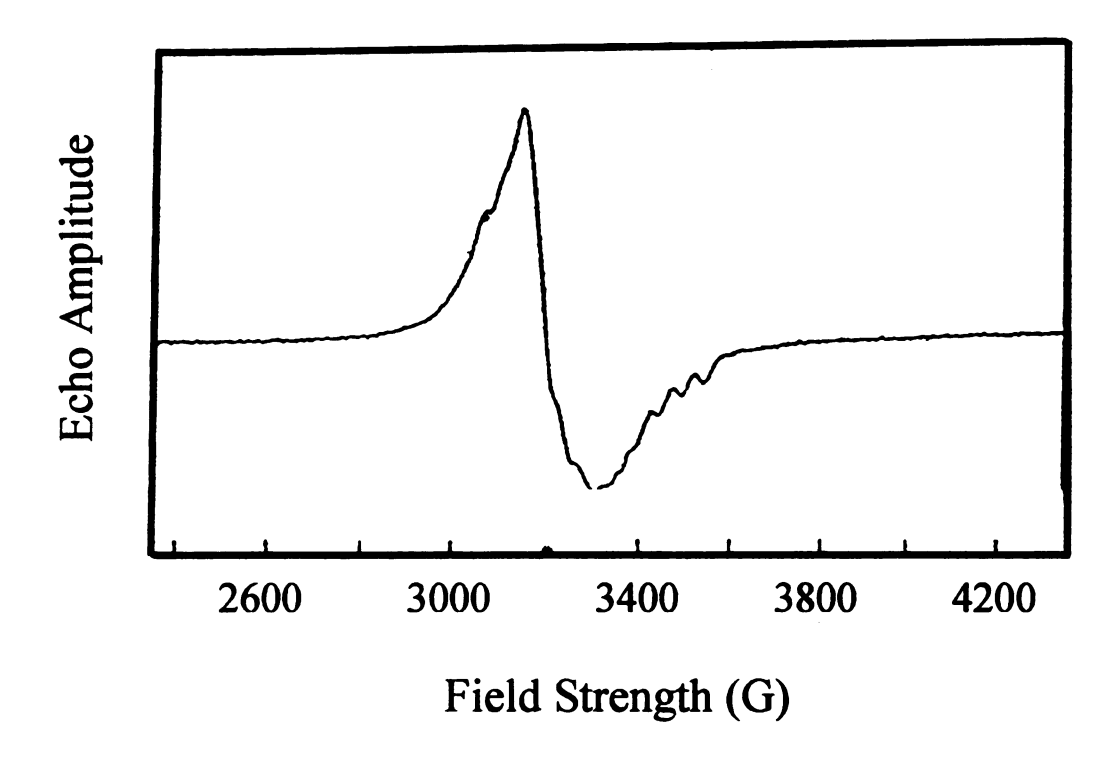


Figure 2.11: The EPR spectrum of mmCoA mutase with the substrate L-mmCoA.

hyperfine splittings resulting from coupling of the unpaired electron with the cobalt nucleus, which has a nuclear spin of I = 7/2. The  $g_{\perp}$  and  $g_{\parallel}$  values are typical for that of the cobalamin radical, where  $g_{\perp} = 2.26$ , and  $g_{\parallel} = 2.00$ . Therefore, it is certain that there is cobalamin in the sample. No other features are resolved due to inhomogeneous broadening of the lineshape, which is a distribution of resonance frequencies over an unresolved band caused by many resonance frequencies very close together.<sup>3</sup>

In the attempt to reduce the inhomogeneous broadening of the lineshape, Banerjee and Padmakumar substituted the hydrogen atoms of the methyl group on the *L*-mmCoA with deuterium atoms. Hydrogen has a nuclear g value of 5.586, while the nuclear g value for deuterium is only 0.857. The hyperfine coupling constant A, which is a measure of the magnetic interaction energy between the electron and nucleus, is proportional to the nuclear g value.<sup>3</sup> Therefore, a smaller nuclear g value will be associated with smaller hyperfine couplings. By this reasoning, a reduction in the inhomogeneous linewidth should be detected for the deuterated sample if the substrate is coupled to the unpaired electron. Figure 2.12<sup>6</sup> shows the spectrum of the holoenzyme with deuterated substrate. This spectrum is very similar to the spectrum of the holoenzyme with protonated substrate shown in Figure 2.11<sup>6</sup>, the only difference being that there is an increase in the signal-to-noise in the spectrum with deuterated substrate.

Banerjee and Padmakumar also tested a sample of the holoenzyme with the product, succinyl-CoA.<sup>6</sup> The EPR spectrum for this sample is shown in Figure 2.13<sup>6</sup>. The spectrum shows features that are identical to those observed in the spectra of the holoenzyme with both protonated and deuterated substrate, namely the coupling of the unpaired electron to the cobalt nucleus in the high field region, and inhomogeneous

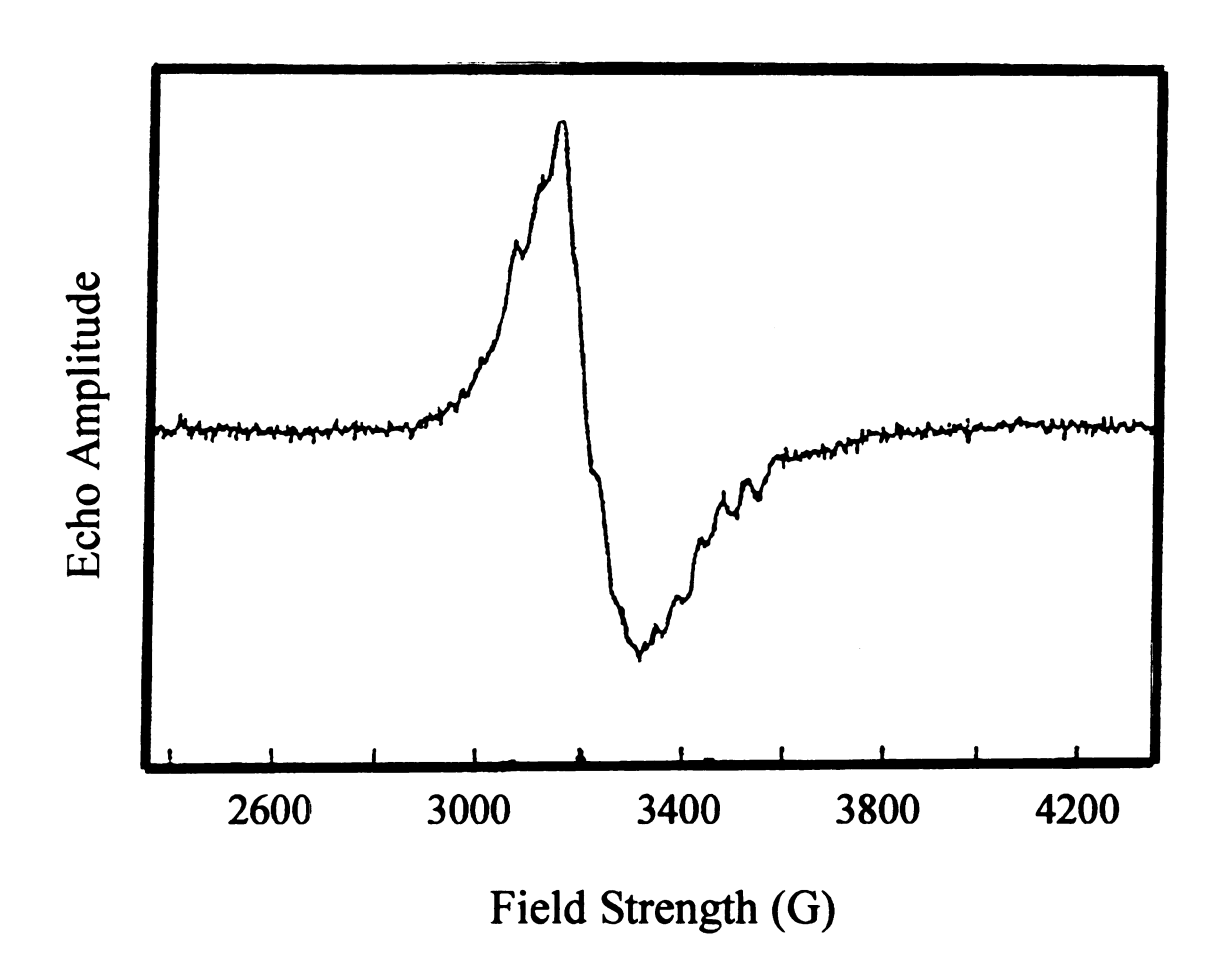


Figure 2.12: The EPR spectrum of mmCoA mutase with [CD<sub>3</sub>]mmCoA.

47

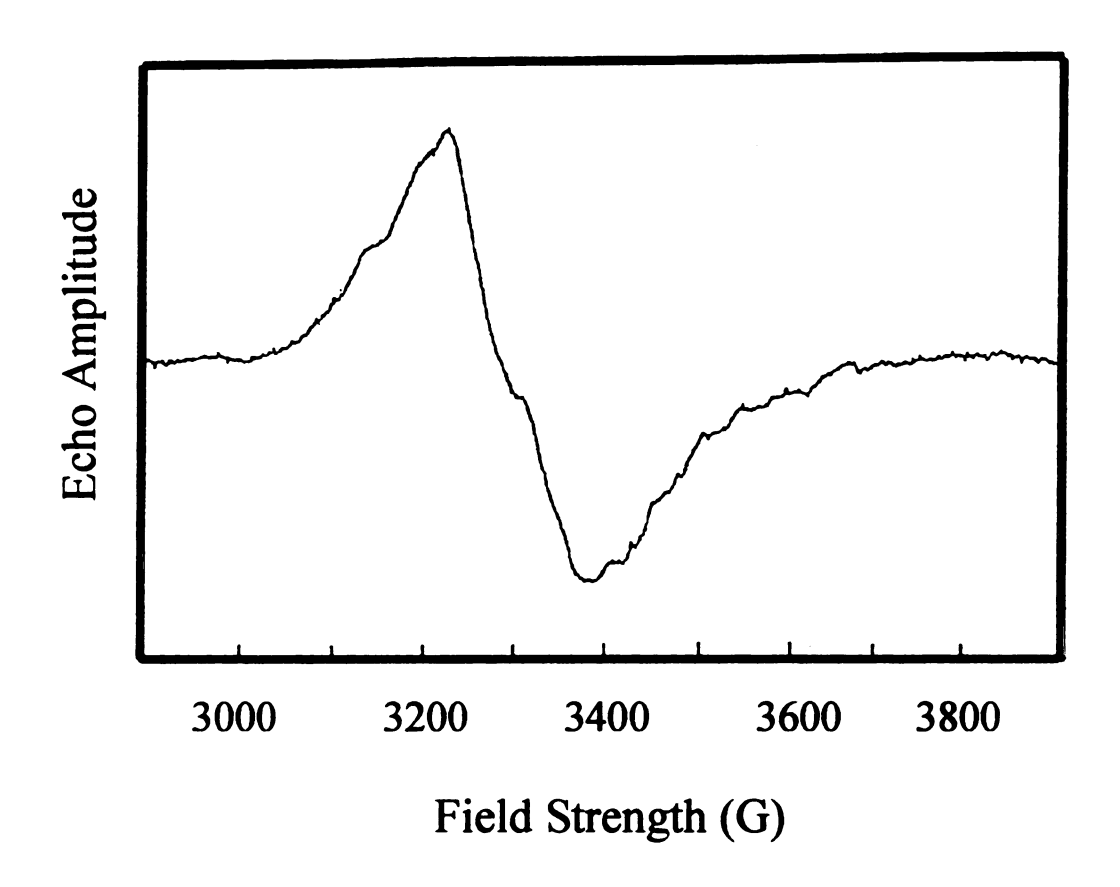


Figure 2.13: The EPR spectrum of mmCoA mutase with the product succinyl-CoA.

broadening of the lineshape.

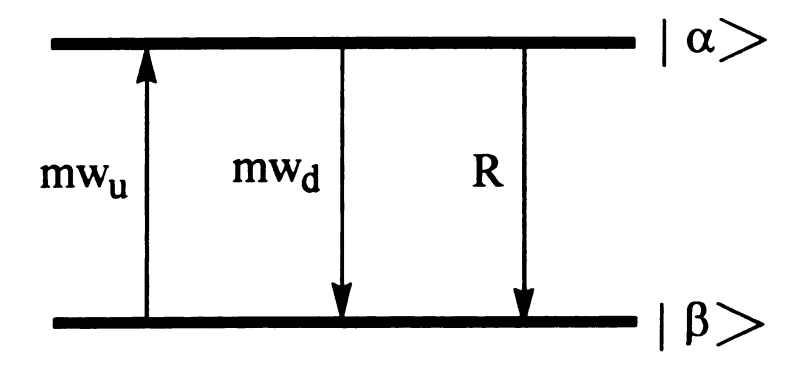
### Principles Of Transition Rates and Power Saturation

For a two level system with a ground state  $\beta$  and an excited state  $\alpha$ , illustrated in Figure 2.14, there are two different phenomenon going on. There are the microwave-induced transitions up and down, and there is also a relaxation rate down. The microwave-induced rates up and down are always equal, but when the relaxation rate down is added to the microwave-induced rate down at low power, the downward transitions become greater than the one upward transition. Physically then, the excited state is being depopulated faster than it can be populated. A technique is needed to suppress the relaxation rate down in order to restore the equilibrium of the upward and downward transition rates. This can be done by increasing the microwave power. Therefore, at high power, the upward and downward transition rates are restored to equilibrium, and theoretically then, the populations of both the ground state and the excited state are equal. This condition is known as power saturation.<sup>3</sup> This concept can be useful for distinguishing multiple species in EPR, if the different species have unique saturation properties.

For a macroscopic sample in which a resonance is observed, a two level system for an electron with  $S = \frac{1}{2}$  is represented in Figure 2.15<sup>7</sup>. The number of spins in the lower and upper states is represented by N. and N<sub>+</sub> respectively, and the total number of spins is given by

$$N_{Tot} = N_+ + N_-$$
 (107)

When a magnetic field is applied to the system, the number of spins in each level changes due to induced transitions, but the total number of spins N<sub>Tot</sub> remains unchanged. The



## (a) At low power:

$$mw_u = mw_d$$
$$mw_u < mw_d + R$$

# (b) At high power:

$$mw_u \approx mw_d + \mathcal{K}$$
 $\Longrightarrow$  Saturation

Figure 2.14: For a two level system, with ground state  $\beta$  and excited state  $\alpha$ , the microwave-induced upward transition rate  $mw_u$  equals the microwave-induced downward transition rate  $mw_d$  at low power.

- (a) When the relaxation rate down is added to the microwave-induced rate down, they become greater than the upward transition rate.
- (b) The microwave power can be increased to overcome the relaxation rate down, leading to a condition called power saturation.

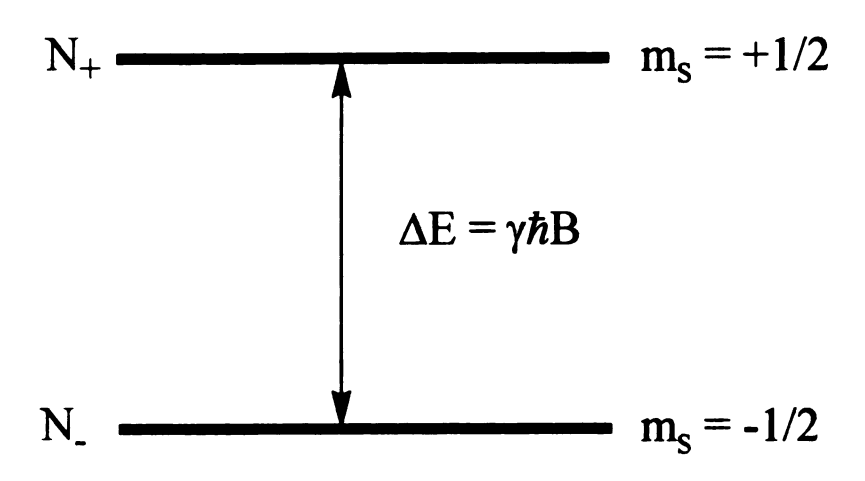


Figure 2.15: The two level system of an electron with S = 1/2. The transition energy  $\Delta E = \gamma \hbar B$ . The number of spins in the two states are represented by N<sub>+</sub> and N<sub>-</sub>.

probability per second of inducing a transition of a spin from the lower state to the upper state can be represented by W., while the reverse transition can be represented by W., the change of population in terms of N. can be written as the following differential equation:

$$\frac{dN_{\perp}}{dt} = N_{\perp} W_{+ \rightarrow} - N_{\perp} W_{- \rightarrow} . \tag{108}$$

From time-dependent perturbation theory, the formula for the probability per second  $(P_{a\rightarrow b})$  that an interaction V(t) induces a transition from a state (a) with energy  $E_a$  to a state (b) with energy  $E_b$  is

$$P_{a\to b} = \frac{2\pi}{\hbar} \left| \left( b | V | a \right) \right|^2 \, \delta \left( E_a - E_b - \hbar \omega \right). \tag{109}$$
 Since  $| (a | V | b) |^2 = | (b | V | a) |^2$ , it follows that  $(P_{a\to b}) = (P_{b\to a})$ . Therefore,  $W_{\to +} = W_{\to +} = W$ , meaning that the probability per second of inducing a transition of a spin from the lower state to the upper state is the same as that of the upper state to the lower state. Thus, Equation (108) can be rewritten as

$$\frac{dN_{\perp}}{dt} = W(N_{\perp} - N_{\perp}) \tag{110}$$

By letting

$$n = N_{-} - N_{+} \tag{111}$$

then from addition and subtraction of Equations (107) and (111) the populations of each of the two levels can be written as

$$N_{\cdot} = \frac{1}{2} (N + n)$$
 (112)

and

$$N_{+} = \frac{1}{2}(N - n).$$
 (113)

Substituting Equations (112) and (113) into Equation (110) simplifies the equation to

$$\frac{dn}{dt} = -2Wn. \tag{114}$$

The solution to Equation (114) is

$$n = n(0)e^{-2Wt} \tag{115}$$

where n(0) is the value of n at t = 0. This solution suggests that if there is an initial population difference it will disappear with time due to the induced transitions.<sup>7</sup>

The rate of absorption of energy, dE/dt, is obtained by finding the number of spins per second that go from the lower energy level to the higher energy level, minus the number that drop back down emitting energy. Thus

$$\frac{dE}{dt} = N_{\perp}W\hbar\omega - N_{\perp}W\hbar\omega = \hbar\omega Wn \qquad (116)$$

where  $\omega$  is the frequency of the transition. From Equation (116), it can be seen that in order for a net absorption of energy, there must be a population difference between the two energy levels.<sup>7</sup>

If a magnetic field is applied to an unmagnetized sample, then in order for the system to be in its most stable configuration, the electron magnetic moments prefer to be aligned antiparallel to the applied magnetic field. This would require that N. be greater than  $N_+$ , which corresponds to a net number of transitions from the upper to the lower energy state. As this occurs, the spins give up energy, implying that there is a heat transfer to some other system that is accepting the energy being released. This heat transfer will continue until the relative populations  $N_+/N_-$  correspond to the temperature T of the reservoir which is receiving the energy. The final equilibrium populations  $N_-$ ° and  $N_+$ ° are given by

$$\frac{N_{+}^{\circ}}{N^{\circ}} = e^{\frac{\Delta E}{kT}} = e^{\frac{AB}{kT}}.$$
 (117)

It can be said then that there exists a mechanism for inducing transitions between  $N_-$  and  $N_+$  which is due to the coupling of the spins to some other system, namely the reservoir. If the probability per second that this coupling induces a spin transition from the lower to the upper energy level is represented by  $W\uparrow$ , and the reverse transition is represented by  $W\downarrow$ , then the rate equation can be written as

$$\frac{dN_{\perp}}{dt} = + N_{\perp} W \downarrow - N_{\perp} W \uparrow . \tag{118}$$

It is important to note here that the upward and downward transition probabilities are no longer equal. As stated earlier, when magnetizing an unmagnetized sample, a net downward transition is expected. However, since in the steady-state dN/dt is zero, then from Equation (118) it is found that

$$\frac{N_{\perp}^{\circ}}{N_{\parallel}} = \frac{W \uparrow}{W \downarrow}. \tag{119}$$

Using the relationships given in Equations (117) and (119), the ratio of W↑ to W↓ is given by

$$\frac{\mathbf{W}\uparrow}{\mathbf{W}\downarrow} = \mathbf{e}^{\frac{\mathbf{M}B}{\mathbf{k}T}} \tag{120}$$

which illustrates that in this case the transition probabilities are not equal.<sup>7</sup>

In order to understand the reason why the transition probabilities are unequal for this case, it is important to realize that the reservoir imposes limitations to the transition probabilities. Not only does the thermal transition require that the spins couple to some other system, but this system must also be in an energy state that will allow a transition. Suppose that the reservoir has two energy levels that are separated by a distance equal to the two levels of the electron system, illustrated in Figure 2.16<sup>7</sup>. Figure 2.16(a)<sup>7</sup>

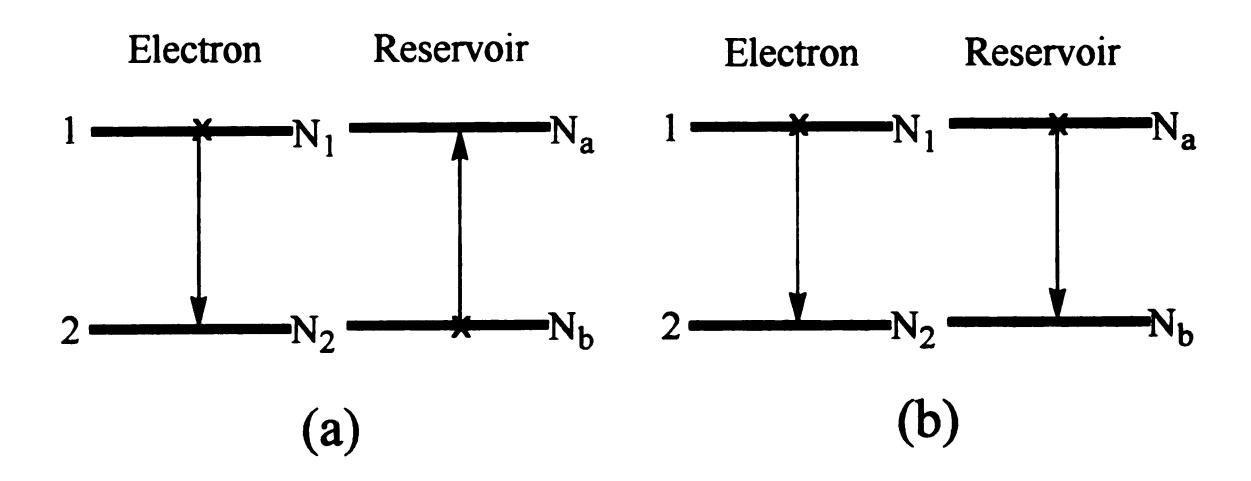


Figure 2.16: The two level systems of both the electron system, labelled 1 and 2, and the reservoir, labelled a and b. The diagram in (a) represents an allowed transition, while the diagram in (b) represents a forbidden transition. The x's represent initial states. The populations of the two levels in the electron system are given by  $N_1$  and  $N_2$ , and the populations of the two levels in the reservoir system are given by  $N_a$  and  $N_b$ .

represents an allowed transition, where the initial state of the electron system is at the upper level and the initial state of the reservoir is at the lower level. Therefore, as the downward transition of the electron releases energy to the reservoir (or lattice), the reservoir can simultaneously absorb the energy to allow an upward transition, which satisfies conservation of energy. However, if both the electron system and reservoir have their initial states in the upper level, shown in Figure 2.16(b)<sup>7</sup>, a simultaneous transition is forbidden because energy is not conserved. In other words, both systems will be simultaneously releasing energy. Thus, this argument illustrates that for the case where the spins couple to some other system (called the reservoir), the rate of transition of the electron is dependent on the probability that the reservoir will be in a state that will allow the transition to occur. Due to this constraint, the transition probabilities W...+ and W+... are not equal.<sup>7</sup>

According to Figure  $2.16^7$ , the electron states have populations  $N_1$  and  $N_2$ , and the lattice states have populations  $N_a$  and  $N_b$ . Thus, the number of transitions per second is found as

$$\#/S = N_1 N_b W_{1b \to 2a} \tag{121}$$

where  $W_{1b\to 2a}$  is the probability per second of the transition where the electron is initially in state 1 and the lattice is initially in state b. By equating the rate of the transition shown in Figure 2.16(a)<sup>7</sup> to its reverse transition, the steady-state condition is represented as

$$N_1 N_b W_{1b \to 2a} = N_2 N_a W_{2a \to 1b}. \tag{122}$$

According to the quantum theory,  $W_{1b\to 2a} = W_{2a\to 1b}$ , so that in thermal equilibrium, Equation (122) becomes

$$\frac{N_1}{N_2} = \frac{N_a}{N_b} \tag{123}$$

That implies that at thermal equilibrium, the electron levels will have the same relative populations as those of the lattice (the two populations will be in thermal equilibrium). It is also possible now to solve for W<sup>↑</sup> and W<sup>↓</sup> (the probabilities per second that coupling of the electron spins to the lattice will induce upward or downward transitions):

$$\mathbf{W}\uparrow = \mathbf{N_a}\mathbf{W_{2a\to 1b}} \tag{124}$$

and

$$\mathbf{W} \downarrow = \mathbf{N_b} \mathbf{W_{1b \to 2a}} = \mathbf{N_b} \mathbf{W_{2a \to 1b}} \tag{125}$$

where it can be seen that W↑ and W↓ are unequal.<sup>7</sup>

Referring back to Equation (118), N. and  $N_{+}$  can be substituted by Equations (112) and (113) to give

$$\frac{dn}{dt} = N(W \downarrow -W \uparrow) - n(W \downarrow +W \uparrow)$$
 (126)

Equation (126) can be rewritten as

$$\frac{dn}{dt} = \frac{n_{\circ} - n}{T_{\circ}} \tag{127}$$

where

$$n_{\circ} = N \left( \frac{W \downarrow -W \uparrow}{W \downarrow +W \uparrow} \right) \tag{128}$$

and

$$\frac{1}{T_{i}} = N(W \downarrow + W \uparrow) \tag{129}$$

The solution of the differential equation given in Equation (127) is

$$n = n_{\circ} + Ae^{-\frac{t}{T_1}} \tag{130}$$

where A is a constant of integration. In the above equations,  $n_0$  represents the thermal equilibrium population difference, and  $T_1$  is the characteristic time associated with the approach to thermal equilibrium, called the "spin-lattice relaxation time". In other words,  $T_1$  characterizes the time needed to magnetize an unmagnetized sample (where the spins try to achieve the more stable configuration of aligning with the field). For instance, if a sample is initially unmagnetized, the magnetization process is described by the following exponential rise to equilibrium:

$$n = n_{\circ} + (1 - e^{-\frac{t}{T_1}})$$
which physically describes a relaxation process. (131)

If the two rate equations for dn/dt given in Equations (114) and (127) are combined, the complete rate equation becomes

$$\frac{\mathrm{dn}}{\mathrm{dt}} = -2\mathrm{Wn} + \frac{\mathrm{n}_{\circ} - \mathrm{n}}{\mathrm{T_{1}}}.$$
 (132)

The first term in Equation (132) represents the transitions induced by the applied alternating field, while the second term represents the transitions due to thermal processes. From the steady state condition of Equation (132), it is found that

$$n = \frac{n_{\circ}}{1 + 2WT_{1}}.$$
 (133)

From Equation (133) it can be seen that if  $2WT_1 \ll 1$ , then  $n \cong n_0$ . That would imply that the absorption of energy from the alternating field would not affect the populations much from their thermal equilibrium values.<sup>7</sup>

The rate of absorption of energy dE/dt is given by

$$\frac{dE}{dt} = n\hbar\omega W = n_o\hbar\omega \frac{W}{1 + 2WT}.$$
 (134)

From Equation (134), it can be seen that the power absorbed can be increased by the electron by increasing the amplitude of the alternating field, as long as  $2WT_1 \ll 1$ . If, however, the transition rate W becomes large enough so that  $W \sim \frac{1}{2} T_1$ , then the power absorbed levels off even if W is increased. This effect is known as "power saturation". In general, systems with long  $T_1$  values saturate faster than those with short  $T_1$  values.

## Power and Temperature Dependence Study

Banerjee and Pamakumar performed a microwave power dependence study on the sample of the mmCoA mutase with L-mmCoA at both 10K, shown in Figure 2.17<sup>6</sup>, and at 25K, shown in Figure 2.18<sup>6</sup>, where the power ranged from 100 to 0.05 mW.<sup>6</sup> At 10K, the g value shifted from 2.14 to 2.11. At 25K, there was only one g value at 2.11. One way to interpret these spectra is by the concept of power saturation.

Looking at the power dependence spectrum at 10K in Figure 2.17<sup>6</sup>, Banerjee and Padmakumar believed that there were contributions from two different species with different relaxation properties, one being a fast relaxing species at g = 2.14, and the other being a slow relaxing species at g = 2.11. The species with fast relaxing properties would be at the higher power, 100 mW, because it would require more power to drive one-half the population to the excited energy level. The species with slow relaxing properties would therefore be at the lower power, 0.05 mW. In comparing the two spectra at 10K and 25K shown in Figures 2.17<sup>6</sup> and 2.18<sup>6</sup> respectively, it could be seen that by increasing the temperature by 15K, the fast relaxing species was lost. Thus, from their power and temperature dependence study, Banerjee and Padmakumar believed they

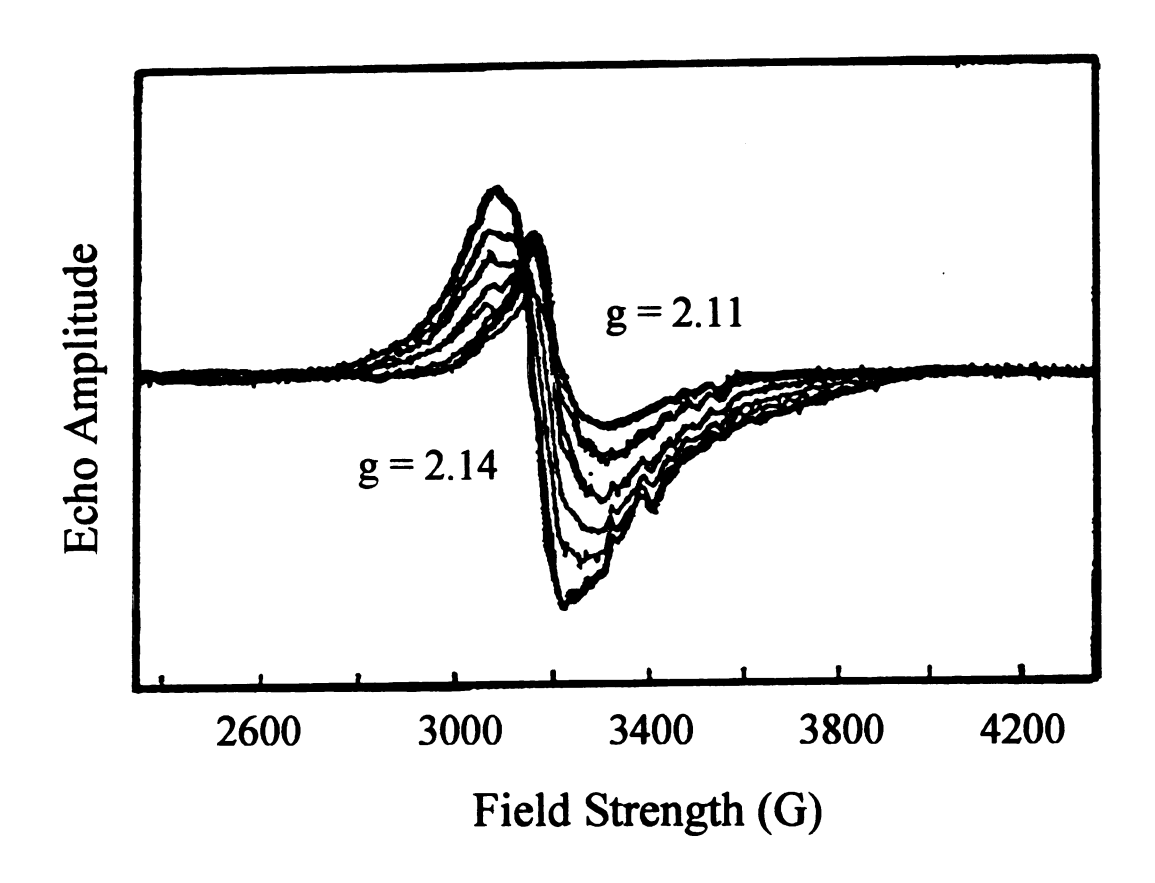


Figure 2.17: The EPR spectrum of the power dependence study of mmCoA mutase with L-mmCoA at 10 K. There is a shift in the g value as the power is varied from 100 mW to 0.05 mW. At 100 mW, the g value is 2.14. At .05 mW, the g value is 2.11.

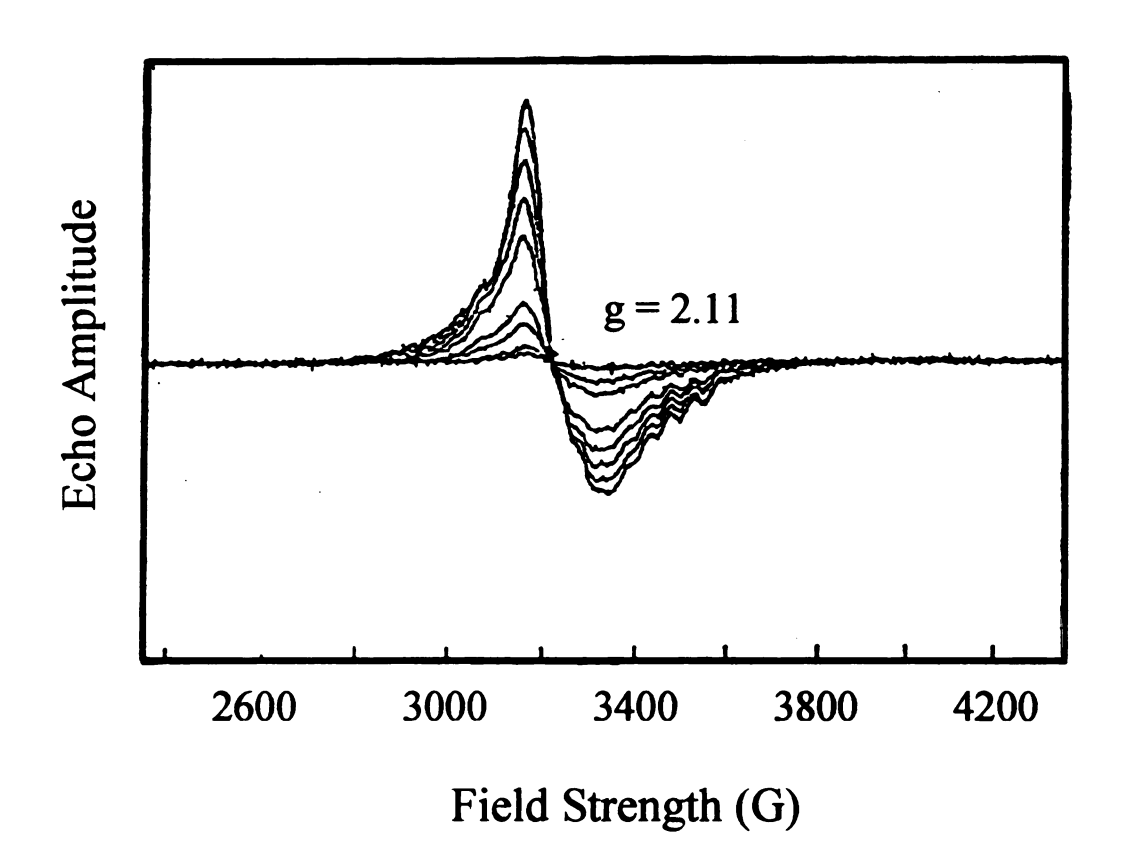


Figure 2.18: The EPR spectrum of the power dependence study of mmCoA mutase with L-mmCoA at 25 K. As the power is varied from 100 mW to 0.05 mW, there is no shift in the g value. The g value of the lineshape is 2.11.

had distinguished two radicals which had different relaxation properties. Based on their EPR studies, Banerjee and Padmakumar concluded that either there were two radical pairs in the sample, or they had detected two different states of the same radical pair.<sup>6</sup>

#### References

- 1. Tipler, Paul A. Physics. Worth Publishers: New York, 1991, pp.882-883.
- 2. Alberty, Robert A., and Robert J. Silbey. <u>Physical Chemistry</u>. John Wiley and Sons, Inc.: New York, 1992, pp. 325-331, 350-355.
- 3. Weil, J. A., J. R. Bolton, and J. E. Wertz. <u>Electron Paramagnetic Resonance</u>. John Wiley & Sons, Inc.: New York, 1994.
- 4. Atkins, Peter. Physical Chemistry. W. H. Freeman and Co.: New York, 1994, pp. 553-554.
- 5. Drago, R., <u>Physical Methods For Chemists</u>. Saunders College Publishers: Fort Worth, 1992.
- 6. Banerjee, R., and R. Padmakumar, *The Journal Of Biological Chemistry*, April 21, 1995, Vol. 270, No. 16, pp. 9295-9300.
- 7. Schlichter, C. P. <u>Principles Of Magnetic Resonance</u>. Springer-Verlag: Berlin: 1990, pp. 4-9.

# Chapter 3: Electron Spin Echo Envelope Modulation

Banerjee and Padmakumar's EPR spectra for the samples containing mmCoA mutase with *L*-mmCoA showed inhomogeneous broadening of the lineshape. 

Inhomogeneous line broadening can be caused by an inhomogeneous external magnetic field, by anisotropic interactions in randomly oriented systems, meaning a distribution of local magnetic fields, or by unresolved hyperfine structure, where many lines are very close together. Unresolved hyperfine structure occurs when the number of hyperfine components from nearby nuclei are so large that no structure is observed. What is detected then is a broad peak, or an "envelope", of a multitude of lines. 

A technique other than continuous wave EPR spectroscopy must be used to measure hyperfine couplings.

The conventional EPR spectroscopy is the continuous wave technique, where monochromatic, continuous microwave radiation is applied to the spin system. A variation of this technique is a method by which a sequence of short microwave pulses are applied to the system. This technique is a method of pulsed EPR spectroscopy known as electron spin echo envelope modulation, or ESEEM. The main advantage of this technique is that it allows for the measurement of small electron-nuclear hyperfine couplings that are often masked by inhomogeneous broadening of the EPR lineshape in continuous wave spectra. The two most common sequences of pulses that can be used are a two pulse scheme and a three pulse scheme.<sup>3</sup>

#### Two Pulse ESEEM

In a two-pulse ESEEM experiment, a  $90^{0}$  microwave pulse is applied to the sample, as shown in Figure 3.1. After a time  $\tau$ , a  $180^{0}$  microwave pulse is applied to the sample. After time  $\tau$  again, an electron spin echo results. When the time between the two pulses in the sequence,  $\tau$ , is increased, the spin echo decays exponentially. This decay is determined by the spin-spin relaxation time. By plotting the integrated intensity of these echoes as a function of the time between the two pulses  $\tau$ , the electron spin echo decay envelope can be measured. The result is an overall decay of the electron spin magnetization, which usually shows modulations caused by weak interactions with nuclei surrounding the paramagnetic centers<sup>3</sup>, as illustrated in Figure 3.2<sup>3</sup>.

It is much easier to understand the production of the spin echo from the classical point of view, which is in terms of the bulk magnetization vector  $\mathbf{M}$ . In the classical picture, shown in Figure 3.3<sup>3</sup>, initially the bulk magnetization of the sample is directed along the z-axis (Figure 3.3a<sup>3</sup>). The laboratory magnetic field,  $\mathbf{B}_0$ , is also directed along the z-axis. The magnetic field associated with the microwave pulses,  $\mathbf{B}_1$ , is along the y-axis, perpendicular to the lab field. The first 90° microwave pulse, applied along the y-axis, rotates the bulk magnetization 90° until it is aligned with the x-axis. During the time  $\tau$  between the first and second pulses, each individual spin packet within the bulk magnetization vector begins to precess at different angular frequencies because each spin packet experiences different local magnetic environments. The 180° pulse torques each spin packet magnetization vector through a 180° angle about the y-axis. This allows refocusing of the spin packets since some of the packets are rotating with larger angular frequencies than others. After a time  $\tau$ , the individual magnetization vectors are in phase

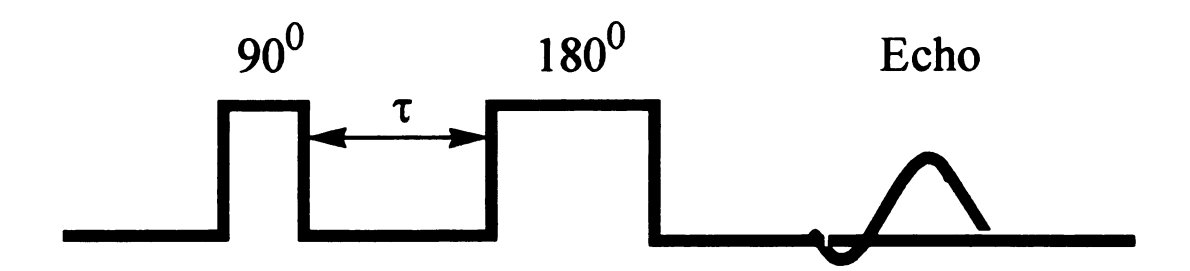


Figure 3.1: The microwave pulse sequence of a two-pulse ESEEM experiment.

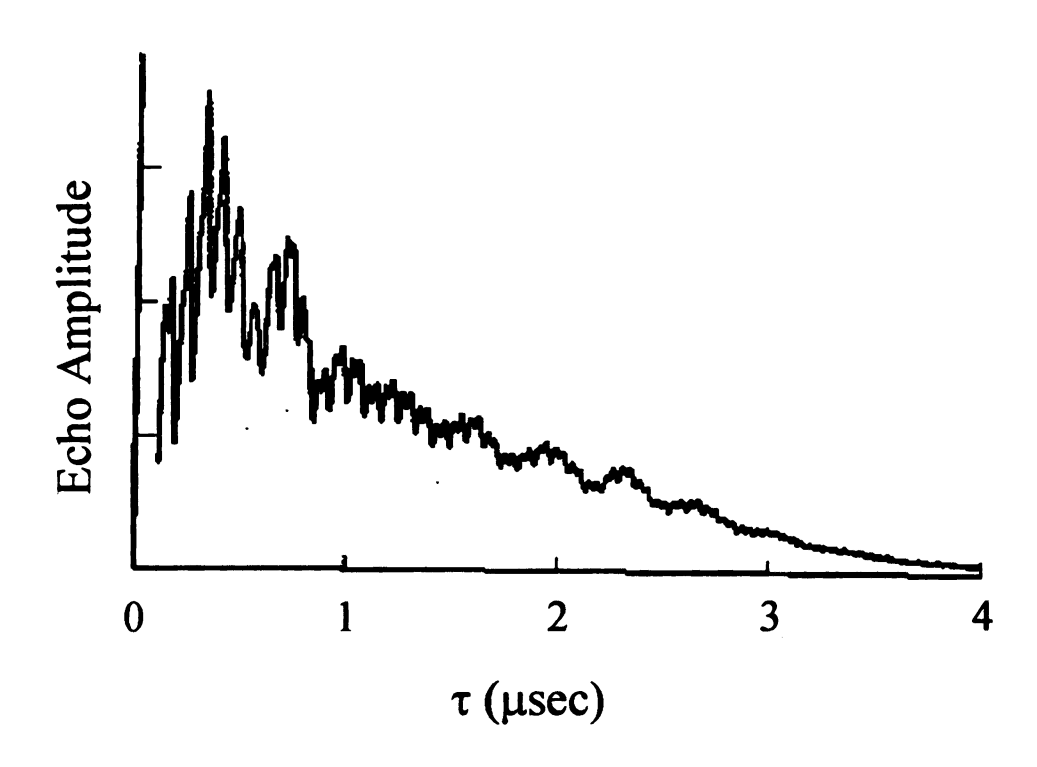
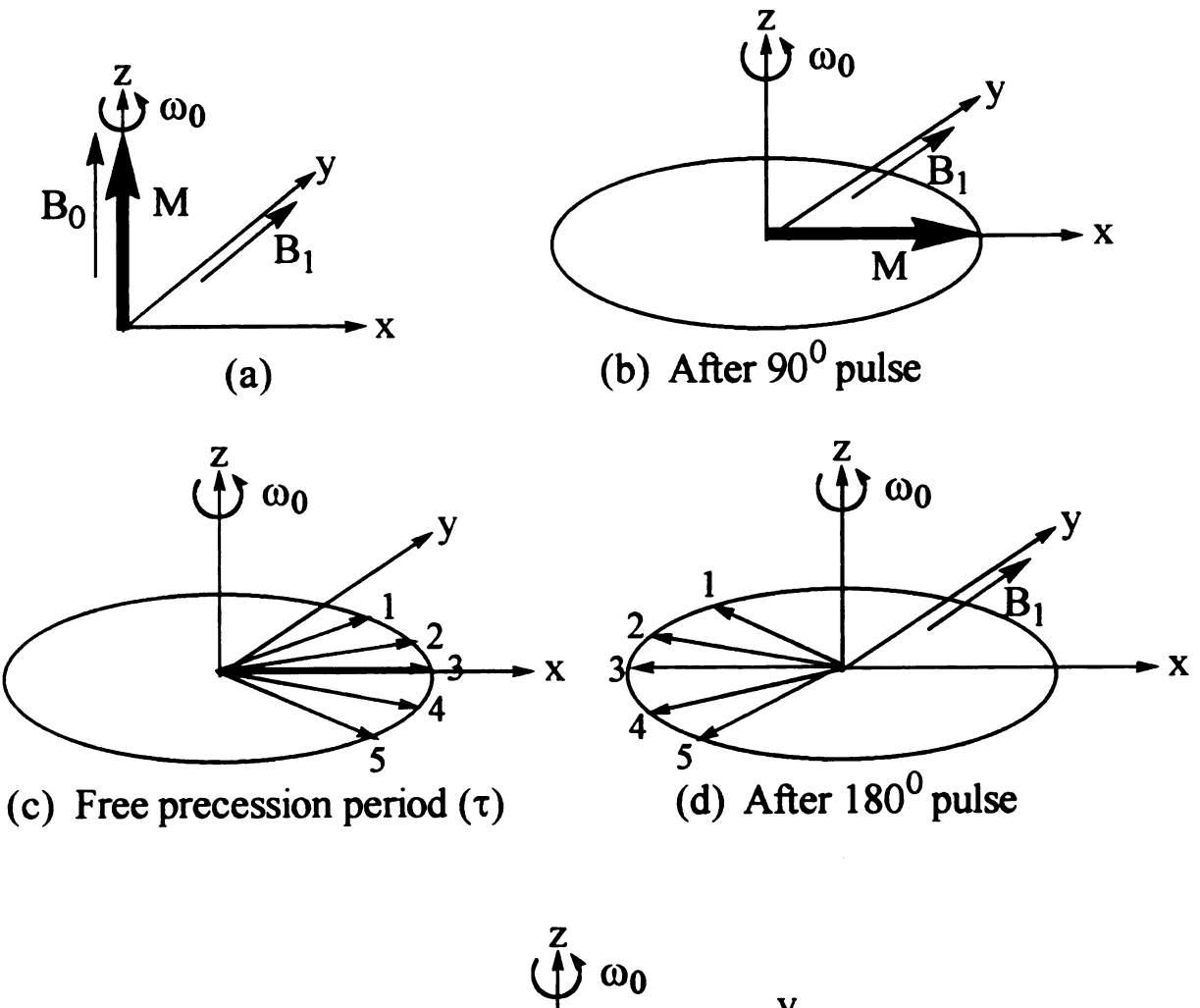
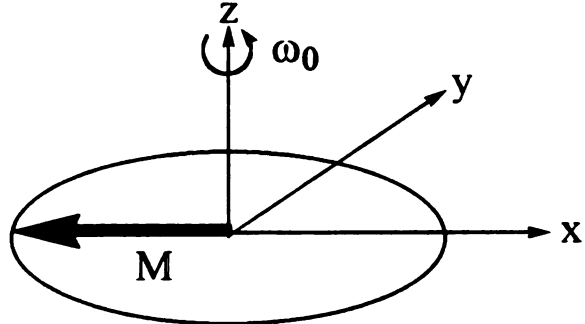


Figure 3.2: The modulated electron spin echo decay plot of Ni(III)(CN)<sub>4</sub>(H<sub>2</sub>O)<sub>2</sub> complex.





(e) Refocusing of magnetization  $(2\tau)$  to form spin echo at  $2\tau$ 

Figure 3.3: The classical picture of a two-pulse ESEEM experiment.  $B_0$  is the lab field,  $B_1$  is the magnetic field associated with the microwave pulses, M is the bulk magnetization, and  $\omega_0$  is the microwave pulse frequency.

along the x-axis, and a primary echo is observed at time 2τ after the beginning of the pulse sequence.<sup>3,4,5</sup>

Two-Pulse ESEEM For A Spin System With  $S = \frac{1}{2}$  and  $I = \frac{1}{2}$ 

For a system with one nucleus with nuclear spin  $I = \frac{1}{2}$  coupled to an electron spin  $S = \frac{1}{2}$ , the hamiltonian for the case of an isotropic electron g matrix and an axial hyperfine interaction is

$$\frac{\hat{H}}{\hbar} = \omega_s \hat{\mathbf{S}}_z + \mathbf{A}_{zz} \hat{\mathbf{S}}_z \hat{\mathbf{I}}_z + \mathbf{A}_{xz} \hat{\mathbf{S}}_z \hat{\mathbf{I}}_x - \omega_1 \hat{\mathbf{I}}_z. \tag{135}$$

For spin systems with nuclear spin I  $\geq$ 1, there would be a fifth term due to a nuclear quadrupole interaction, which is more complicated and will thus be discussed later. For this more simpler case, the first term of the hamiltonian given in Equation (135), which is the electron Zeeman term, describes the interaction of the electron spin with the external magnetic field  $\mathbf{B}_0$ . The second and third terms of Equation (135) are the electron-nuclear hyperfine interaction terms, where  $\mathbf{A}_{zz} = \mathbf{A} = \mathbf{A}_{\parallel} \cos^2\theta + \mathbf{A}_{\perp} \sin^2\theta$ , and  $\mathbf{A}_{xz} = \mathbf{B} = (\mathbf{A}_{\parallel} - \mathbf{A}_{\perp})\cos\theta\sin\theta$ . The angle  $\theta$  is the angle between the principal axis of the hyperfine tensor and the laboratory field  $\mathbf{B}_0$ .  $\mathbf{A}_{\parallel}$  and  $\mathbf{A}_{\perp}$  represent the principal values of the axially symmetric hyperfine tensor, which can be described using two different types of coupling. The first is a Fermi contact coupling, denoted  $\mathbf{A}_{iso}$ , as it is isotropic and at the nucleus, and the second is a dipole-dipole coupling,  $\mathbf{D} = \mathbf{gg}_n\beta\beta_n/r^3$ , which depends on the orientation of the nucleus with respect to the unpaired electron. Using these two coupling terms,  $\mathbf{A}_{\parallel}$  and  $\mathbf{A}_{\perp}$  can be defined as

$$A_{i} = A_{iso} + 2D \tag{136}$$

and

$$A_{I} = A_{iso} - D_{I}^{3}$$
 (137)

The fourth term in Equation (135) is the nuclear Zeeman term. The nuclear Zeeman term describes the interaction of the nuclear spin with the external magnetic field **B**<sub>0</sub>.

The hamiltonian matrix, which is constructed in an uncoupled basis set consisting of electron and nuclear spin product states  $lm_s, m_l >$ , can be diagonalized for each of the two electron spin manifolds to give the eigenvalues and eigenvectors of Equation (135). The only term in the operator that gives rise to off-diagonal elements is the  $l_x$  term. The results can be summarized using an energy level diagram, as shown in Figure 3.4<sup>3</sup>. For the EPR transitions marked lul and lvl in Figure 3.4<sup>3</sup>, the normalized probability amplitudes are

$$|u| = \frac{\langle 2|\hat{\mathbf{S}}|3\rangle}{0.5g\beta \mathbf{B}_1} = \sin\left[\frac{(\phi_\alpha - \phi_\beta)}{2}\right]$$
 (138)

and

$$|v| = \frac{\left\langle 1|\hat{\mathbf{S}}|3\right\rangle}{0.5\mathbf{g}\beta\mathbf{B}_{1}} = \cos\left[\frac{\left(\phi_{\alpha} - \phi_{\beta}\right)}{2}\right]. \tag{139}$$

The angles  $\phi_{\alpha}$  and  $\phi_{\beta}$  define the axes of quantization for the  $\alpha$  and  $\beta$  spin manifolds. They are defined as  $\sin\!\phi_{\alpha}=B/2\omega_{\alpha}$  and  $\sin\!\phi_{\beta}=B/2\omega_{\beta}.^3$ 

When combining these quantum mechanical results summarized in Figure 3.4<sup>3</sup> with the classical picture of echo formation shown in Figure 3.3<sup>3</sup>, the origin of ESEEM can be understood as the semiclassical picture shown in Figure 3.5<sup>3</sup>. In Figure 3.5<sup>3</sup>, the microwave frequency  $\omega_0$  is equal to  $\omega_s$  of Figure 3.4<sup>3</sup>. The focus is on the response of the packet of spins that makes a transition from 13> to 12> after the first 90<sup>0</sup> pulse. After the

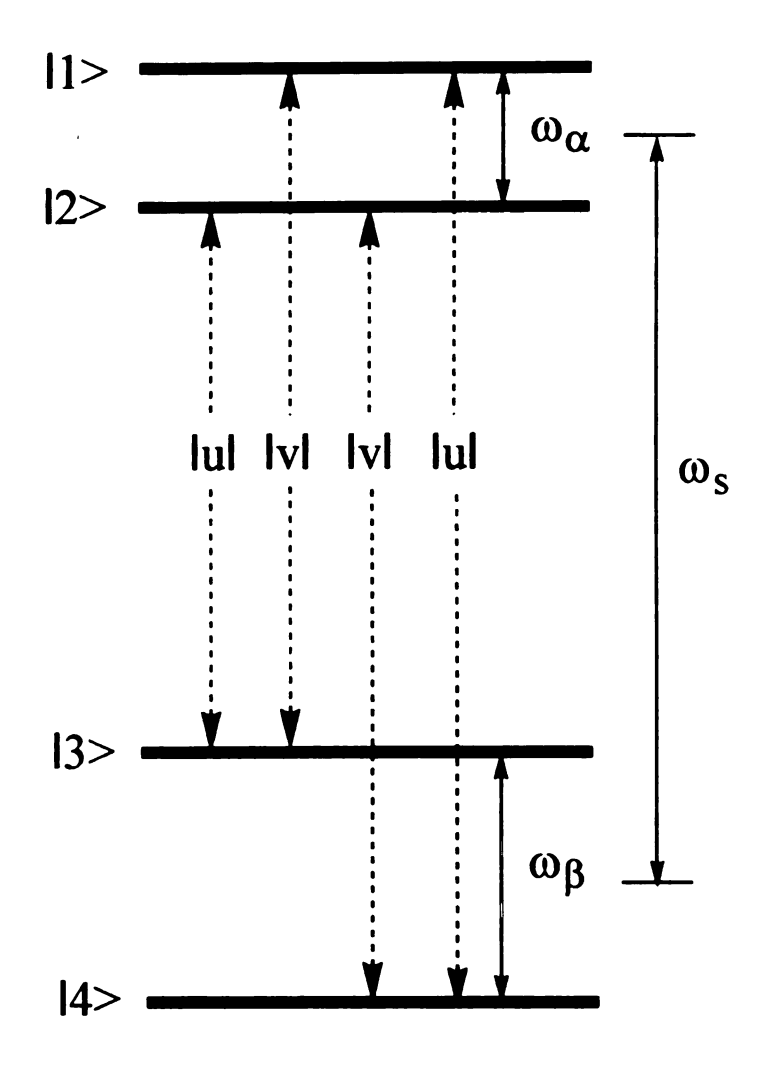


Figure 3.4: The energy level diagram describing the quantum mechanical results of an ESEEM experiment for an  $S = \frac{1}{2}$ ,  $I = \frac{1}{2}$  spin system. The frequencies  $\omega_{\alpha}$  and  $\omega_{\beta}$  are

$$\omega_{\alpha} = \sqrt{\left(\omega_{1} - \frac{A}{2}\right)^{2} + \frac{B^{2}}{4}}$$

and

$$\omega_{\beta} = \sqrt{\left(\omega_{\rm I} + \frac{\rm A}{2}\right)^2 + \frac{\rm B^2}{4}}.$$

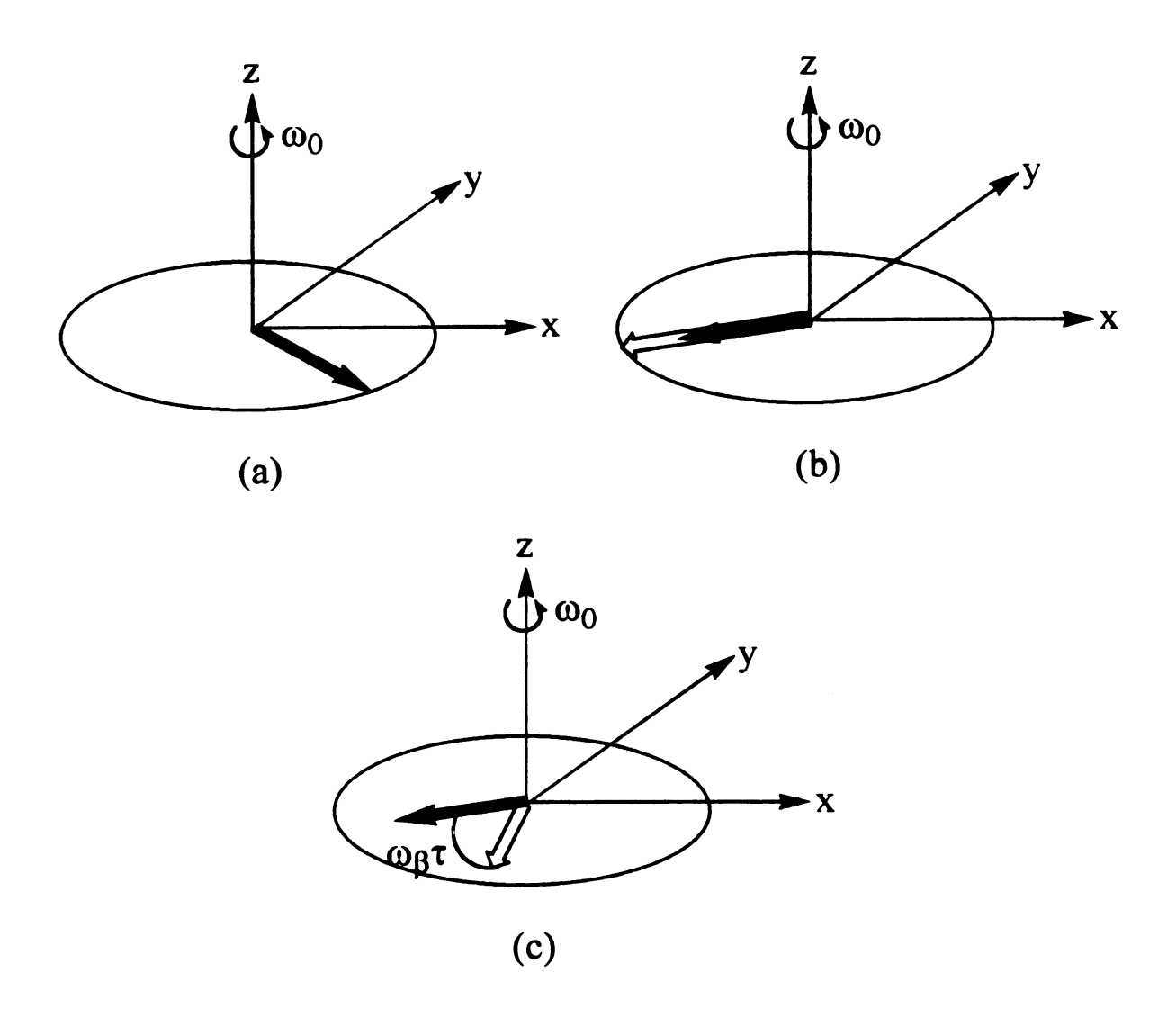


Figure 3.5: The combination of quantum mechanical results with classical results of an ESEEM experiment.

first precession period  $\tau$ , the spin packet falls behind the precessional frequency of the frame, so that it develops a phase  $(\omega_{23} - \omega_0)\tau$  with respect to the x-axis. After the  $180^0$  pulse, the spin packet is torqued  $180^0$  about the y-axis, and part of it splits into a smaller packet that will precess at  $\omega_{24}$ , as it has made the transition from  $|2\rangle$  to  $|4\rangle$ . Since  $\omega_{24}$  is larger than  $\omega_0$ , this packet will precess opposite that with the  $\omega_{23}$  frequency, and will interfere with the echo formation at time  $\tau$  after the second pulse. This phenomenon is known as "branching". The interference is modulated as the time between the  $90^0$  and  $180^0$  pulses is varied with a frequency of  $|\omega_{23} - \omega_{24}| = \omega \beta$ .

Two-Pulse ESEEM For A Spin System With S = 1/2 and I=1

For a system with electron spin  $S = \frac{1}{2}$  and nuclear spin I = 1, such as  $^{14}N$ , the energy level diagram becomes more complicated than the  $S = \frac{1}{2}$  and  $I = \frac{1}{2}$  system shown in Figure 3.4<sup>3</sup>. Figure 3.6<sup>6</sup> illustrates the energy level diagram showing the microwave transitions between the upper and lower electron manifolds. At the beginning of the two-pulse ESEEM experiment, the electron spin is in state I = 1. After the first I = 1 microwave pulse, the allowed transition I = 1 microwave pulse, the allowed transition I = 1 microwave pulse, and  $I = \frac{1}{2}$  and  $I = \frac{1}{2}$  system shown in Figure 3.4<sup>3</sup>. Figure 3.6<sup>6</sup> illustrates the energy level diagram showing the microwave transitions between the upper and lower electron manifolds. At the beginning of the two-pulse ESEEM experiment, the electron spin is in state I = 1. After the first I = 1 microwave pulse, the allowed transition I = 1 microwave pulse, and  $I = \frac{1}{2}$  and  $I = \frac{1}{2}$  system shown in Figure 3.4<sup>3</sup>. Figure 3.6<sup>6</sup> illustrates the energy level diagram showing the microwave transitions between the upper and lower electron manifolds. At the beginning of the two-pulse ESEEM experiment, the electron spin is in state  $I = \frac{1}{2}$  and  $I = \frac{1}{2}$  system shown in Figure 3.4<sup>3</sup>. Figure 3.6<sup>6</sup> illustrates the energy level diagram showing the microwave transitions of the microwave pulse, and  $I = \frac{1}{2}$  and  $I = \frac{1}{2}$  system shown in Figure 3.4<sup>3</sup>. Figure 3.6<sup>6</sup> illustrates the energy level diagram showing the microwave pulse, and  $I = \frac{1}{2}$  system shown in Figure 3.6<sup>6</sup> illustrates the energy level diagram showing the microwave pulse, and  $I = \frac{1}{2}$  system shown in Figure 3.6<sup>6</sup> illustrates the energy level diagram showing the microwave pulse, and  $I = \frac{1}{2}$  system shown in Figure 3.6<sup>6</sup> illustrates the energy level diagram showing the microwave pulse, and  $I = \frac{1}{2}$  system shown in Figure 3.6<sup>6</sup> illustrates the energy level diagram showing the microwave pulse, and  $I = \frac{1}{2}$  system shown in F

During the time  $\tau$  between the first and second pulses, the states |1>, |2>, and |3> evolve with the phase factors  $e^{(-iE/\nu/h)}$ ,  $e^{(-iE2\nu/h)}$ , and  $e^{(-iE3\nu/h)}$  respectively. The second 180° microwave pulse induces the allowed transitions |1> to |4>, |2> to |5>, and |3> to |6>, as well as the semiforbidden transitions |1> to |5>, |1> to |6>, |2> to |4>, |2> to |6>, |3> to

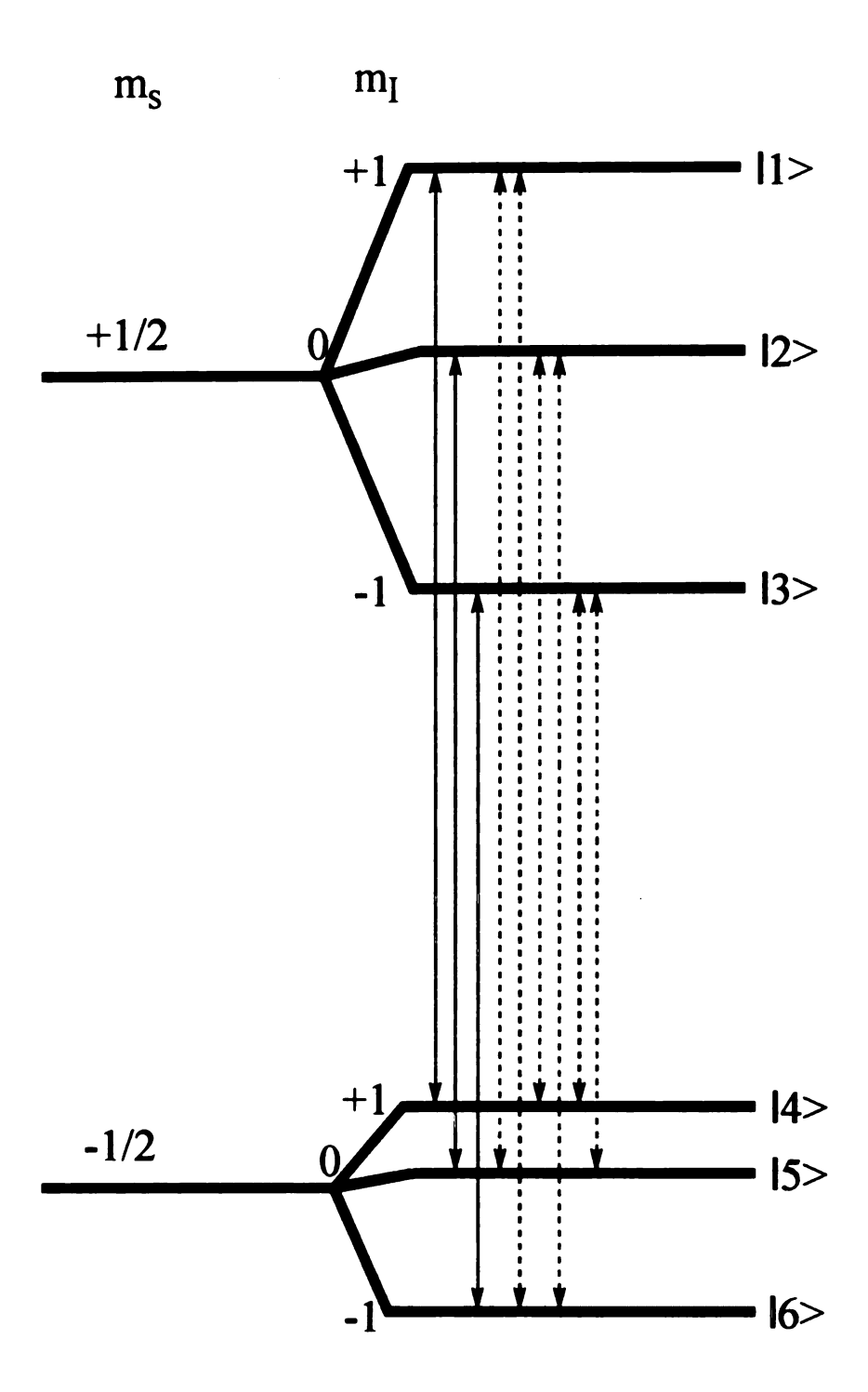


Figure 3.6: The energy level diagram for an  $S = \frac{1}{2}$ , I = 1 spin system, showing the three allowed and six semiforbidden transitions.

14>, and 13> to 15>. During the time  $\tau$  between the second pulse and the echo, the additional phase factors  $e^{(-iE4\tau/\hbar)}$ ,  $e^{(-iE5\tau/\hbar)}$ , and  $e^{(-iE6\tau/\hbar)}$  become part of the wave function. Thus, the echo is generated mostly by the allowed transitions, but also in part by the semiforbidden transitions, and changes in echo amplitude are a result of interference between the components of the wave function.

## Modulations Of Two-Pulse ESEEM

For a two-pulse ESEEM experiment with  $S = \frac{1}{2}$  and  $I = \frac{1}{2}$ , the modulation function is given by

 $E_{mod}(\tau) = |u|^4 + |v|^4 + |u|^2 |v|^2 [\cos \omega_{\alpha} \tau + 2\cos \omega_{\beta} \tau - \cos(\omega_{\alpha} - \omega_{\beta})\tau - \cos(\omega_{\alpha} + \omega_{\beta})\tau].$  (140) From Equation (140), it can be seen that modulations of the two-pulse echo amplitude occur not only at the fundamental hyperfine frequencies, but also at their sum and difference frequencies,  $(\omega_{\alpha} + \omega_{\beta})$  and  $(\omega_{\alpha} - \omega_{\beta})$ . The product of the transition probabilities of the two individual transitions associated with "branching",  $|u|^2 |v|^2$ , describes the amplitude of the modulations. The product of the transition probabilities for the "non-branching" spins,  $|u|^4$  or  $|v|^4$ , describes the non-modulated part of the echo envelope.<sup>3</sup>

In an ESEEM experiment, what is experimentally observed is the product of the modulation function and an exponential decay function, describing the loss of magnetization as a result of spin relaxation. In a two-pulse experiment, spin-spin relaxation is generally on the order of one µsec. This rapid background decay reduces the frequency resolution in two-pulse experiments.<sup>3</sup>

When multiple nuclei contribute to the modulation of a single paramagnetic center, the modulation function becomes the product of each individual modulation

function, given by

$$E(\tau) = V_{\text{decay}} \prod_{i=1}^{N} E_{\text{mod}}^{i}(\tau)$$
 (141)

where N is the number of coupled nuclei. From Equation (141), it can be seen how complex a two-pulse ESEEM experiment can become if just a few nuclei contribute, because for each nucleus, there will be fundamental  $\Delta m_I = \pm 1$  frequencies and combination frequencies, and also there will be new frequencies representing combinations of the frequencies from different nuclei as well.<sup>3</sup>

## Three-Pulse ESEEM

Reduction of resolution and increase in complexity are two problems with two-pulse ESEEM that may be avoided by using three-pulse ESEEM. In a three-pulse ESEEM experiment, the microwave pulse sequence is 90°-τ-90°-T-90°, as shown in Figure 3.7. The first 90° pulse transfers the bulk magnetization vector M along the v-axis, shown in Figure 3.8<sup>5</sup>. During the first time τ, the bulk magnetization dephases and the individual spin packets precess with their characteristic angular frequencies. The second 90° pulse rotates the individual magnetization vectors into the xz plane. During time T, the transverse magnetization decays, meaning that the individual spin packets relax back to the z-axis. The third 90° pulse restores the transverse magnetization by transferring the spin packets along the z-axis onto the y-axis. After time  $\tau$  again, the individual spin packets dephase about the y-axis, such that the tips of their vectors form the locus of a circle. At time T+2 $\tau$  from the beginning of the experiment a stimulated echo is formed along the v-axis.<sup>5</sup> In a three-pulse sequence, the background decay is dependent on electron spin-lattice relaxation, T<sub>1</sub>, which is much longer than spin-spin relaxation. This allows for better frequency resolution as compared to the two-pulse

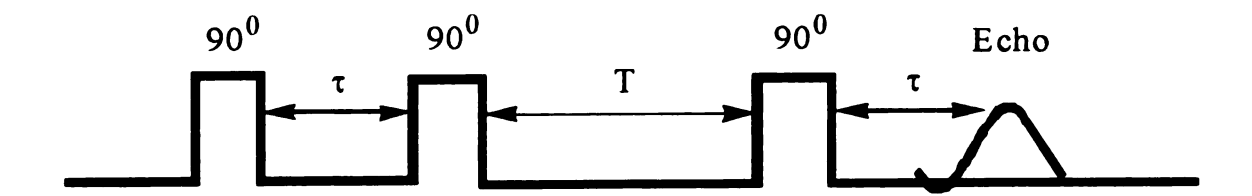


Figure 3.7: The microwave pulse sequence of a three-pulse ESEEM experiment.

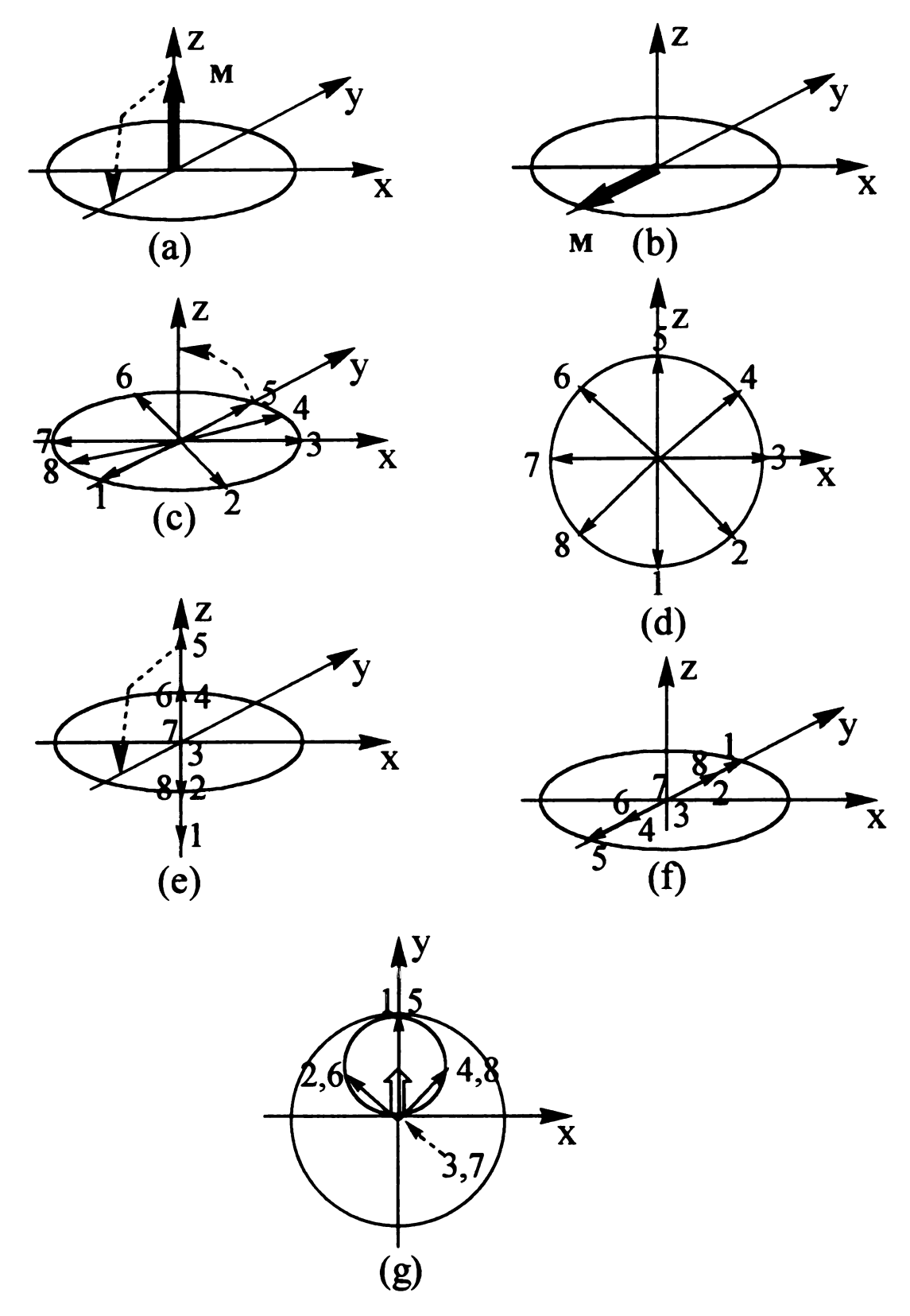


Figure 3.8: The classical picture of a three-pulse ESEEM experiment describing the formation of a stimulated echo.

experiment.<sup>3</sup>

#### Modulations Of Three-Pulse ESEEM

For a three-pulse ESEEM experiment, the modulation function for an  $S=\frac{1}{2}$  and  $I=\frac{1}{2}$  system is

$$E_{\text{mod}}(\tau, T) = |u|^{4} + |v|^{4} + |u|^{2}|v|^{2} \left\{ \cos \omega_{\alpha} \tau + \cos \omega_{\beta} \tau + 2\sin^{2} \left( \frac{\omega_{\alpha} \tau}{2} \right) \cos \left[ \omega_{\beta} (\tau + T) \right] \right\} + 2\sin^{2} \left( \frac{\omega_{\beta} \tau}{2} \right) \cos \left[ \omega_{\alpha} (\tau + T) \right]. \tag{142}$$

As shown in Equation (142), the modulations observed in three-pulse ESEEM are those of the fundamental hyperfine frequencies, and not the combination frequencies.<sup>3</sup>

In a three-pulse ESEEM experiment with multiple nuclei coupled to a single paramagnetic center, the overall modulation function is

$$E(\tau,T) = \left(\frac{V_{\text{decay}}}{2}\right) \left[\prod_{i=1}^{N} E_{\alpha}^{i}(\tau,T) + \prod_{j=1}^{N} E_{\beta}^{i}(\tau,T) + \right]. \tag{143}$$

It is evident from Equation (143) that the products are taken between frequencies of the same electron manifold, and not combinations of the frequencies between the manifolds, as is the case in two-pulse ESEEM. Therefore, three-pulse ESEEM removes much of the complexities that arise in two-pulse ESEEM.

## The $\tau$ -Suppression Effect

It can be seen from Equation (142) that the  $\tau$  values chosen in a three-pulse experiment will affect the amplitudes of the modulations. Therefore, the value of  $\tau$  can be varied over a range of values to either enhance or suppress the contribution from one of the electron spin manifolds. This is known as the " $\tau$ -suppression effect", and is a useful technique to use for making spectral assignments. The condition for suppression of a particular nucleus is that the time  $\tau$  be equal to the inverse of the resonant frequency

 $\nu$  of the nucleus. Using  $\tau$  to suppress a known nucleus in an experimental sample is useful in analyzing ESEEM data because it isolates the other peaks, which makes it easier to assign them.<sup>3</sup>

## Fourier Transformation

The resulting signal of an ESEEM experiment is preceded by a free induction decay spectrum, or an FID spectrum, such as the one shown in Figure  $3.9(a)^2$ . Once the spectrum is obtained, the resonant frequencies present in the FID spectrum must be recovered in some way. The FID curve is a sum of oscillating functions, and so the frequencies can be recovered in terms of the harmonic components of the curve. The FID curve is analysed using a mathematical technique called Fourier transformation. The signal, S(t), is originally in the time domain. The total FID curve is the sum over all possible contributing frequencies, represented by the integral

$$S(t) = \int I(\nu) e^{(-2\pi i \, x)} d\nu. \qquad (144)$$

In Equation (144), I(v) is the intensity of the contribution of the frequency v, and the exponential part,  $e^{(-2\pi i v t)}$ , is the signal oscillating with frequency v. In order to convert the spectrum into the frequency domain, I(v) must be determined, which can be evaluated by the integral

$$I(\nu) = 2re \int_{0}^{\infty} S(t)e^{(2\pi i \kappa)}dt$$
 (145)

where "re" specifies real solutions. This integration is carried out over a series of designated frequencies  $\nu$  on a computer that is a component of the spectrometer. When the FID signal is transformed by this method, a frequency-domain spectrum results, as the one shown in Figure 3.9(b)<sup>2</sup>. The frequency-domain spectrum is much more useful for analysis than the time-domain spectrum because it is easier to assign peaks based on

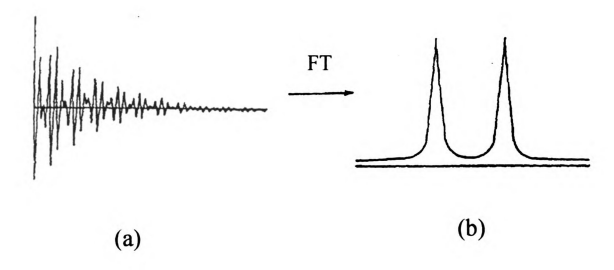


Figure 3.9: (a) The free induction decay (FID) spectrum for an S =  $\frac{1}{2}$ , I =  $\frac{1}{2}$  spin system.

(b) The frequency domain spectrum of the FID spectrum shown in 9(a).

characteristic resonant frequencies rather than on the time that separates the microwave pulses causing the electron spin echo.

#### References

- 1. Banerjee, R., and R. Padmakumar, *The Journal Of Biological Chemistry*. April 21,1995, Vol. 270, No.16, pp. 9295-9300.
- 2. Weil, J. A., J. R. Bolton, and J. E. Wertz. <u>Electron Paramagnetic Resonance</u>. John Wiley & Sons, Inc.: New York, 1994.
- 3. McCracken, John, <u>Handbook Of Electron Spin Resonance</u>, <u>Volume II</u>: <u>Electron Spin Echo Envelope Modulation</u>. C. P. Poole and H. A. Farach.
- 4. Schweiger, Arthur, Angew. Chem. Int. Engl. Vol. 30, 1991, pp. 269-270.
- 5. Doorslaer, Sabine Van, EPR-Group ETH Zurich Home Page, "Three-Pulse ESEEM", 1996.
- 6. Berliner, Lawrence J., and Jacques Reuben, <u>Biological Magnetic Resonance: Volume</u>
  3. Plenum Press: New York, pp. 231-233.
- 7. Atkins, P. W. Physical Chemistry: Fourth Edition. W. H. Freeman and Company: New York, 1990, p. 551.

# Chapter 4: Nuclear Quadrupole Interaction Of <sup>14</sup>N

Nitrogen-14 has a nuclear spin of one, and nuclei with  $I \ge 1$  have nuclear charge distributions that are non-spherical. Such nuclei are said to possess an electric quadrupole moment eQ, where e is the unit of electrostatic charge, and Q is a measure of the deviation of the nuclear charge distribution from spherical symmetry. For a spherical nucleus, eQ equals zero, illustrated in Figure 4.1<sup>1</sup>. For a positive value of Q, the charge is oriented along the direction of the principal axis, which is the axis of the nonbonded electron pair. For a negative value of Q, the charge accumulation is perpendicular to the principal axis.<sup>1</sup>

The quadrupole moment is a property of nuclei with nuclear spin greater than or equal to one, which arises from a non-spherical charge distribution in the nucleus. At the same time, there is an electron distribution on the molecule from the valence electrons which creates an electric field gradient q at the nucleus. When the quadrupole moment and the field gradient interact at the nucleus, the result is what is called a nuclear quadrupole interaction. Therefore, the nuclear quadrupole interaction is an electrostatic interaction between the quadrupole moment of a nucleus and the electric field gradient at the nucleus due to the surrounding electronic charges in an atom or molecule. <sup>1</sup>

Deriving the Nuclear Quadrupole Interaction Energies For An I=1 Nucleus

The nuclear quadrupole interaction hamiltonian for an I=1 nucleus is

$$\hat{H}_{Q} = \frac{\text{eq(eQ)}}{4} \left[ 3\hat{\mathbf{I}}_{z}^{2} - 2 + \eta \left( \hat{\mathbf{I}}_{x}^{2} - \hat{\mathbf{I}}_{y}^{2} \right) \right]$$
 (146)

where e is the fundamental charge, q is the field gradient, eQ is the electric quadrupole moment, and the operator of  $I_z$  is the z component of the nuclear spin angular momentum

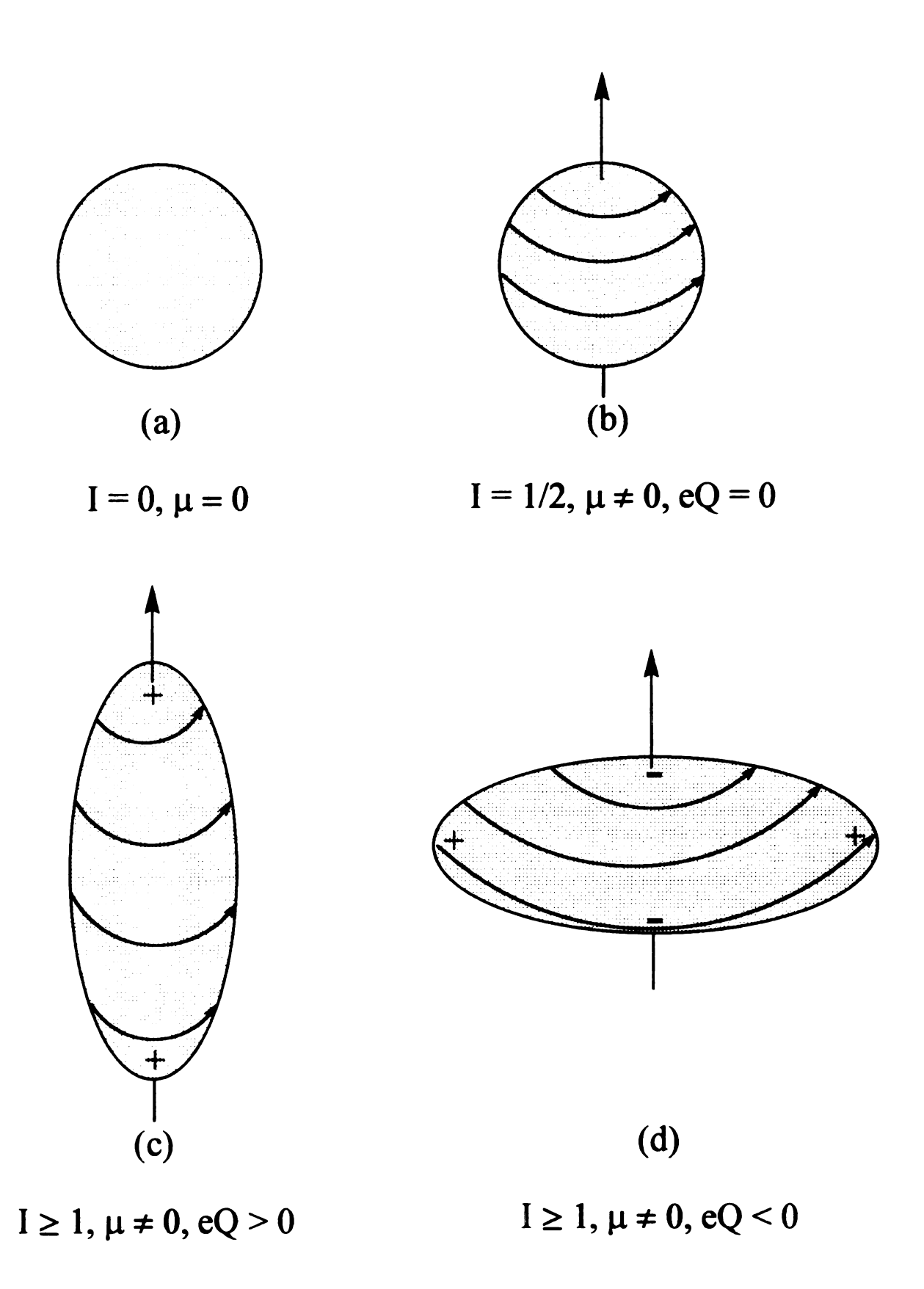


Figure 4.1: Different types of nuclei, varying in charge distributions.

operator.<sup>3</sup> The x and y components of the nuclear spin angular momentum operator, the operators of  $I_x$  and  $I_y$  respectively, can be used to define the step operators of  $I_+$  and  $I_-$  by the two equations

$$\hat{\mathbf{I}}_{\perp} = \hat{\mathbf{I}}_{\nu} + i\hat{\mathbf{I}}_{\nu} \tag{147}$$

and

$$\hat{\mathbf{I}}_{-} = \hat{\mathbf{I}}_{x} - i\hat{\mathbf{I}}_{y}. \tag{148}$$

The x and y components can be defined in terms of these two step operators as

$$\hat{\mathbf{I}}_{x} = \frac{\left(\hat{\mathbf{I}}_{+} + \hat{\mathbf{I}}_{-}\right)}{2} \tag{149}$$

and

$$\hat{\mathbf{I}}_{y} = \frac{\left(\hat{\mathbf{I}}_{\perp} - \hat{\mathbf{I}}_{\perp}\right)}{2i}.$$
 (150)

Squaring both sides of Equation (149) and Equation (150) will give

$$\hat{\mathbf{I}}_{x}^{2} = \frac{1}{4} \left[ \hat{\mathbf{I}}_{+}^{2} + 2\hat{\mathbf{I}}_{+}\hat{\mathbf{I}}_{-} + \hat{\mathbf{I}}_{-}^{2} \right]$$
 (151)

and

$$\hat{\mathbf{I}}_{y}^{2} = -\frac{1}{4} \left[ \hat{\mathbf{I}}_{+}^{2} - 2\hat{\mathbf{I}}_{+} \hat{\mathbf{I}}_{-}^{2} + \hat{\mathbf{I}}_{-}^{2} \right]. \tag{152}$$

Therefore

$$(\hat{\mathbf{I}}_{x}^{2} - \hat{\mathbf{I}}_{y}^{2}) = \frac{1}{2}(\hat{\mathbf{I}}_{+}^{2} + \hat{\mathbf{I}}_{-}^{2})$$
(153)

and the hamiltonian of Equation (146) becomes

$$\hat{H}_{Q} = \frac{\text{eq(eQ)}}{4} \left[ 3\hat{\mathbf{I}}_{z}^{2} - 2 + \left( \frac{\eta}{2} \right) (\hat{\mathbf{I}}_{+}^{2} + \hat{\mathbf{I}}_{-}^{2}) \right]. \tag{154}$$

The Schrodinger equations for the operators of  $I_z$ ,  $I_+$ , and L are

$$\hat{\mathbf{I}}_z | \mathbf{I} \quad \mathbf{m}_1 \rangle = \mathbf{m}_1 | \mathbf{I} \quad \mathbf{m}_1 \rangle \tag{155}$$

$$\hat{\mathbf{I}}_{+}|\mathbf{I} \quad \mathbf{m}_{1}\rangle = [\mathbf{I}(\mathbf{I}+1) - \mathbf{m}_{1}(\mathbf{m}_{1}+1)]^{\frac{1}{2}}|\mathbf{I} \quad (\mathbf{m}_{1}+1)\rangle$$
 (156)

and

 $\hat{I}_{-}|I_{-}|I_{-}|$   $m_{1}\rangle = [I(I+1)-m_{1}(m_{1}-1)]^{\frac{1}{2}}|I_{-}|$   $(m_{1}-1)\rangle$ . (157) When Equations (155), (156), and (157) are applied to the three nuclear spin states of an I = 1 nucleus, the eigenvalues for the three nuclear spin operators can be determined, as summarized in Table 4.1. When applying the hamiltonian to the diagonal terms, the results are

$$\langle -1|\hat{H}_{Q}|-1\rangle = \left(\frac{e^2qQ}{4}\right)(1) \tag{158}$$

$$\langle 0|\hat{\boldsymbol{H}}_{Q}|0\rangle = \left(\frac{e^2qQ}{4}\right)(-2) \tag{159}$$

and

$$\langle +1|\hat{\boldsymbol{H}}_{Q}|+1\rangle = \left(\frac{e^2qQ}{4}\right)(1).$$
 (160)

In each of the solutions for the diagonal terms, the  $\eta$  term vanishes. This is due to orthogonality of the eigenfunctions that arise from the step function operators, which are given in Table 4.1. Along with the three diagonal terms, there are two nonzero off-diagonal terms, which are

$$\langle -1|\hat{\boldsymbol{H}}_{Q}|+1\rangle = \left(\frac{\mathbf{e}^2 \mathbf{q} \mathbf{Q}}{4}\right)(\boldsymbol{\eta})$$
 (161)

and

Table 4.1: The solutions of Equations (156), (157), and (158) for the three nuclear spin states  $m_I = -1$ , 0, and +1.

I	${\sf m}_{ m I} \rangle$	$\hat{\mathbf{I}}_{\mathbf{z}}$	Î <sub>+</sub>	Î_

1 -1>	-1  1 -1>	2 <sup>1/2</sup>   11   0>	0   1 -2>
l1 0>	0   1 0 >	2 <sup>1/2</sup>   1 +1>	21/2   1 -1>
l1 +1>	+1  1 +1>	0   1 +2>	21/2   1   0>

$$\langle +1|\hat{H}_{Q}|-1\rangle = \left(\frac{e^2qQ}{4}\right)(\eta).$$
 (162)

The completed matrix in terms of Im<sub>I</sub>> is

$$|0\rangle \qquad |-1\rangle \qquad |+1\rangle$$

$$|0\rangle \qquad \left(\frac{e^2qQ}{4}\right)(-2) \qquad 0 \qquad 0$$

$$|-1\rangle \qquad 0 \qquad \left(\frac{e^2qQ}{4}\right)(+1) \qquad \left(\frac{e^2qQ}{4}\right)(\eta)$$

$$|+1\rangle \qquad 0 \qquad \left(\frac{e^2qQ}{4}\right)(\eta) \qquad \left(\frac{e^2qQ}{4}\right)(+1)$$

Substituting x for (e<sup>2</sup>qQ/4), the matrix can be written as

$$\begin{bmatrix} -2\mathbf{x} & 0 & 0 \\ 0 & \mathbf{x} & \mathbf{x}\boldsymbol{\eta} \\ 0 & \mathbf{x}\boldsymbol{\eta} & \mathbf{x} \end{bmatrix}.$$

This matrix will be used to solve for the energies  $E_{-1}$ ,  $E_0$ , and  $E_{+1}$ . The "characteristic equation" of this matrix is

$$\begin{vmatrix} -2x - \lambda & 0 & 0 \\ 0 & A - \lambda & A' \\ 0 & A' & A - \lambda \end{vmatrix} = 0.$$
 (163)

From the above characteristic equation,  $-2x-\lambda=0$ , and solving for  $\lambda$  yields  $E_o=-(e^2qQ/2)$ . The other two energies,  $E_{+1}$  and  $E_{-1}$ , are found by solving the remaining determinant within the original characteristic equation, which is

$$\begin{vmatrix} \mathbf{A} - \lambda & \mathbf{A}' \\ \mathbf{A}' & \mathbf{A} - \lambda \end{vmatrix} = 0. \tag{164}$$

The two energies are found by solving for  $\lambda$  from the above determinant. There are two solutions to the determinant, the first is  $\lambda = (e^2 qQ/4)(1-\eta)$ , and the second is

 $\lambda = (e^2 q Q/4)(l+n)$ . Therefore, the two energies for the  $m_I = +1$  and  $m_I = -1$  nuclear states are  $E_{+1} = (e^2 q Q/4)(l \pm \eta)$ .

Resonant Frequencies Of the Nuclear Quadrupole Interaction

Now that the three energies for the nuclear quadrupole interaction of  $^{14}N$  have been determined, it is possible to solve for the corresponding resonant frequencies. There are three possible energy level transitions,  $E_o \rightarrow E_{+1}$ ,  $E_{-1} \rightarrow E_{+1}$ , and  $E_o \rightarrow E_{-1}$ . Calculating these changes in energies will yield the three characteristic resonant frequencies of the nuclear quadrupole interaction.

The first energy transition is  $E_o \rightarrow E_{+1}$ , which is given by the equation

$$E_{+1} - E_{0} = \left(\frac{e^{2}qQ}{4}\right) [(1+\eta) - (-2)] = \left(\frac{e^{2}qQ}{4}\right) (3+\eta).$$
 (165)

The second transition is  $E_{-1} \rightarrow E_{+1}$ ,

$$E_{+1} - E_{-1} = \left(\frac{e^2 qQ}{4}\right) \left[ (1+\eta) - (1-\eta) \right] = \left(\frac{e^2 qQ}{2}\right) (\eta).$$
 (166)

The third and final transition is  $E_{-1} \rightarrow E_{0}$ ,

$$E_{-1} - E_0 = \left(\frac{e^2 qQ}{4}\right) [(1-\eta) - (-2)] = \left(\frac{e^2 qQ}{4}\right) (3-\eta).$$
 (167)

The three changes in energies given in Equations (165), (166), and (167) correspond to the three characteristic frequencies of the nuclear quadrupole interaction of <sup>14</sup>N. The three frequencies are given by

$$v_{+} = \left(\frac{e^2 qQ}{4}\right) (3+\eta) \tag{168}$$

$$v_{-} = \left(\frac{e^2 qQ}{4}\right) (3 - \eta) \tag{169}$$

and

$$v_0 = \left(\frac{e^2 qQ}{2}\right) (\eta)$$
 where  $(e^2Q/4) = 1.207 \times 10^{-6} \text{ (cm}^2C \text{ MHz)/J}.$ 

Solving For the Field Gradient q and the Asymmetry Parameter  $\eta$ 

Using the nuclear quadrupole resonant frequencies for  $^{14}N$ ,  $v_+$ ,  $v_-$ , and  $v_0$ , it is possible to determine the value of q, the constant describing the field gradient. The equation for  $v_+$  is given in Equation (168), and that of  $v_-$  is given in Equation (169). Subtracting  $v_-$  from  $v_+$  gives

$$\left(\nu_{+} - \nu_{-}\right) = \left(\frac{\mathrm{e}^{2} \mathrm{q} \mathrm{Q}}{4}\right) (2\eta) \tag{171}$$

which is  $v_0$ . The electric quadrupole moment eQ for <sup>14</sup>N is  $2.0x10^{-26}$  cm<sup>2</sup>, <sup>5</sup> and the fundamental charge e is  $1.6x10^{-19}$  C.<sup>5</sup> Thus (e<sup>2</sup>Q)/4 is  $8.0x10^{-46}$  (cm<sup>2</sup> C), which in terms of MHz becomes  $1.207x10^{-6}$  (cm<sup>2</sup> C MHz)/J. Substituting this value into Equation (171) and solving for qn gives

$$q\eta = 2v_o/(e^2Q). \tag{172}$$

Going back to  $v_+$ , Equation (168) can be rewritten as

$$\left[3.621 \times 10^{-6} \left(\frac{\text{cm}^2 \text{ C MHz}}{\text{J}}\right)\right] q + \left[1.207 \times 10^{-6} \left(\frac{\text{cm}^2 \text{ C MHz}}{\text{J}}\right)\right] (q \eta) = \nu_{+} \quad (173)$$

by distribution and substitution. From this equation, the field gradient constant q can be calculated. Once q has been determined, it can be substituted into Equation (172) to find the asymmetry parameter  $\eta$ .

Deriving the Energy Level Diagram For An  $S = \frac{1}{2}$  and I = 1 System

Knowing the three energies of a nucleus with spin I=1, the energy level diagram can be derived for a nucleus such as  $^{14}N$  coupled to an electron. There are two possible spin orientations for the unpaired electron, spin up or spin down,  $m_s=+\frac{1}{2}$  and  $m_s=-\frac{1}{2}$  respectively. This degenerate electron spin state is first split due to the electron Zeeman interaction energy, given by

$$\Delta E = -g_e \beta_e B \tag{174}$$

shown in Figure 4.2(a).<sup>6,3</sup> For the case where the external magnetic field B is 3060 G,  $\Delta E$  is 5.6757xl0<sup>-27</sup> kJ, or 8.5658x10<sup>3</sup> MHz.

Each of the electron spin states is further split by the nuclear Zeeman interaction.<sup>3</sup> With a nuclear spin I=1, each electron energy level is split into three levels because there are three nuclear spin states,  $m_I=+1$ ,  $m_I=0$ , and  $m_I=-1$ . The nuclear Zeeman energy is related to the nuclear Larmor frequency by the relationship

$$g_n \beta n B/h = v_n.^6 \tag{175}$$

At 3060 G,  $v_n$  is 0.94 MHz. Therefore, at the upper electron manifold, the three nuclear Zeeman levels will be  $m_I = -1,0$ , and +1 respectively, and the levels will be split by 0.94 MHz, as shown in Figure 4.2(b). Similarly, at the lower electron manifold, the three nuclear Zeeman levels will be  $m_I = -1,0$ , and +1 respectively, and again each level will be split 0.94 MHz apart, shown in Figure 4.2(b).

The nuclear Zeeman energy levels are shifted due to the electron-nuclear hyperfine interaction energy, given by  $Am_Im_s$ . Thus, at the upper electron manifold,  $m_I = -1$  level is decreased by A/2, A being the hyperfine coupling constant of <sup>14</sup>N, and the  $m_I = +1$  level is increased by A/2, as shown in Figure 4.2 (c). At the lower electron

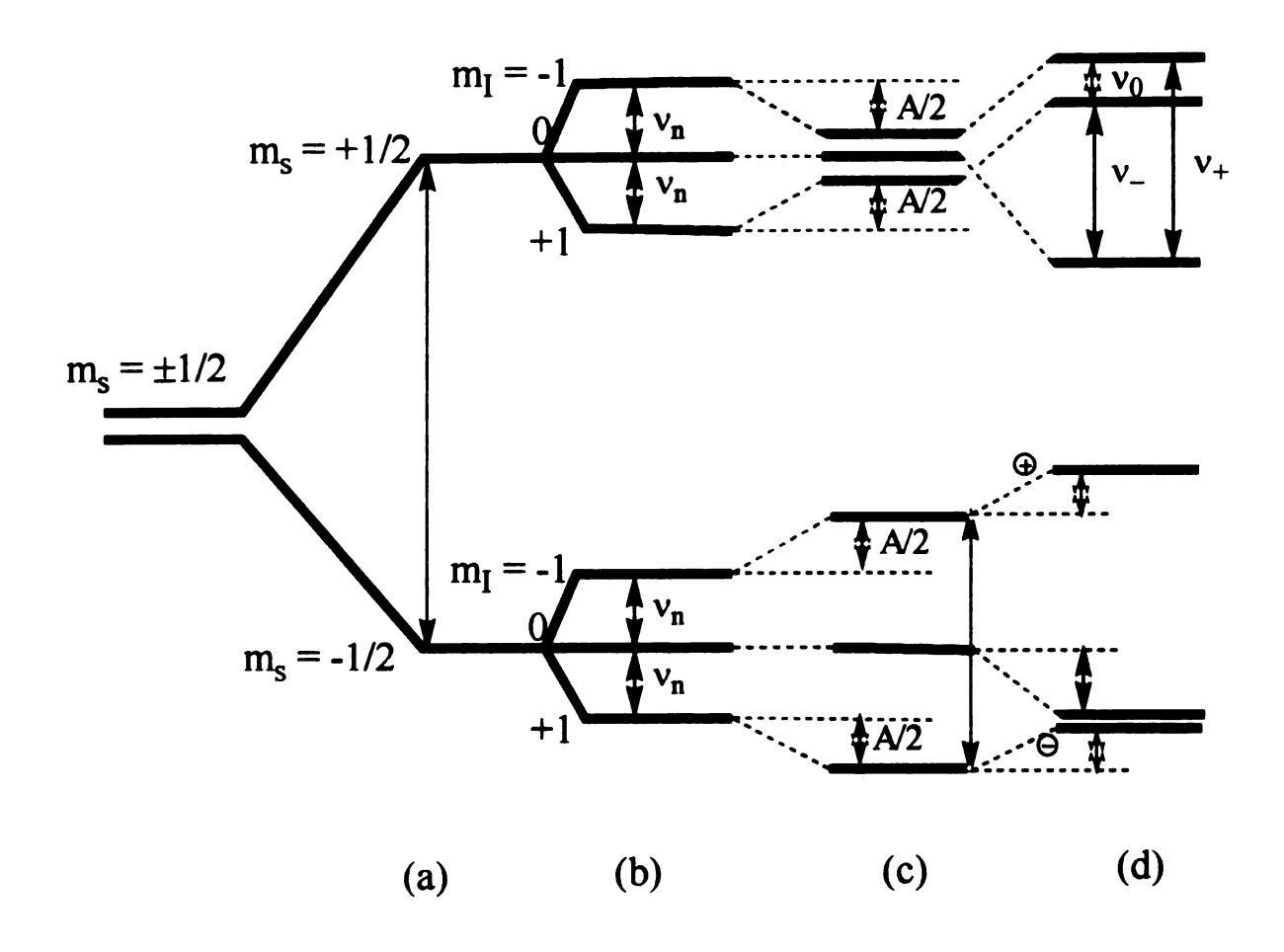


Figure 4.2: The energy splitting diagram of  $^{14}N$ , showing splittings from the (a) electron Zeeman energy  $[-g_e\beta_eBm_s]$ , (b) nuclear Zeeman interaction  $[-g_n\beta_nB/h = -\nu_n]$ , (c) the electron-nuclear hyperfine interaction  $[Am_em_I]$ , and (d) nuclear quadrupole interaction.  $\nu_n$  is the Larmor frequency, which is .94 MHz at 3060 G.

manifold, the  $m_I = -1$  level is increased by A/2 while the  $m_I = +1$  level is decreased by A/2. In both electron manifolds, the  $m_I = 0$  level is neither raised nor lowered.

Each of the electron-nuclear hyperfine levels for  $^{14}N$  is shifted due to the nuclear quadrupole interaction. Solving the nuclear quadrupole interaction hamiltonian for  $^{14}N$ , the quadrupole energy level shifts corresponding to  $m_I = 0, \pm 1$  are

$$E_{ml=0} = -(e^2qQ)/2 (176)$$

$$E_{ml=+1} = (e^2 qQ/4)(1+\eta)$$
 (177)

and

$$E_{mI-1} = (e^2 qQ/4)(1-\eta). \tag{178}$$

In the upper electron manifold in Figure 4.2, the nuclear Zeeman and electron-nuclear hyperfine terms almost cancel each other, thereby leaving only the nuclear quadrupole interaction to determine the energy level splitting. This gives rise to three transitions corresponding to the three sharp lines in the ESEEM spectra with nuclei with spin  $I \ge 1$ , where the frequencies of two add to give the third.<sup>3</sup>

In the second electron manifold in Figure 4.2, the nuclear Zeeman term is almost doubled by the electron nuclear coupling. This gives rise to a single broad transition peak at about four times the nuclear Zeeman frequency, leading to a  $\Delta m_I = 2$  transition.<sup>2</sup>

Thus, in a frequency domain ESEEM spectrum of <sup>14</sup>N coupled to an unpaired electron, one would expect to see three characteristic sharp peaks between zero and about two MHz, and one broad peak at about four MHz, such as the spectrum shown in Figure 4.3<sup>3</sup>.3

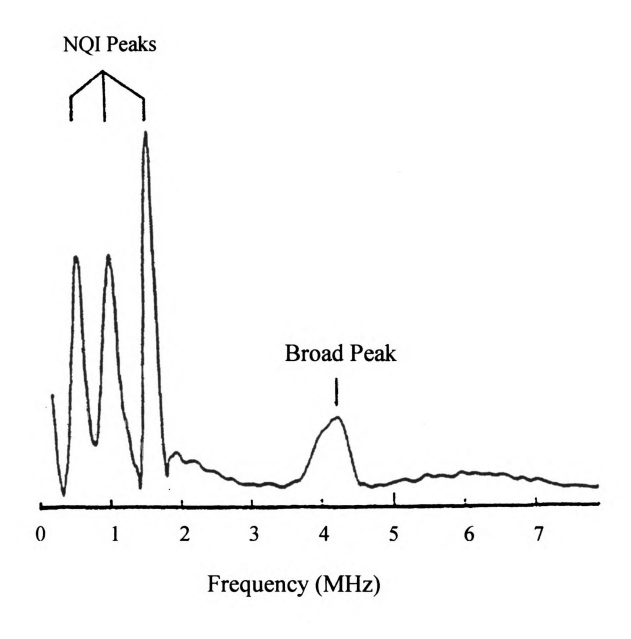


Figure 4.3: The Fourier transformation spectrum of <sup>14</sup>N.

#### References

- 1. Drago, R., Physical Methods For Chemists. Saunders College Publishers: Fort Worth, 1992.
- 2. Weil, J. A., J. R. Bolton, and J. E. Wertz. <u>Electron Paramagnetic Resonance</u>. John Wiley & So, Inc.: New York, 1994, p. 534.
- 3. Jiang, Feng, John McCracken, and Jack Peisach, *Journal Of the American Chemical Society*, **1990**, Vol. 112, No. 25.
- 4. Boas, Mary. Mathematical Methods In the Physical Sciences: Second Edition. John Wiley and Sons: New York, 1983, p. 414.
- 5. Lide, David R., Ph.D. <u>CRC Handbook Of Physics and Chemistry</u>: 72<sup>nd</sup> Edition. CRC Press Inc.: Boca Raton, 1992.
- 6. Weil, J. A., J. R. Bolton, and J. E. Wertz. <u>Electron Paramagnetic Resonance</u>. John Wiley & Sons, Inc.: New York, 1994, pp. 48-50, 463.

# Chapter 5: ESEEM Of Methylmalonyl-CoA Mutase With L-Methylmalonyl-CoA With <sup>14</sup>N

#### **ESEEM Data Collection**

The ESEEM data were collected on a home built spectrometer. A three-pulse sequence (90°-τ-90°-T-90°) was used. Dead time reconstruction was performed prior to Fourier transformation. Computer simulations of the ESEEM data were performed on a Sun Sparcstation 2 computer using FORTRAN software, which is based on the density matrix formalism of Mims.<sup>1</sup>

### Samples Of Methylmalonyl-CoA Mutase

Three-pulse ESEEM experiments were performed on frozen samples of the enzyme methylmalonyl-CoA mutase with the substrate L-methylmalonyl-CoA. The samples were prepared by Rugmini Padmakumar.<sup>2</sup> The sample used was prepared with all the nitrogens being <sup>14</sup>N.

# ESEEM Of <sup>14</sup>N Samples

The first experiment was a two-pulse echo-detected EPR experiment at a  $\tau$  value fixed at 500 ns. The result is known as a "field scan", because the external magnetic field was varied as the echo amplitude was monitored. The resulting spectrum is shown in Figure 5.1. This experiment was done in order to recognize at which field value the greatest echo amplitude would occur. The greatest field value was about 3060 G, and a shoulder was present at about 3140 G. These are the two field values at which the ESEEM experiments were to be performed.

The next experiment was a three-pulse ESEEM experiment at 3060 G. The first  $\tau$ 

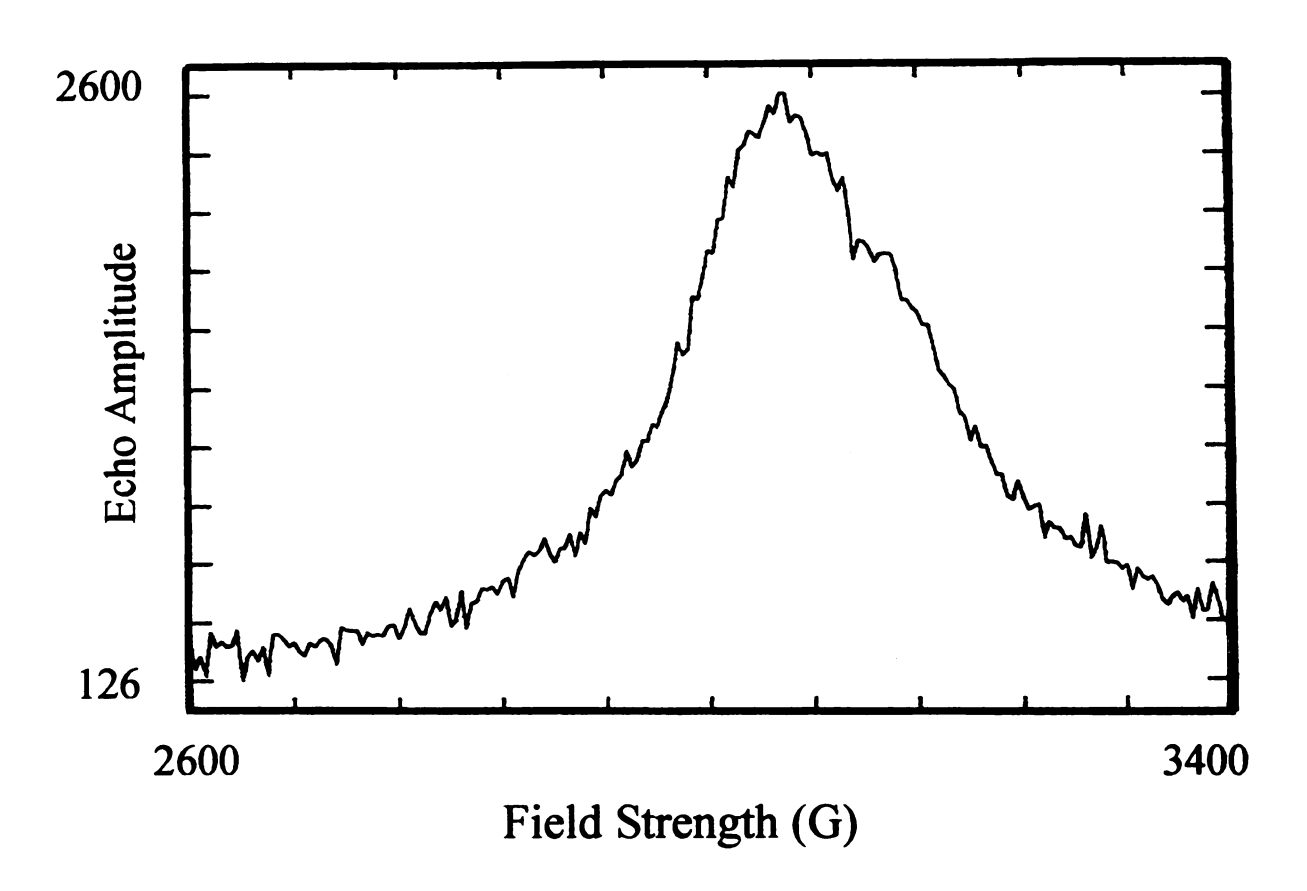


Figure 5.1: The field scan of mmCoA mutase with L-mmCoA, with the frequency at 8.81 GHz and a  $\tau$  value of 500 ns.

value was set at 300 ns, while the time between the second and third pulses, T, was varied. The echo amplitude was detected as a function of T. The resulting spectrum, shown in Figure 5.2, was an electron spin echo decay envelope, which is an overall decay of the magnetization that is modulated by the hyperfine interactions. The spectrum gave a measure of the echo amplitude as a function of the time  $(\tau + T)$  in  $\mu$ sec. Fourier transforming this time domain decay spectrum gave the frequency domain spectrum shown in Figure 5.3. The Fourier transformation spectrum showed frequency peaks at which the nuclear spins present came into resonance at the given magnetic field values, which was useful for identifying the nuclei coupled to the paramagnetic center. The spectrum in Figure 5.3 showed prominent peaks at 1.95 MHz, 2.51 MHz, and 4.0 MHz at 3060 G. Figure 5.4 shows the Fourier transformation spectrum that was taken at 3140 G. The spectrum in Figure 5.4 showed peaks at 2.0 MHz, 2.5 MHz, and 3.9 MHz, which was in very good agreement with the spectrum taken at 3060 G shown in Figure 5.3.

#### Discussion

The peaks present in the Fourier transformation spectra of mmCoA mutase with L-mmCoA, shown in Figure 5.3 and Figure 5.4, were characteristic of the peaks for  $^{14}$ N.  $^{14}$ N has a nuclear spin of one, and nuclei with I  $\geq$  1 have a nuclear quadrupole interaction associated with them. In the two ESEEM spectra, two sharp peaks were in the region between zero and two MHz, while one broad peak was at about four MHz. These peaks could have been assigned to  $^{14}$ N, indicating that  $^{14}$ N was interacting with the paramagnetic center. The one peak absent from the nuclear quadrupole interaction peaks was at too low of a frequency to be detected.

The two sharp peaks at frequencies of about 2.5 MHz and 2.0 MHz were the

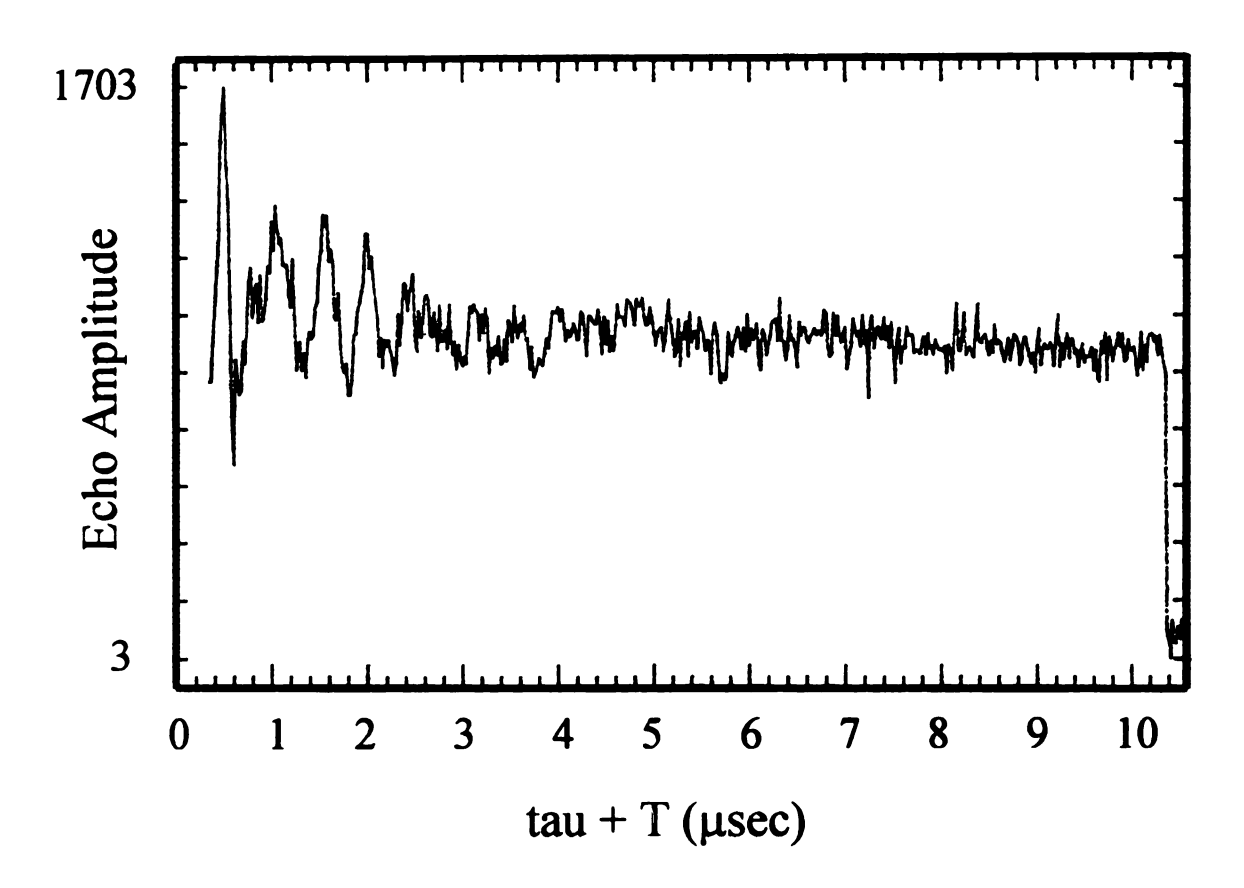


Figure 5.2: The electron spin echo decay envelope of mmCoA mutase with L-mmCoA at 3060 G, with the frequency at 8.81 GHz and a  $\tau$  value of 300 ns.

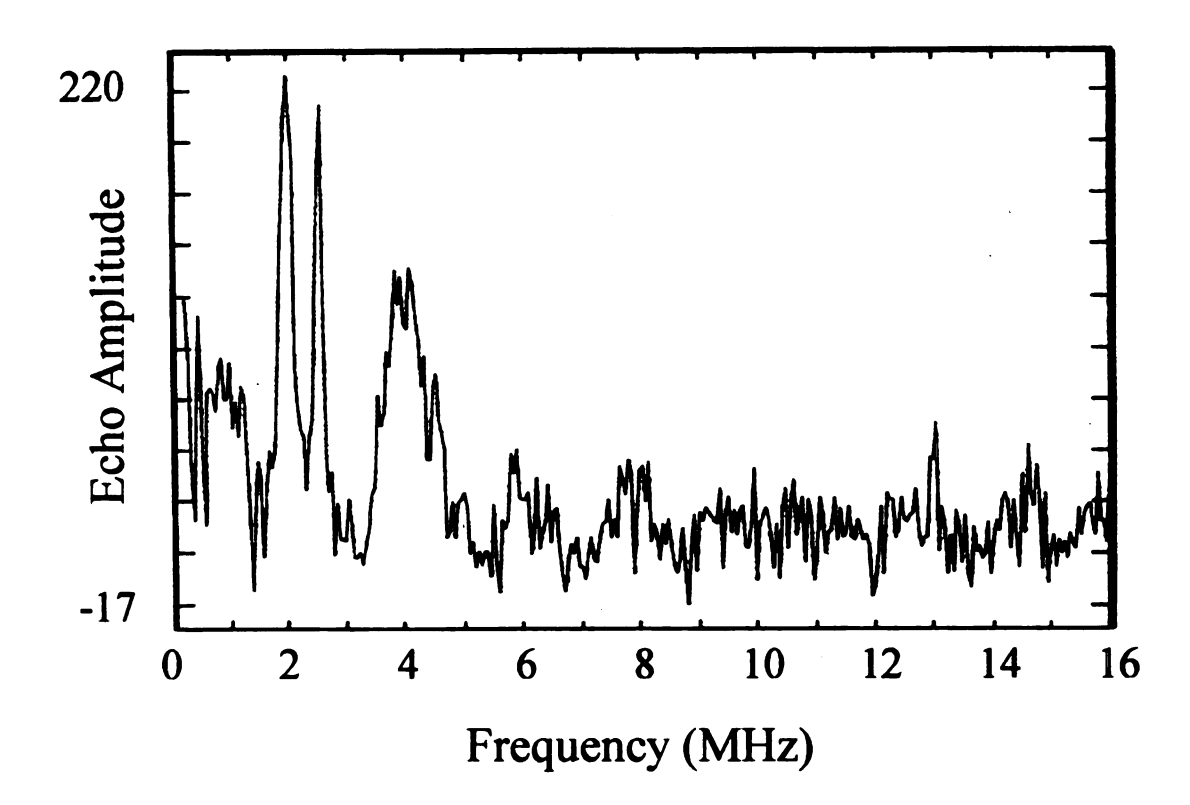


Figure 5.3: The Fourier transformation of the spectrum shown in Figure 5.2 at 3060 G, with the frequency at 8.81 GHz and a  $\tau$  value of 300 ns.

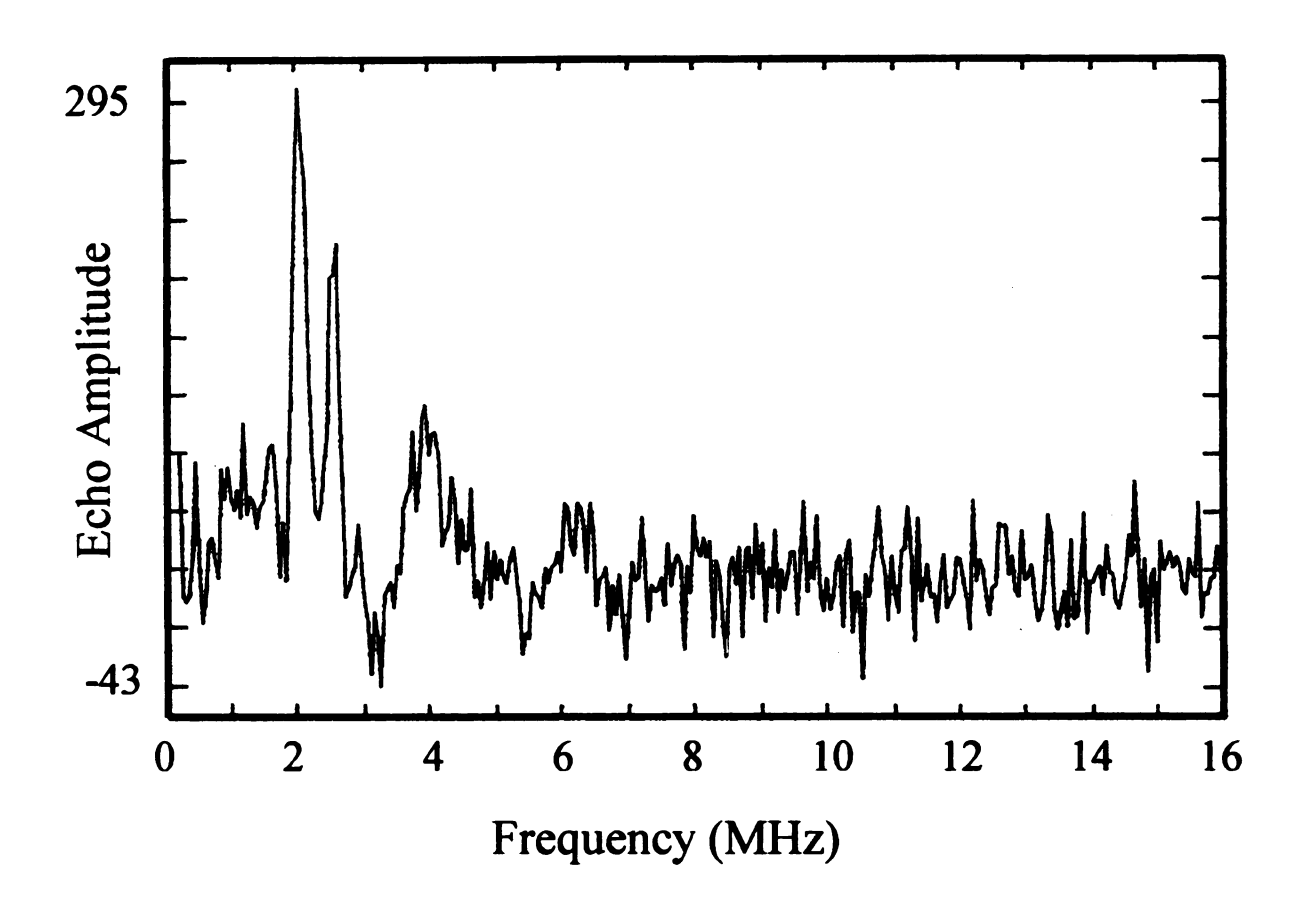


Figure 5.4: The Fourier transformation of the spectrum shown in figure 5.2 at 3140G, with the frequency at 8.81 GHz, and a  $\tau$  value of 300 ns.

characteristic frequencies ν<sub>+</sub> and ν<sub>-</sub>, defined in Equations (168) and (169) respectively. These two frequencies were used to solve for the third characteristic peak, ν<sub>o</sub>. From Equation (171), ν<sub>o</sub> was calculated to be about 0.5 MHz. Substituting ν<sub>o</sub> and the numerical values of the constants into Equation (172), the value of qη was found to be 2.071x10<sup>5</sup> J/(cm<sup>2</sup> C). The result of Equation (172) was then substituted into Equation (173) to solve for the field gradient constant q, which was 6.21375x10<sup>5</sup> V/cm<sup>2</sup>. The value of q was then substituted back into Equation (172) to find the value of the asymmetry parameter η, which was calculated to be 0.333.

Once the values of q and  $\eta$  were known, Equations (176), (177), and (178) could be solved for the quadrupole energy level shifts, illustrated in Figure 4.2(d). After substituting the numerical values for the constants, the energy level shifts in MHz were

$$E_{ml=0} = -1.5000 \text{ MHz}$$
 (179)

$$E_{mI=+1} = 0.9975 \text{ MHz}$$
 (180)

and

$$E_{ml=-1} = 0.5002 \text{ MHz}. \tag{181}$$

Therefore, in both electron manifolds, the  $m_I = 0$  energy level decreased by 1.5 MHz, while the  $m_I = +1$  and  $m_I = -1$  energy levels increased by 0.9975 MHz and 0.5002 MHz respectively, shown in Figure 4.2(d).

Since the broad peak at about 4.0 MHz was near "exact cancellation", it was used to estimate the isotropic hyperfine coupling constant,  $A_{iso}$ , for <sup>14</sup>N. As illustrated in the energy level diagram in Figure 4.2(c),  $2A_{iso} \cong 4.0$  MHz. Therefore, the approximate experimental value for  $A_{iso}$  for <sup>14</sup>N was about 2.0 MHz.

From the ESEEM data, it was evident that the paramagnetic center was interacting with <sup>14</sup>N. However, there were three different nitrogens that could couple with the paramagnetic center, as shown in Figure 5.5. The first possibility was the four pyrrole nitrogens in the corrin ring. The second possibility was the nitrogen of the lower axial dimethylbenzimidazole group. Lastly, it was also possible that the nitrogen could have been from a nitrogen-based ligand on the protein of the enzyme. An experiment was needed in order to determine which nitrogen was interacting with the paramagnetic center.

Figure 5.5: An illustration of cobalamin showing the three possible nitrogens coupled to the unpaired electron. The four nitrogens around the cobalt center are the pyrrole nitrogens. The nitrogen at the lower axial position is the nitrogen from the dimethylbenzimidazole. The dashed line leads to a nitrogen-based ligand from the protein of the enzyme.

## References

- 1. Mac, Michelle. "Advanced Electron Magnetic Resonance Studies Of Nitrogen Ligation In Photosynthetic Systems", Dissertation For the Degree Of Ph.D., 1996, p. 121.
- 2. Banerjee, R., and R. Padmakumar, *The Journal Of Biological Chemistry*, April 21, 1995, Vol. 270, No.16, pp. 9295-9300.

A sample was made by Banerjee and Padmakumar of mmCoA mutase with <sup>15</sup>N-labelled protein and deuterium-labelled substrate. From this sample it could be determined if the substrate was interacting with the enzyme, because there would be hyperfine interaction from deuterium in the ESEEM spectra. This sample would also assist in the assignment of the nitrogen. If the nitrogen being detected in the ESEEM data were from the B<sub>12</sub> cofactor, the pyrrole nitrogens or the nitrogen of the dimethylbenzimidazole, the quadrupole interaction peaks would reappear in the spectra. If, however, the nitrogen was from a nitrogen-based ligand from the enzyme, then peaks characteristic of <sup>15</sup>N would appear on the ESEEM spectra.

#### **ESEEM Data Collection**

The ESEEM data were collected on a home built spectrometer. A three-pulse sequence (90°-τ-90°-T-90°) was used. Dead time reconstruction was performed prior to Fourier transformation. Computer simulations of the ESEEM data were performed on a Sun Sparcstation 2 computer using FORTRAN software, which is based on the density matrix formalism of Mims.<sup>1</sup>

# Samples Of Methylmalonyl-CoA Mutase

Three-pulse ESEEM experiments were performed on frozen samples of the enzyme methylmalonyl-CoA mutase with the substrate *L*-methylmalonyl-CoA. The samples were prepared by Ruma Banerjee and Rugmini Padmakumar.<sup>2</sup> The sample used contained methylmalonyl-CoA mutase with <sup>15</sup>N-labelled protein, deuterated

L-methylmalonyl-CoA, and D<sub>2</sub>O buffer. Banerjee and Padmakumar were able to separate the B<sub>12</sub> cofactor from the enzyme, grow bacteria on media that contained a nitrogen source labelled with <sup>15</sup>N, and then reconstitute the protein with the B<sub>12</sub> cofactor. In other words, the B<sub>12</sub> cofactor consisted of <sup>14</sup>N, while the rest of the protein was labelled with <sup>15</sup>N.

# ESEEM Of <sup>15</sup>N Sample

The first experiment done on the <sup>15</sup>N-labelled sample was a two-pulse echo-detected EPR experiment. According to the resulting spectrum, shown in Figure 6.1, the two field values of interest were 3060 G and 3220 G. These were the two field values at which the ESEEM experiments were to be done.

The next experiments were three-pulse ESEEM experiments at 3060 G and 3220 G, and the Fourier transformation spectra are shown in Figure 6.2 and Figure 6.3 respectively. At 3060 G, the major peaks were at 1.35 MHz, 1.90 MHz, 2.50 MHz, 2.90 MHz, 3.90 MHz, and 13.00 MHz. At 3220 G, the major peaks were at 1.40 MHz, 2.05 MHz, 2.60 MHz, 2.90 MHz, 4.10 MHz, and 13.69 MHz. The two spectra were in close agreement.

The last ESEEM experiment was a three-pulse ESEEM experiment on the <sup>15</sup>N-labelled sample at 4000 G. The Fourier transformation of the three-pulse spectrum is shown in Figure 6.4. The major peaks were 0.60 MHz, 1.78 MHz, 2.90 MHz, and 5.30 MHz.

#### Discussion

In the spectrum at 3060 G in Figure 6.2, the peak at 13.00 MHz was the hydrogen larmor frequency, which is the frequency at which hydrogen comes into resonance at

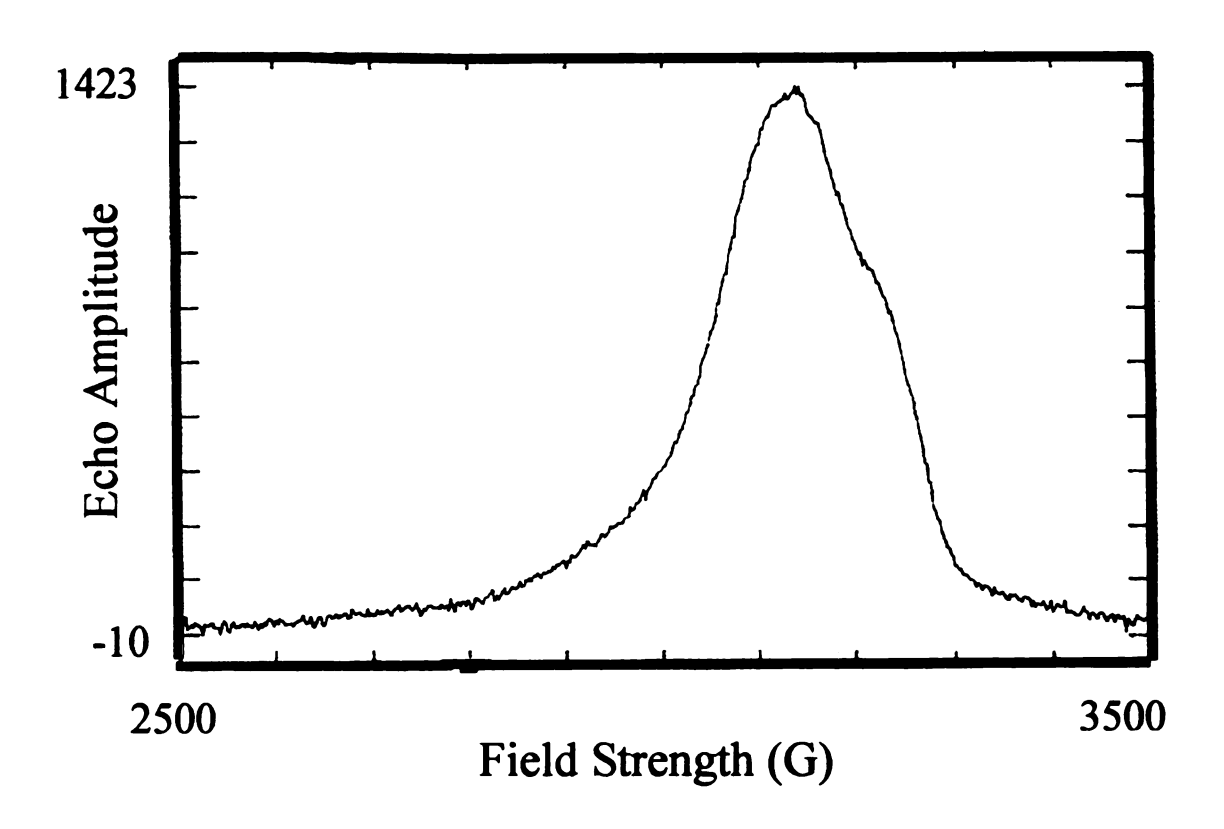


Figure 6.1: The two-pulse echo-detected EPR experiment of  $^{15}$ N-labelled mmCoA mutase with L-[CD<sub>3</sub>]mmCoA at a frequency of 9.00 GHz and a  $\tau$  value of 500 ns.

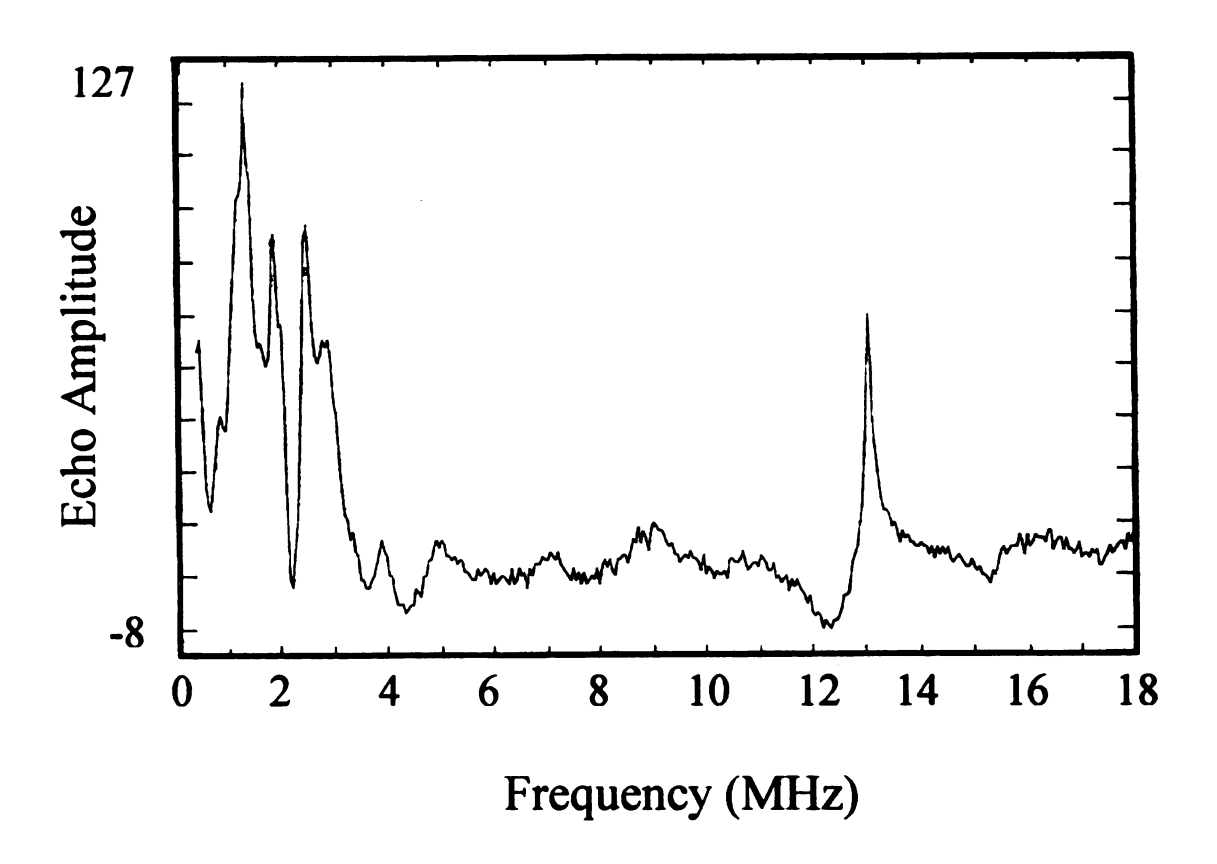


Figure 6.2: The Fourier transformation spectrum of the three-pulse ESEEM spectrum of  $^{15}$ N-labelled mmCoA mutase with L-[CD<sub>3</sub>]mmCoA at 3060G, with the frequency at 9.00 GHz and a  $\tau$  value of 500 ns.

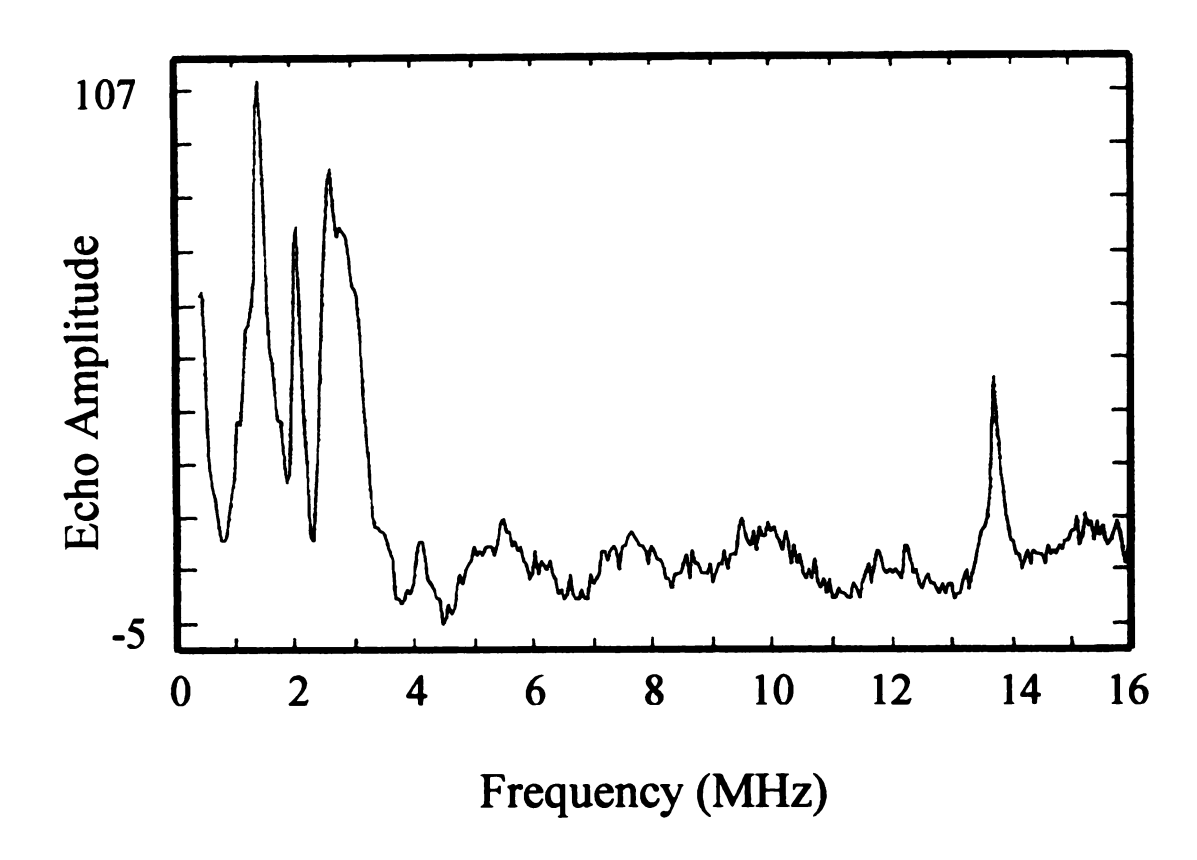


Figure 6.3: The Fourier transformation spectrum of the three-pulse ESEEM spectrum of  $^{15}$ N-labelled mmCoA mutase with L-[CD<sub>3</sub>]mmCoA at 3220 G, with the frequency at 9.00 GHz and a  $\tau$  value of 450 ns.

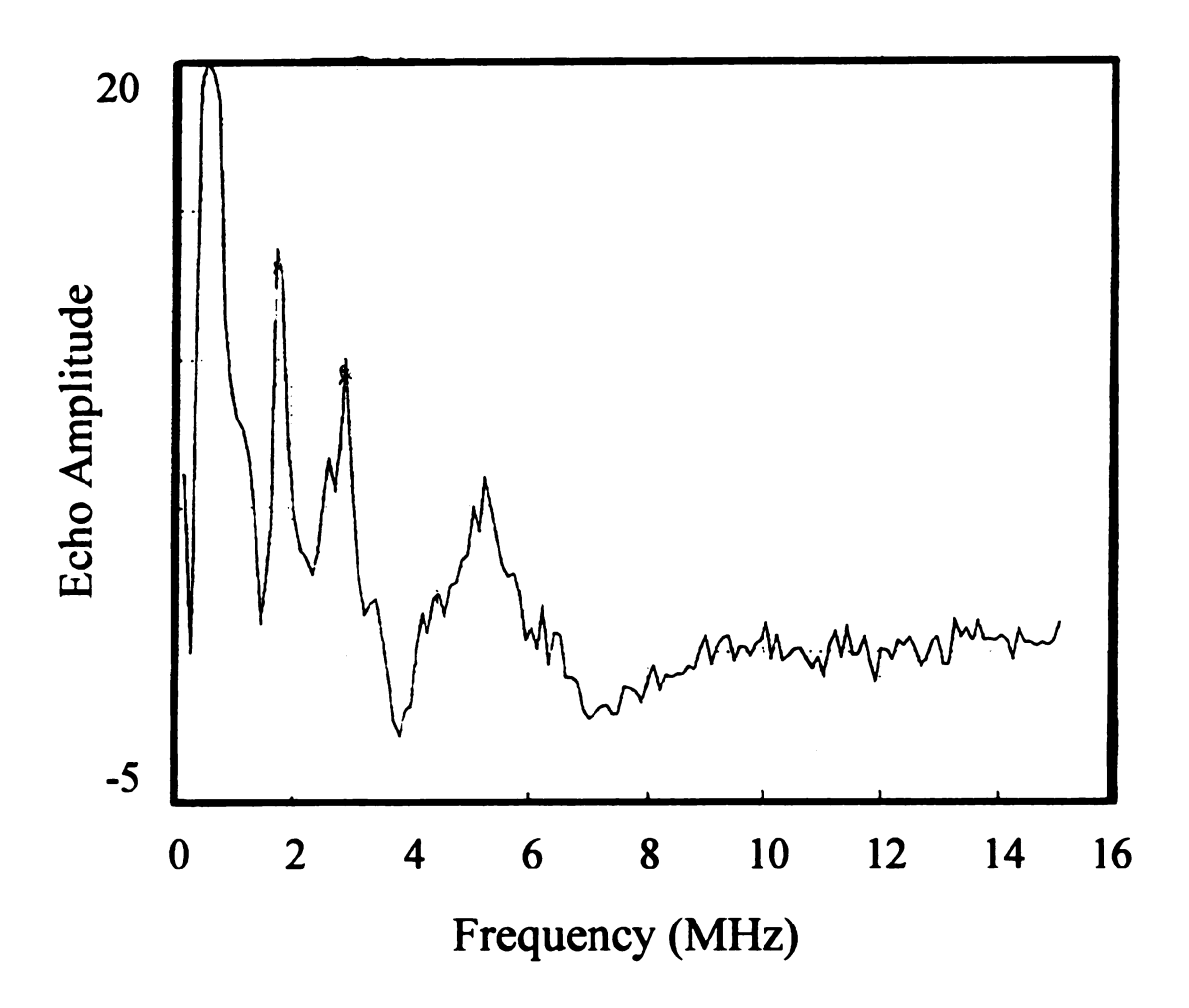


Figure 6.4: The Fourier transformation spectrum of the three-pulse ESEEM spectrum of  $^{15}$ N-labelled mmCoA mutase with L-[CD<sub>3</sub>]mmCoA at 4000 G, with the frequency at 11.64 GHz and a  $\tau$  value of 760 ns.

3060 G. Likewise, the peak at 1.9 MHz was the deuterium larmor frequency. The peaks at 1.35 MHz and 2.5 MHz were both about 0.60 MHz away from the deuterium larmor frequency. When two peaks are equidistant about the larmor frequency, that is an indication of hyperfine interaction. Therefore, it was possible that there was hyperfine interaction from deuterium.

On the other hand, the peak at 1.35 MHz was also the larmor frequency of <sup>15</sup>N, and the peak at 2.5 MHz, which is 1.15 MHz away from the <sup>15</sup>N larmor frequency, may also have been due to hyperfine from <sup>15</sup>N. If this was so, then a peak 1.15 MHz to the left of the <sup>15</sup>N larmor frequency should have also existed, which would have been at about 0.20 MHz. In order to have detected this peak, if it existed, would have required that the magnetic field be increased. So the question that needed to be answered was if there was hyperfine interaction from <sup>15</sup>N or <sup>2</sup>H?

When the magnetic field has been varied, a characteristic peak shift results, which is given by

$$\Delta v = \frac{\left(g_n \beta_n \Delta B\right)}{h}.$$
 (182)

By increasing the magnetic field to 4000 G and estimating where the peaks for <sup>15</sup>N and <sup>2</sup>H should be, it became possible to determine which nucleus was coupling to the paramagnetic center. According to Equation (182), varying the field from 3060 G to 4000 G should have shifted the <sup>15</sup>N peaks 0.43 MHz/kG, and should have shifted the <sup>2</sup>H peaks 0.65 MHz/kG. Applying these characteristic shifts to the peaks at 3060 G, the peaks at 4000 G were able to be assigned. In Figure 6.4, the peak at 1.78 MHz was the larmor frequency for <sup>15</sup>N at 4000 G, and the peaks at 0.60 MHz and 2.90 MHz were both 1.18 MHz away from the larmor frequency of <sup>15</sup>N. This indicated that there was

hyperfine interaction from <sup>15</sup>N. The small peak at about 2.60 MHz may have been the <sup>2</sup>H larmor frequency, but there was no indication of hyperfine interaction from <sup>2</sup>H. Therefore, the <sup>15</sup>N hyperfine peaks were assigned to the nitrogen belonging to the protein of the enzyme.

Using the data from the <sup>15</sup>N experiments, a more accurate hyperfine coupling constant could be found for <sup>14</sup>N. From the <sup>15</sup>N experiments, a hyperfine coupling constant could be measured for <sup>15</sup>N, and then scaled back to find the hyperfine coupling constant for <sup>14</sup>N. This method would yield a more accurate value for the hyperfine coupling constant of <sup>14</sup>N because it would not be tainted by the nuclear quadrupole interaction, as would be the case with the <sup>14</sup>N experiments.

Determining the anisotropy coupling constant of <sup>14</sup>N required scaling back from the <sup>15</sup>N data using the equation

$$\left(\frac{A}{2}\right)_{\binom{14}{N}} = \left(\frac{g_{n}\binom{14}{N}}{g_{n}\binom{15}{N}}\right)\left(\frac{A}{2}\right)_{\binom{15}{N}} \tag{183}$$

where  $g_{n(14N)} = 0.40376^2$  and  $g_{n(15N)} = 0.56638$ .<sup>2</sup> Referring to the experimental ESEEM spectrum with <sup>15</sup>N at 3060 G, shown in Figure 6.2,  $(A/2)_{(15N)}$  was measured to be about 1.15 MHz. Substituting these values into Equation (183),  $(A/2)_{(14N)}$  was found to be 0.81981 MHz, and thus  $A_{(14N)} = 1.63962$  MHz. The same procedure was performed on the ESEEM spectrum at 4000 G, where  $(A/2)_{(15N)} = 1.18$  MHz, shown in Figure 6.4. In this case,  $(A/2)_{(14N)}$  was calculated to be 0.8412 MHz, and thus  $A_{(14N)} = 1.6824$  MHz. Therefore, the anisotropy coupling constant for <sup>14</sup>N was approximately 1.66 MHz  $\pm$  0.1 MHz.

#### Conclusion

From the ESEEM experiments, some of the hyperfine lines were assigned to the nitrogen at the lower axial position of the cobalamin radical, the nitrogen at the lower axial position being a nitrogen-based ligand from the protein. It was concluded from the low frequency ESEEM experiments that <sup>15</sup>N must be at the lower axial position as illustrated in Figure 6.5, because the dimethylbenzimidazole group is the only ligand that was able to exchange with a protein ligand from the enzyme. There was no evidence from the data that the substrate was part of the paramagnetic center giving rise to the ESEEM, but rather the <sup>2</sup>H was from the solvent. From the data, it was strongly believed that the enzyme was in its "base-off" form, the "base-off" form being when the lower axial position is occupied by a nitrogen-based ligand, such as a histidyl group, from the enzyme.<sup>4</sup>

.

Figure 6.5: An illustration showing cobalamin with the cobalt center coordinated at the lower axial position to a nitrogen-based ligand from the protein of the enzyme.

#### References

- Mac, Michelle. "Advanced Electron Magnetic Resonance Studies Of Nitrogen Ligation In Photosynthetic Systems", Dissertation For the Degree Of Ph.D., 1996, p. 121.
- 2. Banerjee, R., and R. Padmakumar, *The Journal Of Biological Chemistry*, April 21, 1995, Vol. 270, No.16, pp. 9295-9300.
- 3. Weil, J. A., J. R. Bolton, and J. E. Wertz. <u>Electron Paramagnetic Resonance</u>. John Wiley & So, Inc.: New York, 1994, p. 534.
- 4. Frasca, Verna, R. Banerjee, W. Dunham, R. Sands, and R. Matthews. *Biochemistry*, 1988, Vol. 27, p. 8458.

